

VALIDATION OF NONDESTRUCTIVE TESTING EQUIPMENT FOR CONCRETE

FINAL REPORT

**Sponsored by the Florida Department of Transportation Research Center
Contract Number BD545-80**

**Dr. Dennis R. Hiltunen, P.E.
Principal Investigator**

**Dr. Daniel Algernon and Dr. Christopher C. Ferraro
Researchers**

**DEPARTMENT OF CIVIL & COASTAL ENGINEERING
UNIVERSITY OF FLORIDA**

July 2010



DISCLAIMER

The opinions, findings, and conclusions expressed in this publication are those of the authors and not necessarily those of the State of Florida Department of Transportation or the U.S. Department of Transportation.

Prepared in cooperation with the State of Florida Department of Transportation and the U.S. Department of Transportation.

METRIC CONVERSION TABLE

SYMBOL (US)		MULTIPLY BY		TO FIND		SYMBOL (SI)	
LENGTH							
in	inches	25.4		millimeters		mm	
ft	feet	0.305		meters		m	
yd	yards	0.914		meters		m	
mi	miles	1.61		kilometers		km	
AREA							
in²	square inches	645.2		square millimeters		mm²	
ft²	square feet	0.093		square meters		m²	
yd²	square yard	0.836		square meters		m²	
ac	acres	0.405		hectares		ha	
mi²	square miles	2.59		square kilometers		km²	
VOLUME							
fl oz	fluid ounces	29.57		milliliters		mL	
gal	gallons	3.785		liters		L	
ft³	cubic feet	0.028		cubic meters		m³	
yd³	cubic yards	0.765		cubic meters		m³	
MASS							
oz	ounces	28.35		grams		g	
lb	pounds	0.454		kilograms		kg	
T	short tons (2000 lb)	0.907		megagrams (or "metric ton")		Mg (or "t")	
TEMPERATURE (exact degrees)							
°F	Fahrenheit	5 (F-32)/9 or (F-32)/1.8		Celsius		°C	
FORCE and PRESSURE or STRESS							
lbf	poundforce	4.45		newtons		N	
lbf/in²	poundforce per square inch	6.89		kilopascals		kPa	
SYMBOL (SI)		MULTIPLY BY		TO FIND		SYMBOL (US)	
LENGTH							
mm	millimeters	0.039		inches		in	
m	meters	3.28		feet		ft	
m	meters	1.09		yards		yd	
km	kilometers	0.621		miles		mi	
AREA							
mm²	square millimeters	0.0016		square inches		in²	
m²	square meters	10.764		square feet		ft²	
m²	square meters	1.195		square yards		yd²	
ha	hectares	2.47		acres		ac	
km²	square kilometers	0.386		square miles		mi²	
VOLUME							
mL	milliliters	0.034		fluid ounces		fl oz	
L	liters	0.264		gallons		gal	
m³	cubic meters	35.314		cubic feet		ft³	
m³	cubic meters	1.307		cubic yards		yd³	
MASS							
g	grams	0.035		ounces		oz	
kg	kilograms	2.202		pounds		lb	
Mg (or "t")	megagrams (or "metric ton")	1.103		short tons (2000 lb)		T	
TEMPERATURE (exact degrees)							
°C	Celsius	1.8C+32		Fahrenheit		°F	
FORCE and PRESSURE or STRESS							
N	newtons	0.225		poundforce		lbf	
kPa	kilopascals	0.145		poundforce per square inch		lbf/in²	

1. Report No.	2. Government Accession No.	3. Recipient's Catalog No.	
4. Title and Subtitle Validation of Nondestructive Testing Equipment for Concrete		5. Report Date July 2010	6. Performing Organization Code
7. Author(s) Daniel Algernon, Dennis R. Hiltunen, and Christopher C. Ferraro		8. Performing Organization Report No.	
9. Performing Organization Name and Address Department of Civil and Coastal Engineering University of Florida 365 Weil Hall, P.O. Box 116580 Gainesville, FL 32611-6580		10. Work Unit No. (TRAIS)	11. Contract or Grant No. BD545-80
12. Sponsoring Agency Name and Address Florida Department of Transportation 605 Suwannee Street, MS 30 Tallahassee, FL 32399		13. Type of Report and Period Covered Final Report March 2007-March 2010	
		14. Sponsoring Agency Code	
15. Supplementary Notes			
16. Abstract The Florida Department of Transportation (FDOT) would like to implement nondestructive test and evaluation (NDT/NDE) technologies to assess quality of concrete constructed in the field as means to reduce flaws introduced by faulty construction. Toward this aim, the primary objective of the project was to design, construct, and implement a facility for calibrating and validating methodologies for the NDT/NDE of structural concrete materials and members. Four concrete test blocks have been designed and built in which specific testing problems (e.g., concrete cover, concrete thickness, and tendon ducts) were implemented to investigate them under defined conditions in the laboratory. The specimens were designed to challenge NDT techniques, and serve to demonstrate their capabilities as well as their limitations. An automated test frame has been designed, built, and implemented, and a software platform for scanner control, data acquisition with different sensors, real-time imaging and data analysis has been developed and successfully applied in the project. Automated measurements were taken with impact-echo, ultrasonic echo, and covermeter on the four concrete test specimens. GPR equipment has been procured but will require extra effort to be operated on the scanner. Covermeter measurements on the specimen with reinforcement steel clearly demonstrated the potential of this method, but also showed some limitations. Complementary ultrasonic-echo measurements in combination with the synthetic aperture focusing technique (SAFT) analysis showed the potential of this method to resolve reinforcement in cases where it cannot be resolved by the covermeter. Measurements conducted on the specimen with varying thicknesses demonstrated the capabilities of especially ultrasonic-echo. The tendon ducts in the tendon duct specimen were located in 2D by impact-echo and in 3D by ultrasonic echo. Overall, a first stage NDT validation facility has been established, and the system has been demonstrated to work precisely and reliably.			
17. Key Word Automated scanning, concrete cover, concrete thickness, covermeter, impact echo, nondestructive evaluation, nondestructive test, tendon ducts, ultrasonic echo		18. Distribution Statement No Restrictions	
19. Security Classif. (of this report) Unclassified	20. Security Classif. (of this page) Unclassified	21. No. of Pages 142 Pages	22. Price

ACKNOWLEDGMENTS

The Florida Department of Transportation (FDOT) is gratefully acknowledged for providing the financial support for this study. The FDOT Materials Office provided the additional testing equipment, materials, and personnel needed for this investigation. Sincere thanks go to the project manager, Mr. Charles Ishee, for providing his technical coordination and advice throughout the project. Sincere gratitude is extended to the FDOT Materials Office personnel, particularly to Richard DeLorenzo and Jordan Nelson for their invaluable help in this study.

Sincere thanks also go to the FDOT Structures Office in Tallahassee, FL, for transferring two of their very well designed and documented test blocks, which were an excellent complement to the test blocks designed in the course of the project.

Special thanks go to the great support and advice of Dr. Herbert Wiggensauser and his group, division VIII.2 at the Federal Institute for Materials Research and Testing (BAM) in Berlin, Germany.

The support of Proceq SA in giving access to modified hardware, thus making automated covermeter measurements possible, is greatly acknowledged by the authors.

EXECUTIVE SUMMARY

The Florida Department of Transportation (FDOT) would like to implement nondestructive test and evaluation (NDT/NDE) technologies to assess quality of concrete constructed in the field as means to reduce flaws introduced by faulty construction. Toward this aim, the primary objective of the project was to design, construct, and implement a facility for calibrating and validating methodologies for the NDT/NDE of structural concrete materials and members.

Four concrete test blocks have been designed and built in which specific testing problems (e.g., concrete cover, concrete thickness, and tendon ducts) were implemented to investigate them under defined conditions in the laboratory. The specimens were designed to challenge NDT techniques, and serve to demonstrate their capabilities as well as their limitations.

An automated test frame has been designed, built, and implemented, and a software platform for scanner control, data acquisition with different sensors, real-time imaging and data analysis has been developed and successfully applied in the project.

Automated measurements were taken with impact-echo, ultrasonic echo, and covermeter on the four concrete test specimens. GPR equipment has been procured but will require extra effort to be operated on the scanner. Covermeter measurements on the specimen with reinforcement steel clearly demonstrated the potential of this method, but also showed some limitations. Complementary ultrasonic-echo measurements in combination with the synthetic aperture focusing technique (SAFT) analysis showed the potential of this method to resolve reinforcement in cases where it cannot be resolved by the covermeter. Measurements conducted on the specimen with varying thicknesses demonstrated the capabilities of especially ultrasonic-echo. The tendon ducts in the tendon duct specimen were located in 2D by impact-echo and in 3D by ultrasonic echo. Overall, a first stage NDT validation facility has been established, and the system has been demonstrated to work precisely and reliably.

TABLE OF CONTENTS

1	INTRODUCTION.....	9
1.1	MOTIVATION	9
1.2	OBJECTIVES AND TASKS.....	9
1.3	ASSESSMENT OF THE PREVALENT CONCRETE PROBLEMS AND AVAILABLE NDT TECHNOLOGY.....	10
2	CONCRETE SPECIMENS.....	14
2.1	GENERAL CONSIDERATIONS.....	14
2.2	SPECIMEN 0, CONTROL BLOCK.....	15
2.3	SPECIMEN 1, REINFORCING STEEL.....	15
2.3.1	Considerations.....	15
2.3.2	Design.....	16
2.4	SPECIMEN 2, VARYING THICKNESSES	21
2.4.1	Considerations.....	21
2.4.2	Design.....	22
2.5	SPECIMEN 3, TENDON DUCTS.....	24
2.5.1	Considerations.....	24
2.5.2	Design.....	25
2.6	SPECIMENS 3-1 AND 3-2, ADDITIONAL TENDON DUCT BLOCKS	28
2.7	BLOCK COORDINATE SYSTEM	29
3	DATA IMAGING.....	30
3.1	B-, C -, AND D-SCAN IMAGING	30
3.2	SYNTHETIC APERTURE FOCUSING TECHNIQUE (SAFT)	32
4	HARD- AND SOFTWARE.....	34
4.1	AUTOMATED TESTING FRAME.....	34
4.2	NDT SENSORS.....	36
4.3	SOFTWARE DEVELOPMENT.....	39
4.3.1	Interfaces	39
4.3.2	Operation.....	39
5	MEASUREMENTS ON LABORATORY SPECIMENS.....	44
5.1	CONTROL BLOCK, REFERENCE MEASUREMENTS	44
5.1.1	Impact-Echo	44
5.1.2	Ultrasonic-Echo Measurements	49
5.2	COVERMETER CALIBRATION EXPERIMENTS ON A SMALL CONCRETE BLOCK WITH REBAR.....	50
5.2.1	Calibration Experiment No. 1, Rebar Depth	51
5.2.2	Calibration Experiment No. 2.....	53
5.2.3	Calibration Experiment No. 3, Rebar Size.....	57
5.2.4	Calibration Experiment No. 4, Rebar Spacing	58
5.2.5	Conclusion from the Experiments.....	60
5.3	SPECIMEN 1, STEEL REINFORCEMENT.....	62
5.3.1	Covermeter Measurements	62
5.3.2	Ultrasonic Echo.....	71
5.4	BLOCK WITH VARYING THICKNESSES.....	75
5.4.1	Ultrasonic Echo Measurements.....	75
5.4.2	Impact-Echo Measurements	92
5.5	TENDON DUCT BLOCK	110
5.5.1	Impact-Echo Measurements	110
5.5.2	Ultrasonic Echo Measurements.....	118

5.5.3	<i>Covermeter Measurements</i>	124
5.6	<i>MEASUREMENTS ON SPECIMEN 3-1, TENDON DUCTS</i>	125
5.6.1	<i>Impact-Echo Measurements</i>	125
5.7	<i>DISCUSSION</i>	128
5.7.1	<i>Localizing Reinforcement Steel in Concrete Components</i>	128
5.7.2	<i>Thickness Measurements</i>	129
5.7.3	<i>Tendon Duct Inspections</i>	129
6	<i>DETERMINING ELASTIC PARAMETERS USING ACOUSTIC NDT METHODS</i>	131
6.1	<i>THEORY</i>	131
6.2	<i>DEMONSTRATION</i>	133
6.3	<i>DISCUSSION</i>	134
7	<i>CLOSURE</i>	136
7.1	<i>SUMMARY OF FINDINGS</i>	136
7.2	<i>CONCLUSIONS</i>	137
7.3	<i>RECOMMENDATIONS</i>	137
8	<i>REFERENCES</i>	139

1 Introduction

1.1 *Motivation*

The Florida Department of Transportation (FDOT) has addressed durability problems with Portland cement concrete in structural applications. While the desired design life for bridges in Florida is now 100 years, the production of concrete for these significant design periods is rather challenging. One of the biggest problems affecting durability is the corrosion of reinforcing steel due to infiltration of concrete with salt water, which is particularly a problem for structures located in coastal areas, e.g., Miami, Tampa. Infiltration and corrosion is not typically a result of design mistakes, but rather a product of flaws induced during construction. These flaws include inadequate cover due to improper placement of steel reinforcement, inconsistent consolidation which can result in debonding and air pockets near reinforcement, and surface cracks due to improper finishing, curing, etc. All of these flaws are likely to accelerate infiltration and corrosion. Currently, the inspection and acceptance of facilities constructed of structural concrete is based upon visual surveys and results from traditional tests on concrete samples, e.g. slump, cylinder breaks, etc. However, the FDOT would like to move toward implementation of nondestructive test and evaluation (NDT/NDE) technologies to assess quality of concrete constructed in the field as means to reduce flaws introduced by faulty construction. An efficient application of such methods can lead to improved quality of concrete construction, improved durability and longer life, and significant cost savings for the state of Florida.

To be implemented, these technologies must be proven to be effective, and this proof is developed via calibration and validation research experiments in which the technologies are shown to be accurate and reliable in circumstances where the result (i.e., concrete characteristics as well as the size and position of objects, such as reinforcing steel, tendon ducts or voids inside the concrete) is well known. While significant development of such a facility has occurred at the Federal Institute for Materials Research and Testing (BAM) in Berlin, Germany, a comprehensive facility for such experiments does not exist in the United States. This was the motivation for the FDOT to fund this project dealing with the development of a first stage NDT validation facility at their State Materials Office (SMO) in Gainesville, Florida.

1.2 *Objectives and Tasks*

The primary objective of the proposed project has been to design, construct, and implement a facility, which would allow calibrating and validating methodologies for the NDT/NDE of structural concrete materials and members.

This includes the design and construction of concrete specimens with known characteristics for calibration/validation activities. Besides the procurement and application of testing devices and sensors, an automated scanning system for controlling and conducting NDT/NDE experiments on the specimens was to become a major part of

the facility. Knowing that the extensive NDT facility at BAM has required a sustained development effort over many years, the goal of the two-year project described in this report was to produce a first-stage facility that would mimic a subset of the capabilities available at BAM, as well as create a vision of a comprehensive facility suitable for conditions in the state of Florida.

The project was directed toward solution of problems most relevant to transportation structures in the state of Florida and to clearly demonstrate the capabilities and limitations of NDT technology. Therefore, the concrete problems prevalent in the state had to be assessed, and available and emerging NDT technologies with potential for revealing and documenting the major problems associated with concrete in Florida had to be identified.

Concrete specimens with known material properties and internal conditions including flaws would allow the conduction of accurate and repeatable calibration and validation experiments with NDT technologies.

An automated scanning system as it has been developed and successfully applied by BAM was identified to be an important aspect of the project, as it allows to minimize the human factor in the evaluation of the capabilities of different NDT systems, make the experiments repeatable and allow to collect a very large and therefore statistically meaningful number of measurements on a test object. Especially when the data is visualized in scan images, the asset of an automated scanning system becomes clear.

For the application of the different NDT methods, sensors and hardware were to be procured. To operate these sensors with the scanning system, a software platform, which controls the scanner, synchronizes the data acquisition with it, saves and visualizes the data, had to be developed in the project.

Following implementation, a series of simple experiments were conducted with the NDT technology chosen. These experiments were aiming to shakedown and establish the capabilities of the integrated NDT equipment and concrete specimens.

1.3 Assessment of the Prevalent Concrete Problems and Available NDT Technology

To further understand the prevalent problems, the research team met with FDOT representatives to uncover the major problems associated with concrete in Florida. As an outcome of the discussion, it was decided to focus on four major testing problems to be solved by NDE:

1. Measuring the concrete cover of steel reinforcement. To protect the reinforcement steel from corrosion, a minimum concrete cover is essential. In cases where the concrete cover is too low, the durability of the reinforcement steel and therefore the structural component can be significantly reduced. Determining the actual

concrete cover can therefore ensure the protection of the steel from corrosion and can likely increase the lifetime of a structure.

2. Measuring the thickness of concrete components. Measuring the thickness of structural components to ensure the required thickness can prevent an overstraining of that component. Furthermore, on components that are accessible only from one side, thickness measurements can reveal damages near the opposite side. In cases where a layer of concrete is protecting another component from environmental exposure, maintaining a minimum concrete thickness can be crucial for the durability of the component.
3. Inspection of tendon ducts. In structures made of prestressed concrete with post-tensioned tendon ducts, the tendons are protected from corrosion by a cementitious grout. Air voids within the grout can be dangerous, as over the years, moisture within the air can be a source of corrosion. The consequences can be fatal.
4. Providing material parameters as an input for measurements of bridge deflection. To determine the condition of concrete bridges, deflectometer measurements can provide some useful information. However, this information requires a prior knowledge or estimation of certain material parameters. In most cases, these parameters will be simply estimated, which naturally causes some uncertainty within the results. If these parameters could be determined more precisely from NDT tests carried out before the actual deflection test, the accuracy of the results could be significantly increased.

Having defined the major testing problems to focus on, the adequate NDT techniques had to be identified and defined. The experience gained in the BAM group as well as a review of the existing literature on these topics led to the decision to include the following NDT techniques in the focus of the project:

- Ultrasonic Echo
- Impact-Echo
- Covermeter
- GPR
- Laser Profilometer

Ultrasonic Echo: In recent years, ultrasonic echo has been successfully applied in various inspections of concrete bridges ([1], [2], [3]). Especially the development of a dry-coupled ultrasound sensor working with shear waves generated by an array of twelve transducers, and measured by an array of another twelve transducers [4], has made this method very practical in use. In combination with a signal processing technique referred to as SAFT (Synthetic Aperture Focusing Technique, [5], [6]) explained in chapter 3.2, it is highly suitable for imaging the inside of a concrete component. Its field of applications comprises thickness measurements, flaw detection, and inspection of tendon ducts ([7], [8]).

Impact-Echo (IE): Having a long tradition ([9]), IE is still one of the most widely used NDT techniques for inspection of concrete structures. Being different from ultrasound echo, acoustic waves are generated by the elastic impact of a small steel sphere or hammer. The occurring multiple reflections of the waves are analyzed according to the following equation [9]:

$$d = \frac{c_L}{2f}, \quad (1)$$

d: reflector depth

c_L: longitudinal wave velocity

f: measured frequency

It is commonly used for thickness measurements, flaw detections, and tendon duct inspections. While it is normally used as a single-point measurement method, i.e., at every measurement point the curve obtained is analyzed for itself, its application as a scanning method in combination with various imaging techniques as done by BAM, seems to be more promising, especially because the risk of misinterpretations can be reduced. The advantage of the imaging becomes evident, for example, in its potential to detect voids in the grout of post-tensioning tendon ducts. While the interpretation of the wave reflection at the tendon duct as proposed in [9] can rarely be measured in practice, another effect occurring at the duct seems to reveal better information regarding the grout condition of the duct and is nowadays widely used ([10], [11], [12], [13], [14], [16]). It is the apparent shift of the backwall indication towards lower frequencies at the position of the duct that can be used to locate the duct in its lateral position. The simplest way to explain this phenomenon is to look at it as a wave diffraction as illustrated in the sketch in Figure 1. The wave generated by the impact at the surface of the concrete object reaches the duct. Due to the cylindrical shape of the duct, only a small part of the wave energy is reflected while the biggest portion is diffracted at the duct and still reaches the backwall, where it is reflected, then reaches the duct again and is diffracted once again before it reaches the surface again. The diffraction causes a delay resulting in a slightly lower frequency indication in the frequency domain. The quantity of this delay and the frequency shift, respectively, depend on whether the duct is filled with grout or empty. An empty duct would naturally show a larger shift, i.e., an indication at a lower frequency, than a grouted duct. However, this interpretation has its limitations. Since a small air gap, as it would occur at the inside of the duct if the grout is debonded, cannot be passed by the wave, the occurring effect would be the same as if the duct was completely empty. Therefore, whenever the grout is not bonded to the duct for any reason, this method will give results that are misleading. The existence of various publications dealing with signal processing techniques (e.g., [17], [18]) to enhance the signal quality indicates that the signals obtained tend to be rather complex.

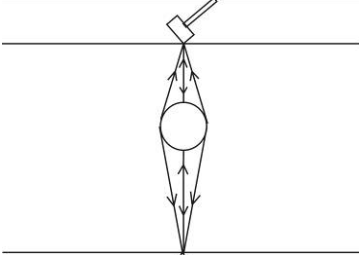


Figure 1: Wave reflection and diffraction occurring at a reflector of cylindrical shape.

Covermeter: Covermeters are widely used to measure the concrete cover of reinforcement steel. There are a variety of different models by different manufacturers available. As can be found in the literature (e.g. [19], [20]), for an exact measurement of the concrete cover the diameter of the reinforcement bars has to be known. The penetration depth is relatively low.

Ground Penetrating Radar (GPR): GPR has many applications in a number of fields. Engineering applications include nondestructive testing (NDT) of structures and pavements. As an electromagnetic method, it is very sensitive to metallic reflectors in the concrete, e.g. reinforcement and metal tendon ducts. In the various publications (e.g. [21]) on the successful application of GPR it can also be found that the density of the reinforcement right below the measurement surface has a major effect on the maximum depth that can be assessed with this method, since dense reinforcement will reflect almost all of the energy and will make it hardly possible to measure below it. For tendon duct inspections, GPR is used to determine the exact location of the duct. However, since the electromagnetic waves are reflected almost completely at the metal duct, it is not possible to measure inside the duct to detect a possible void in the grout. It will therefore be used in combination with acoustic methods like ultrasonic echo or impact echo [22].

Laser Profilometer: Laser profilometers are scanned contactless along a surface and measure the distance to the surface, thus providing a surface profile of the scan area [23]. This can be useful to adjust other sensors (e.g. impact-echo sensor) according to the profile to guarantee good coupling. Furthermore, the surface profile can be used to determine the exact thickness of the block as a reference in the evaluation of thickness measurements with other sensors. For example, to determine the accuracy of an impact-echo sensor regarding measuring the thickness of a concrete specimen, the actual thickness of the block at every measurement position has to be known. However, due to the fabrication process of the specimen, the thickness will vary over the specimen and cannot be determined by measuring only along the edges of the block using a tape measure. Therefore, a surface profile obtained from laser measurements can provide some valuable information.

2 Concrete Specimens

2.1 General Considerations

For an objective study it is necessary to create defined conditions under which the methods can be validated. Therefore, the design of adequate specimens is essential. Specimens in the laboratory allow the isolation of certain testing problems as well as the variation of certain parameters. Because of the controlled conditions in the laboratory, the number of unknown variables can be decreased, which makes it possible to concentrate on specific aspects, investigate them in detail, and gain further information on the capabilities and limitations of the methods.

To be able to evaluate the critical aspects concerning the different methods that are going to be applied, these aspects have to be taken into account for the design of the specimens. To investigate the capabilities of NDT methods in solving the above named testing problems, every testing problem should at first be studied by itself to limit the number of variables. Therefore, every specimen should include only one type of testing problem resulting in altogether at least four specimens for the four testing problems.

To minimize artifacts caused by boundary effects, the dimensions of the specimens should not be too compact. On the other hand, there are practical limitations because the specimens are placed in the laboratory and will have to be movable. As a compromise, a size of approximately 2.00 m × 1.50 m (6.6' × 5') and a thickness of up to 50 cm (20") was chosen for all four blocks.

For better identification of artifacts, all specimens should have the same geometry as well as the same material properties as far as it is possible. For the same reason, it was decided to build an additional control block, which should be a solid concrete block without any testing problems implemented.

For all specimens described in the following, regular strength concrete is used according to a mix design as shown in Table 2.

Table 1: Concrete mix design for test specimen blocks.

Quantity	Cement	Water	Fine Aggregate	Course Aggregate	Air Entraining	Water Reducers
Per yd ³	680 lb	239 lb	1173 lb	1770 lb	5.1 oz	95.2 oz
Per m ³	3.956 kN	1.390 kN	6.824 kN	10.297 kN	0.197 L	3.68 L

2.2 Specimen 0, Control Block

This specimen (Figure 2) serves as a reference for the measurements conducted on the other blocks, where particular testing problems are being assessed. As far as possible, this block was supposed to have the same dimensions and geometry as the other blocks (approximately 1.97 m × 1.48 m × 25 cm (6.6' × 4.9' × 10")). In case that there are indications in the data collected on one of the other blocks, which cannot be explained unambiguously, the data can be compared with that obtained from this control block. If the same indications occur on the control block as well, they are most probably caused by the geometry of the block and not related to the actual testing problem. This can reduce the risk of misinterpreting the results.

Since the measurements are not affected by reflections caused by voids or other built-in reflectors such as rebars, tendon ducts, etc., this specimen is also adequate for a study on the capabilities of the NDT techniques in determining certain material parameters of the test object.

Furthermore, it also serves to practice the handling of the heavy blocks in the laboratory (e.g., formwork construction, mix, handling with the forklift) before risking damage of one of the blocks with testing problems implemented.



Figure 2: Specimen 0, control block.
Left: Reusable formwork as it was used for the other blocks as well.
Right: Finishing the surface of the block after the concrete was poured.

2.3 Specimen 1, Reinforcing Steel

2.3.1 Considerations

This specimen serves to evaluate the capabilities of NDT technology in determining the location of steel reinforcement in concrete. Concerning the reinforcement, the following parameters are considered crucial and therefore were varied over the block:

- a) rebar diameter
- b) rebar depth
- c) rebar spacing
- d) rebars in different layers, interaction between them, influence on the measurement

a) The block has reinforcement with different diameters, ranging from #3 rebars (9.5 mm) up to #9 (29.7 mm). This is to investigate how far the diameter has an effect on the measurements and their accuracy.

b) The rebar depth of the reinforcement varies within a range of approximately 25 mm (1") to 125 mm (5"). This is to investigate how far the accuracy of the measurement is dependent on the depth. The depth range was chosen as a compromise between the rebar depths occurring in practice and the limits of the covermeter in automatic (low depth range, highest accuracy) mode. Naturally, this is also dependent on the rebar diameter.

c) As it can be found in the literature ([19], [20]), measurements using a covermeter become inaccurate in areas of high reinforcement density. This parameter has been taken into account and investigated on the specimen. Therefore, the distance between the rebars varies over the specimen. There are some areas where the rebar spacing is as close as 3.5 cm (1.5"). It is well-known that such dense rebar spacing makes covermeter measurements more than challenging, and is actually less than the required minimum spacing for the covermeter to resolve the rebars [20]. Nevertheless, this is supposed to demonstrate the value of the different methods and devices as well as their limitations.

d) There are areas with reinforcement in just one layer as well as areas with two and even three layers of reinforcement.

2.3.2 Design

Figure 3, Figure 4 and Figure 5 reveal the design of the specimen. It has a 25 cm (10") thickness and reinforcement on both sides (upper and lower layer).

The reinforcement running in y-direction (short side of the specimen) on the front of the specimen can be divided in two different sections. In one section, the rebar diameter varies from #3 (9.525 mm) up to #9 (28.65 mm) and has a concrete cover of approximately 59 mm (2.4"). The diameter is incrementally increased to study the influence of the steel diameter on the measurements. The second section serves to investigate the influence of the rebar spacing on the accuracy of the measurements. The spacing varies from 25 cm (10") down to a spacing of 3.75 cm (1.5"). All rebars in this section have the same diameter #3 (11 mm) and concrete cover of approximately 59 mm (2.4").

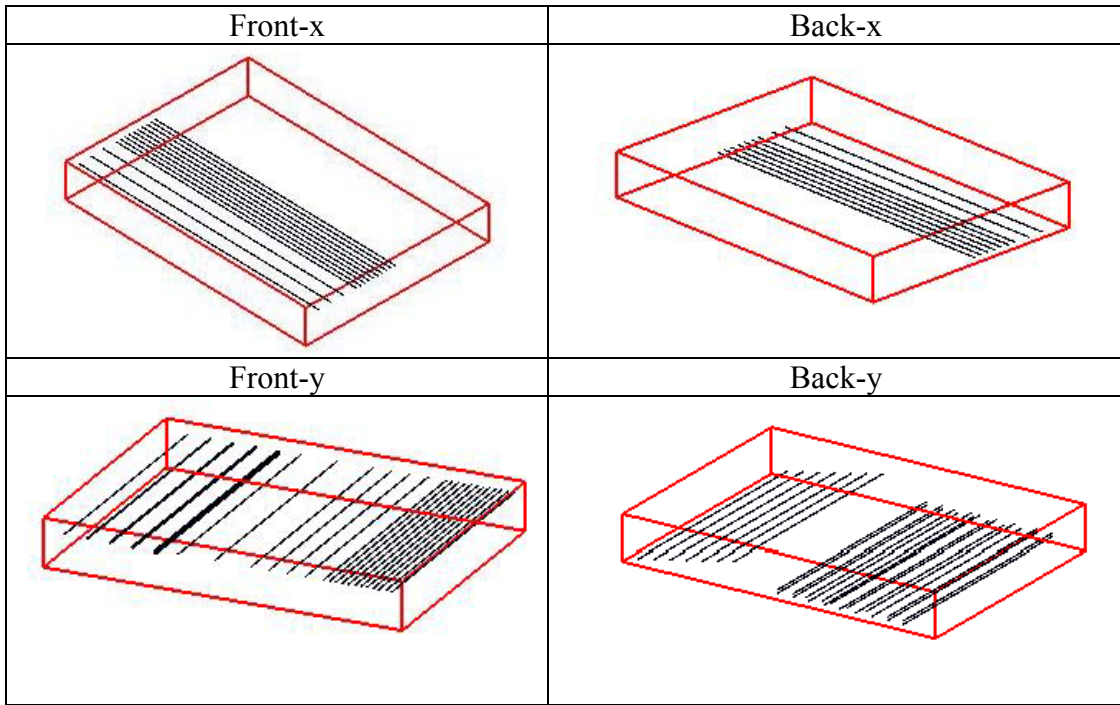


Figure 3: Different layers of reinforcement in the block.

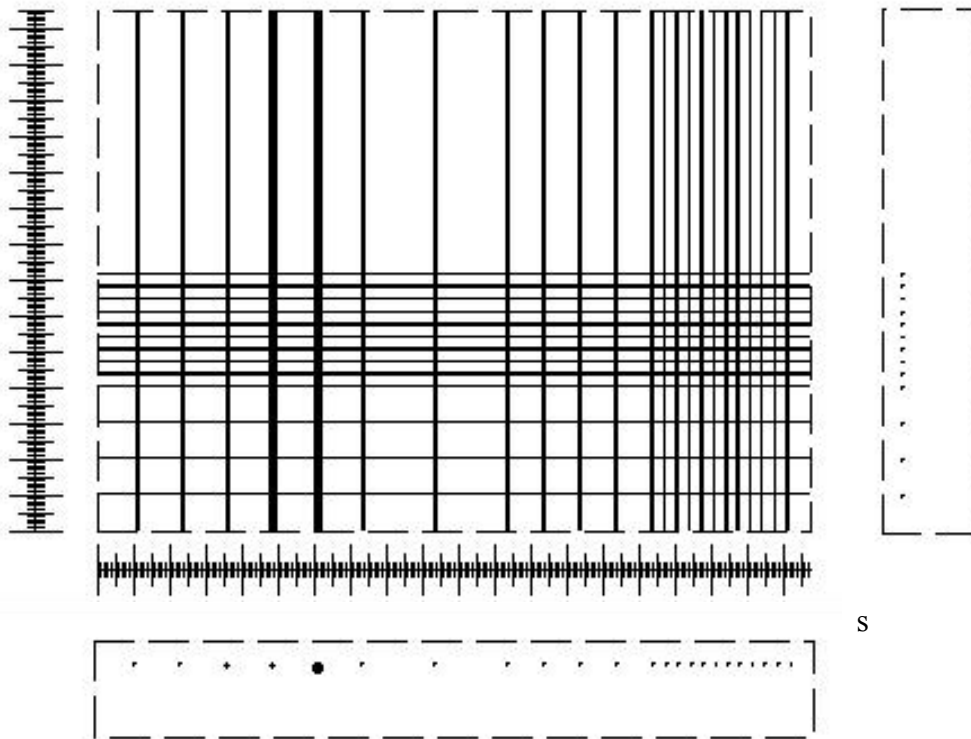


Figure 4: Steel reinforcement layers on the front of the block.

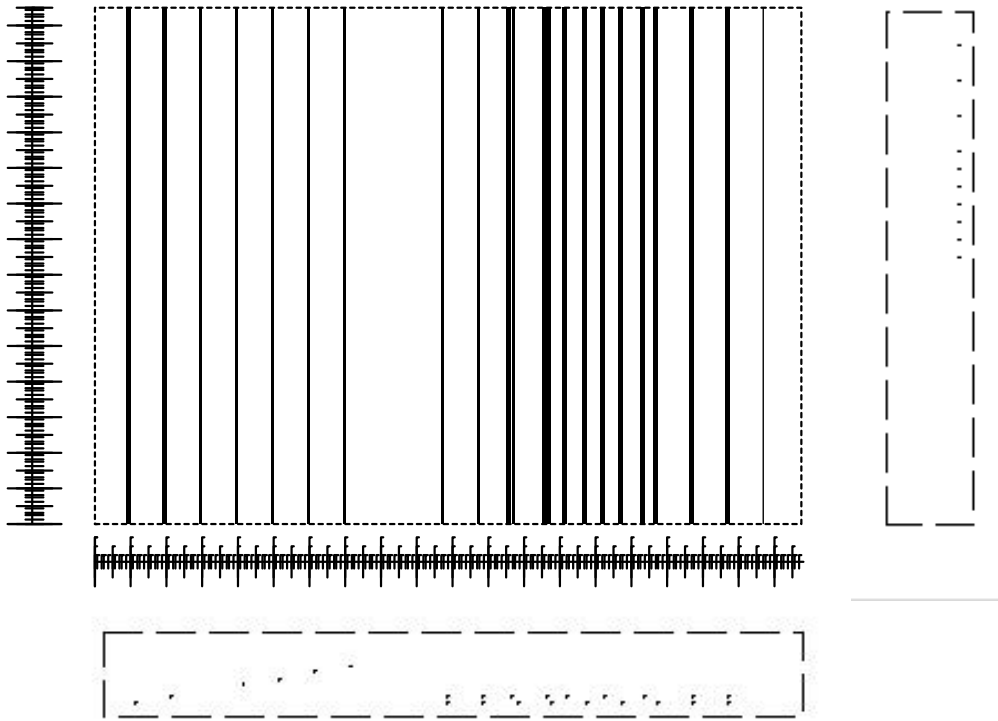


Figure 5: Steel reinforcement layers on the back of the block.

The reinforcement running in x-direction on the front of the block covers only half of its y-length (height), so that a possible influence of that layer on the detection of the first layer can be studied as well. This second layer consists of an area with a wider spacing of 10 cm (4") between the rebars and an area with a spacing as small as 3.5 cm (1.38"). Among other questions it serves to investigate how far the localization of the second layer is affected by the spacing of the reinforcement in the first layer.

In the first section of the reinforcement running in y-direction at the back of the block the depth of the rebars (all #3 rebars, 11 mm diameter) is incrementally increased. This serves to investigate up to what depth a rebar with that diameter can be detected and how far the accuracy depends on the depth.

The second section serves to investigate up to what depth the rebars of three reinforcement layers can be detected. Some of the rebars are congruent; others are shifted against each other. Regarding the measurements, the question will be in how far the rebars of the different layers can be discerned and if this is depending on the amount of shift.

A list of all rebars in this specimen is provided in Table 22 (x-direction) and Table 3 (y-direction). The specimen was fabricated in a reusable wooden formwork (Figure 6).

Table 2: Reinforcement in x-direction (horizontal) in the reinforced concrete block.

x-Reinforcement

Index	y- Position (")	Depth (")	Depth (mm)	Cover Front (mm)	Cover Back (mm)	Diameter (")	Size #	Diameter (mm)
x_1	4	2.375	59	55	186	0.375	#3	9.525
x_2	8	2.375	59	55	186	0.375	#3	9.525
x_3	12	2.375	59	55	186	0.375	#3	9.525
x_4	16	2.375	59	55	186	0.375	#3	9.525
x_5	17.375	2.375	59	55	186	0.375	#3	9.525
x_6	18.75	2.375	59	55	186	0.375	#3	9.525
x_7	20.125	2.375	59	55	186	0.375	#3	9.525
x_8	21.5	2.375	59	55	186	0.375	#3	9.525
x_9	22.875	2.375	59	55	186	0.375	#3	9.525
x_10	24.25	2.375	59	55	186	0.375	#3	9.525
x_11	25.75	2.375	59	55	186	0.375	#3	9.525
x_12	27.125	2.375	59	55	186	0.375	#3	9.525
x_13	28.5	2.375	59	55	186	0.375	#3	9.525
x_14	30	8.625	216	211	30	0.375	#3	9.525
x_15	32	8.625	216	211	30	0.375	#3	9.525
x_16	34	8.625	216	211	30	0.375	#3	9.525
x_17	36	8.625	216	211	30	0.375	#3	9.525
x_18	38	8.625	216	211	30	0.375	#3	9.525
x_19	40	8.625	216	211	30	0.375	#3	9.525
x_20	42	8.625	216	211	30	0.375	#3	9.525
x_21	46	8.625	216	211	30	0.375	#3	9.525
x_22	50	8.625	216	211	30	0.375	#3	9.525
x_23	54	8.625	216	211	30	0.375	#3	9.525

Table 3: Reinforcement in y-direction (vertical) in the reinforced concrete block.

y-Reinforcement

Index	x-Position (")	Depth (")	Depth (mm)	Cover Front (mm)	Cover Back (mm)	Diameter (")	Size #	Diameter (mm)
y_1	4.625	2.562	64	59	181	0.375	#3	9.525
y_2	9.625	2.625	66	59	178	0.5	#4	12.7
y_3	14.625	2.687	67	59	175	0.625	#5	15.875
y_4	19.625	2.75	69	59	172	0.75	#6	19.05
y_5	24.625	2.937	73	59	162	1.125	#9	28.65
y_6	29.625	2.562	64	59	181	0.375	#3	9.525
y_7	35.625	2.562	64	59	181	0.375	#3	9.525
y_8	45.625	2.562	64	59	181	0.375	#3	9.525
y_9	49.625	2.562	64	59	181	0.375	#3	9.525
y_10	53.625	2.562	64	59	181	0.375	#3	9.525
y_11	57.625	2.562	64	59	181	0.375	#3	9.525
y_12	61.625	2.562	64	59	181	0.375	#3	9.525
y_13	63	2.562	64	59	181	0.375	#3	9.525
y_14	64.375	2.562	64	59	181	0.375	#3	9.525
y_15	65.75	2.562	64	59	181	0.375	#3	9.525
y_16	67.125	2.562	64	59	181	0.375	#3	9.525
y_17	68.5	2.562	64	59	181	0.375	#3	9.525
y_18	69.875	2.562	64	59	181	0.375	#3	9.525
y_19	71.125	2.562	64	59	181	0.375	#3	9.525
y_20	72.5	2.562	64	59	181	0.375	#3	9.525
y_21	73.75	2.562	64	59	181	0.375	#3	9.525
y_22	75.25	2.562	64	59	181	0.375	#3	9.525
y_23	76.675	2.562	64	59	181	0.375	#3	9.525
y_24	3.875	8.687	217	212	28	0.375	#3	9.525
y_25	7.875	7.937	198	194	47	0.375	#3	9.525
y_26	12	7.187	180	175	66	0.375	#3	9.525
y_27	16	6.437	161	156	84	0.375	#3	9.525
y_28	20	5.812	145	141	100	0.375	#3	9.525
y_29	24	4.937	123	119	122	0.375	#3	9.525
y_30	28	4.187	105	100	141	0.375	#3	9.525
y_31	39	7.937	198	194	47	0.375	#3	9.525
y_32	39	8.687	217	212	28	0.375	#3	9.525
y_33	43	7.937	198	194	47	0.375	#3	9.525
y_34	43	8.687	217	212	28	0.375	#3	9.525
y_35	46.375	7.937	198	194	47	0.375	#3	9.525
y_36	47	8.687	217	212	28	0.375	#3	9.525
y_37	50.375	7.937	198	194	47	0.375	#3	9.525
y_38	50.875	8.687	217	212	28	0.375	#3	9.525
y_39	52.625	7.937	198	194	47	0.375	#3	9.525
y_40	54.875	8.687	217	212	28	0.375	#3	9.525
y_41	56.875	7.937	198	194	47	0.375	#3	9.525
y_42	58.875	8.687	217	212	28	0.375	#3	9.525
y_43	61.375	7.937	198	194	47	0.375	#3	9.525
y_44	62.875	8.687	217	212	28	0.375	#3	9.525
y_45	66.875	7.937	198	194	47	0.375	#3	9.525
y_46	66.875	8.687	217	212	28	0.375	#3	9.525
y_47	70.875	7.937	198	194	47	0.375	#3	9.525
y_48	70.875	8.687	217	212	28	0.375	#3	9.525
y_49	74.875	7.937	198	194	47	0.375	#3	9.525
y_50	74.875	8.687	217	212	28	0.375	#3	9.525



Figure 6: Fabrication of the specimen with steel reinforcement.
Left: Formwork. The rebars are held in place by holes in an additional layer of wood in the formwork.
Right: Pouring and compacting the concrete.

2.4 Specimen 2, Varying Thicknesses

2.4.1 Considerations

The relevant thickness range for most practical applications is from about 15 cm (6") up to about 50 cm (20"). Therefore, the specimen should have thicknesses varying within that range. The critical aspects regarding the measurements are:

- a) accuracy of thickness measurements
- b) how big do the lateral dimensions of a minor thickness have to be to be detected
- c) boundary effects, geometry of the specimen
- d) what is underneath/behind the concrete, i.e. type of interfaces, air, soil, polystyrene, steel.

a) To determine the accuracy of the measurements the true thickness has to be known as exact as possible.

b) The specimen has thickness areas of different dimensions.

c) If the lateral dimensions of the specimen are too small, boundary effects will increasingly interfere with the actual measurements. Therefore, the standard size of roughly 2 m × 1.50 m (6.7' × 5') should be the minimum size for this specimen as well.

d) In a first step, only air interfaces will be considered.

2.4.2 Design

This specimen consists of six areas (Figure 7 and Figure 8, left) with different thicknesses (Table 4). For the fabrication of this specimen a wooden formwork has been built.

Table 4: Areas with different thicknesses on Specimen 2.

Area 1: 169 mm (6.8")

Area 2: 369 mm (14.8")

Area 3: 319 mm (12.8") with minor thicknesses 264 mm (10.6")

Area 4: 271 mm (10.8")

Area 5: 510 mm (20.4")

Area 6: 319 mm (12.8")

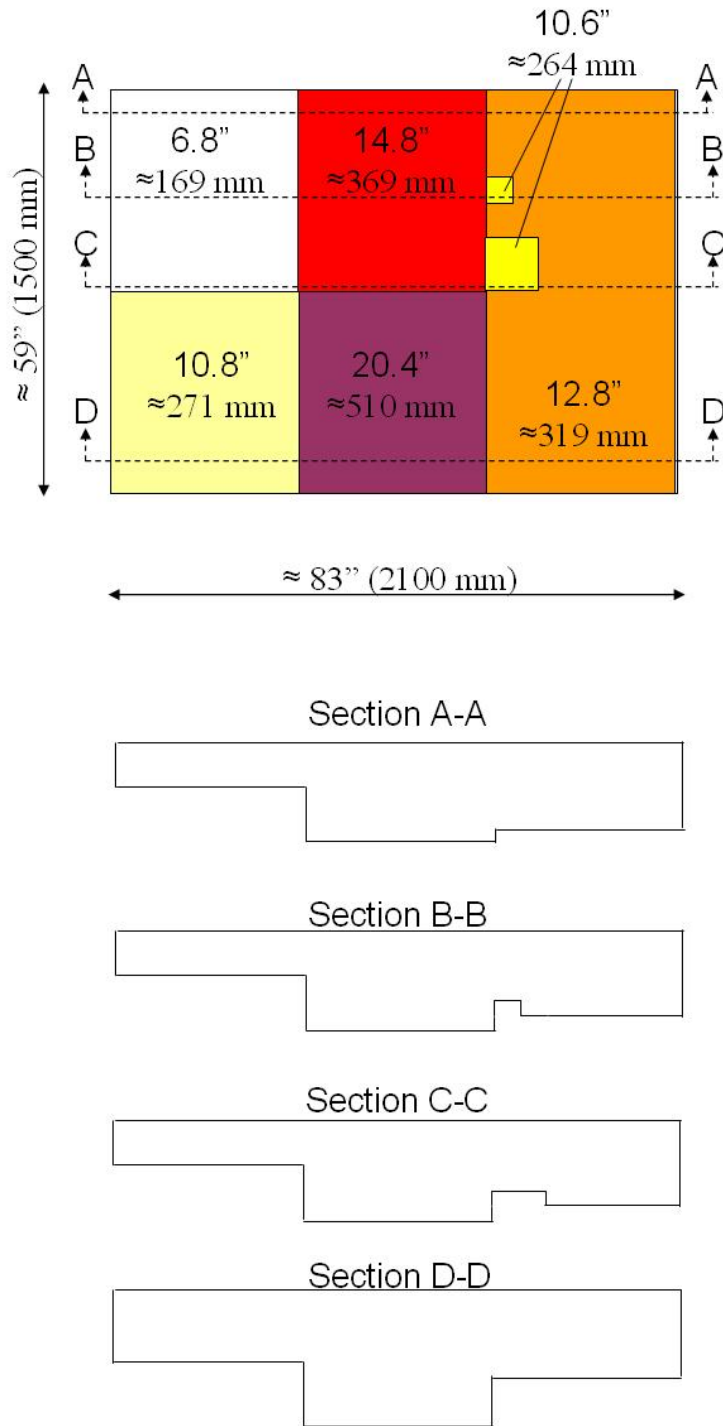


Figure 7: Sketch of Specimen 2 for the validation of thickness measurements. Top view and sections.

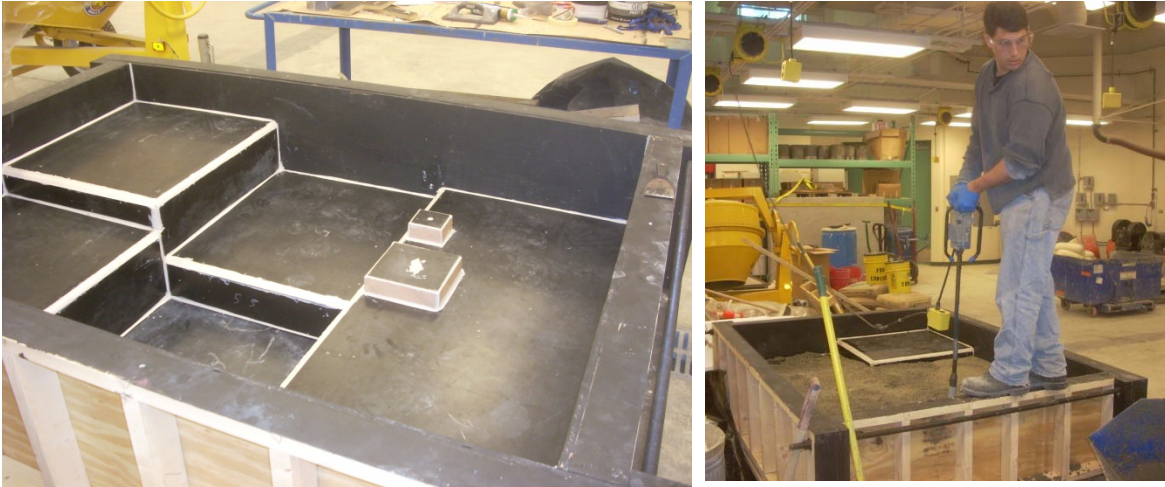


Figure 8: Specimen with varying thicknesses.
Left: Formwork.
Right: Pouring and compacting the concrete.

2.5 Specimen 3, Tendon Ducts

2.5.1 Considerations

A tendon duct inspection can be split up in basically two steps. The first is to detect the position of the duct; the second is obtaining information on the inside of the duct. Crucial points about localizing the duct in concrete are:

- a) Can the duct be localized in 2D, i.e., in its lateral position?
- b) Can it also be located in depth?
- c) Is there a certain minimum diameter that the duct needs to have to be detectable?
- d) Is this minimum diameter also dependent on the depth of the duct?
- e) ...or the thickness of the specimen?
- f) ...or both?
- g) Does it make any difference if having to deal with just a single duct or also further ducts next to it?
- h) Is it possible to detect a duct that is located behind another one (second layer)?
- i) Tendon ducts can be made of different materials, steel or plastic, with different acoustic as well as electromagnetic properties.

Concerning the detection of voids in the grout, the crucial points are:

- j) How to build realistic voids in a test block?
- k) Dimensions of the void inside the duct
- l) Location of a void in the duct?
- m) Reinforcement over the duct
- n) Thickness of the specimen
- o) Geometry of the specimen

p) Bonding between the grout inside the duct and the duct itself

Taking into account all the points listed above would require an enormous number of different specimens. It was therefore decided to focus on just a few aspects to demonstrate and study the process of a tendon duct inspection in general.

2.5.2 Design

A specimen with four ducts that are partially grouted has been designed (Figure 9). There are three prestressing (not under tension though) steel strands in every one of the ducts. To minimize the risk of misinterpretation due to geometry effects, the ducts were placed at a slight angle and not parallel to the edges of the block. The ducts have nominal inner diameters of 50 mm and 75 mm (2" and 3"). For each diameter there is one duct at a depth of half the block thickness, i.e. at the center of the block, and one that is slightly off-centered. The measurements can be conducted from both sides of the specimen.

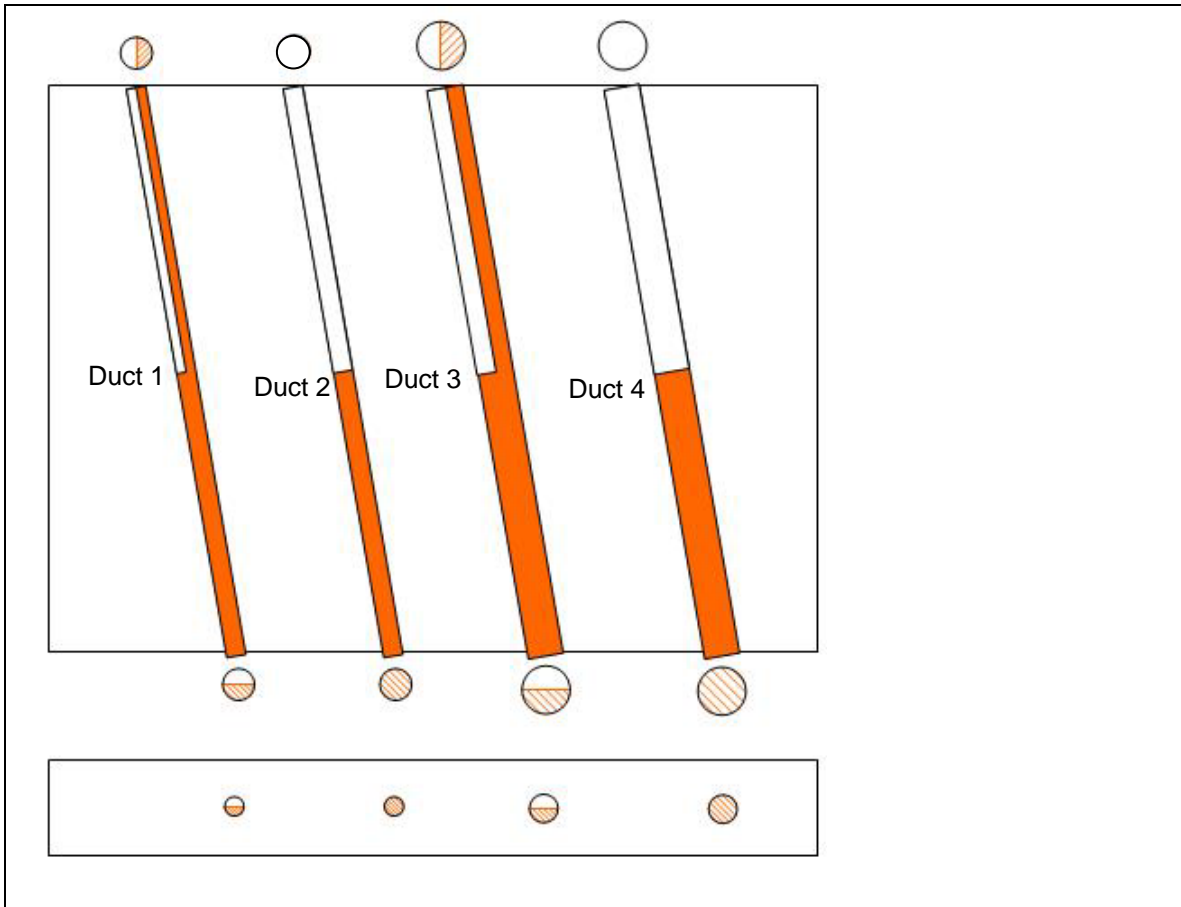


Figure 9: Specimen 3 with four parallel ducts, 2" (50 mm) and 3" (75 mm) nominal diameter. The ducts are not parallel to any of the edges of the specimen to avoid misinterpretation of the results due to geometry effects.

Every duct consists of two sections. For each pair of ducts with the same diameter, there is one duct, which is only partially (50% of its cross section) grouted, with a vertical orientation of the void over half the length of the duct and a horizontal orientation over the other half (ducts 1 and 3). The other two ducts, ducts 2 and 4, are fully grouted over half the duct length; the other half of the duct is empty.

Tendon duct inspections in general are highly dependent on the bond of the grout with the duct. Normally, with acoustic methods such as ultrasonic-echo or impact-echo, it will not be possible to detect a void in the grout if the grout is not bonded with the duct wall. The reason for that is that the acoustic wave will be reflected at the debonded area, i.e., at the thin air gap between the metal wall of the duct and the grout. It will not be possible to distinguish this reflection from a reflection at a “real” void in the grout.

The construction process is illustrated in the photos in Figure 10. In trying to achieve good bond between the grout and the duct, the ducts were grouted or partially grouted before they were put in place. For the partially grouted sections of the ducts, both openings of the respective duct sections were closed with caps in the shape of a half-circle over half the cross sectional area of the duct and the grout was filled in. Once the grout was hardened, the caps were removed and the two different sections of the duct, both half grouted, one in horizontal orientation, the other one in vertical orientation, were connected and put in place in the formwork.

The fully grouted sections of the ducts were closed at one side, and to achieve good bond between the grout and the duct wall, they were stood upright when the grout was poured. They were stored in that position until the grout was hardened. Then they were connected to the other half of the duct, which is the empty section, and put in place in the formwork. The ends of the ducts were sealed to the formwork with epoxy to prevent material from getting inside the duct when the concrete is poured. This was done very carefully to avoid that epoxy will stick to the outside of the duct, which would mean an acoustic barrier similar to a thin air gap. However, at the junction of the two different sections of all four of the ducts, a short piece of plastic pipe is supporting the joint. It was taken into account that this might be an acoustic reflector and therefore affect the measurements. This is a tradeoff for the benefit of a simple and stable joint. The ducts were tied to a wooden support construction to ensure that they would not bend in the middle. The concrete was poured mostly by hand and compacted using vibrating cylinders. Finally, the surface was finished and cured.



1) Preparing the ducts that will be grouted over only half of their cross sectional area (partially grouted ducts).



2) Filling the grout into the duct sections that will be entirely filled with grout. Ducts standing upright to achieve a good bond between the grout and the duct wall.



3) Letting the filled duct sections rest until the grout is completely hardened.



4) Putting the ducts in place in the formwork



5) Pouring and compacting the concrete.



6) Finishing the surface.

Figure 10: Construction of Specimen 3 (tendon duct block).

2.6 Specimens 3-1 and 3-2, Additional Tendon Duct Blocks

In addition to the four blocks described above that were designed and built specifically for this project, there were two additional blocks (Figure 11) procured from the FDOT Structures Office in Tallahassee. They were designed several years ago for a similar purpose of the validation of techniques, to detect broken strands within the grout. The two specimens are very similar in design. The major difference is that Specimen 3-1 has a regular thickness of 200 mm (8") while Specimen 3-2 has a regular thickness of 400 mm (16").

These specimens have a very realistic (slightly rough and uneven) surface, built-in tendon ducts with steel strands and intentionally empty or only partially grouted sections. The positions of the different sections are known. Seven different types of voids within the grout can be found in the different sections of the ducts. Both specimens also have an anchor section. On top of the tendon ducts there is a mesh of rebars.

Due to their large dimensions and the detailed design and documentation, they are well-suited for validation measurements and fit in the project very well. The only problem is that they are too big and too heavy to be brought in the test frame, so that up to now only manual measurements can be conducted on them.



Figure 11: Specimens 3-1 (left) and 3-2 (right) with tendon ducts, intentionally built-in defects and anchorage areas.

2.7 Block Coordinate System

For a clear allocation of the measurement results to the respective positions or areas on the test object and especially to guarantee the reproducibility of the results, the definition of a rigid, intuitive and practical coordinate system is essential. When a scanner is used, an unambiguous coordinate system is necessary for the orientation of the scanner on the block. To describe the volumetric results obtained from the different testing methods, a 3D coordinate system is needed. To make working with the coordinate system as intuitive as possible, a coordinate system according to the left-hand rule has been chosen. The x-axis of the coordinate system is defined to run along the longest side of the test block (length-axis), the y-axis along the second longest (height-axis) and the z-axis along the shortest (thickness-axis) of the specimen. The origin of the coordinate system has to be defined in a way that all points within the volume of the test object have positive coordinates for all axes. This is illustrated in Figure 12, where the four possible origins and coordinate systems are shown.

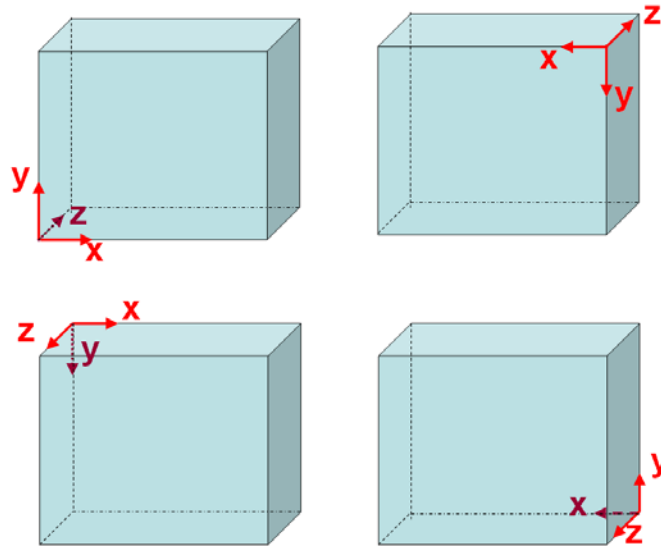


Figure 12: The four possible left hand rule coordinate systems. Either one of them is valid, the origin can be placed at one of the four corners for the coordinate system to be a left hand rule system and all points inside the object to have positive values on all three axes.

For every block used in this project, an origin has been defined and marked with yellow paint to make it permanent and guarantee that the results can be reproduced even after a long time after the block has been moved and tilted in the meantime. The importance of defining a permanent coordinate system will also be discussed in chapter 4.3 on the scanning system and its software.

3 Data Imaging

3.1 *B-, C -, and D-Scan Imaging*

Compared to the analysis of isolated waveforms obtained from single point measurements, imaging provides advantages in many respects. The interpretability of the data is enhanced when it is displayed as an image, since a direct allocation to the measurement situation becomes evident. Furthermore, it is an efficient way to handle the large amount of data obtained from measurements carried out in a dense grid.

A common imaging technique especially, for echo methods, is the use of A-, B- and C-scans ([24], [25], [26]) as it is depicted in Figure 13 for the impact-echo method. This technique requires a line or area scan, i.e., the data is collected along a line or a series of parallel lines with equidistant measurement positions. For every measurement position a waveform is obtained. The waveform is a function of reflected energy over time. According to the velocity of the transmitted wave, the time axis is related to the distance of the reflector. For impact-echo, which is based on multiple reflections, the time domain data is transformed into the frequency domain and the relation between resonance frequency and depth is used instead of the time information. In order to image the data, the waveform (or the frequency spectrum in the case of impact-echo) obtained at every measurement position is plotted using a grey-scale or color code. This plot is called the A-scan. By combining the series of A-scans along the scan line an image is obtained, which is referred to as the B-scan. As time (or frequency in the case of impact-echo respectively) is related to distance or depth, a B-scan can be interpreted as an image of the cross section through the test object along the scan line. For parallel scan lines a series of B-scans is obtained. This allows creating B-scans also perpendicular to the scan lines, which are then called D-scans. By creating a section at a certain time or frequency value through a series of B-scans, a view parallel to the surface is obtained, which is called a C-scan. This procedure can generally be applied to NDT methods that are based on the principle of an emitted pulse and the echo measured at the surface. It has been used routinely for non-contact methods like ground penetrating radar (GPR). Nowadays it is also applied for methods like impact-echo or dry-coupled ultrasonic-echo, which were originally designed for single point measurements. The measurements are still carried out point by point but along a scan line.

The identification of interfering effects and artefacts becomes possible when an image is analyzed instead of a single waveform. For example, impact-echo measurements carried out on test objects with compact dimensions will normally experience interference by reflections of surface waves ([29], [30], [31], [32]). These so-called geometry effects could not be identified in single point measurements. However, they become apparent as regular patterns in the image obtained from a scan line (Figure 14).

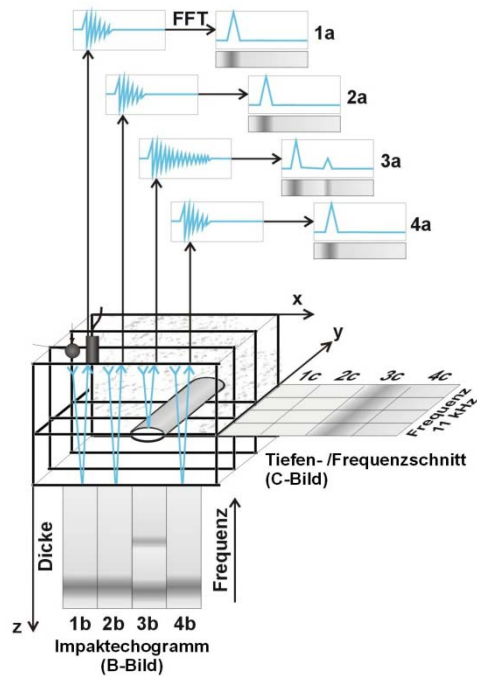


Figure 13: B- and C-Scan imaging illustrated for impact-echo data. (Source: BAM)

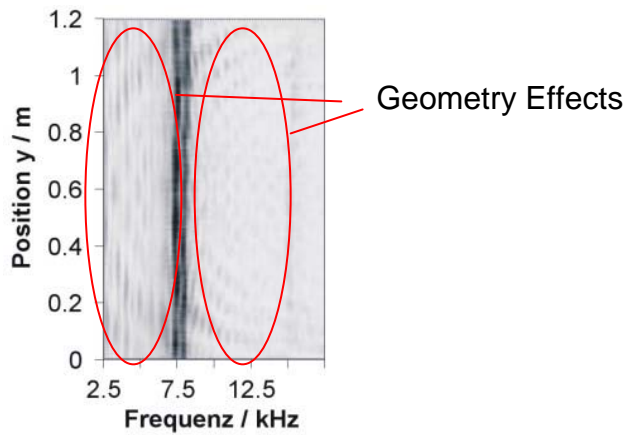


Figure 14: Geometry effects in an impact-echo B-Scan. These effects can only be identified in a scan, but in a single point measurement they would be misleading.

Lastly, picking the time sample with the maximum amplitude for every single one of the A-scans along the measurement area and plotting them in 3D over the respective measurement positions gives a thickness plot, which provides a vivid and relatively easy to interpret representation of the data.

3.2 Synthetic Aperture Focusing Technique (SAFT)

The synthetic aperture focusing technique (SAFT) is a powerful algorithm used in ultrasonic imaging. The SAFT algorithm has been successfully applied in many fields of engineering and medical diagnostics, and has also been used with great success in the field of NDE of concrete structures ([6], [7], [8]). The algorithm focuses signals received at many aperture points by coherent superposition [5]. Theoretical explanations, studies and introductions on this topic can be found for example in [6]. However, the functionality of the algorithm can as well be explained in a simplified and graphic way, which is illustrated in Figure 15 and explained in the following. This explanation might not be mathematically exact, however, it gives a general idea of how the algorithm works.

When scanning measurements are taken on a test object with a point-like reflector at the inside, this reflector will not appear as such in the B-scan. Due to the relatively wide divergence angle of the low frequency probes used in ultrasonic testing of concrete structures, the probe will receive a signal from the reflector even when it is not exactly over the reflector; however, the distance determined from that echo will be higher than the actual depth of the reflector in the object. The closer the probe is being moved to the actual position of the reflector, the closer the measured signal will get to the actual depth of the reflector. Plotting the measured distance over the position of the probe (B-scan) will give a hyperbola. When there is more than one reflector inside the object, the hyperbolas obtained from the different reflectors will interfere with each other so that it can become very hard to identify the different reflectors. The goal of the SAFT algorithm is to focus the hyperbolas obtained from the different reflectors back to the actual position of the reflector. This is being achieved in the following way:

- Plotting a circle with the measured amplitude around the probe position with a radius that equals the distance at which the amplitude was measured (measured distance that is).
- Doing so for every probe position along the scan line. The circles will intersect all at one point, which is the position of the reflector.
- By adding up the amplitude values of all the circles that cross a certain point, the highest amplitude will be obtained at the intersection point of the circles, i.e., at the position of the reflector.

This can be referred to as a simplification of the so-called heuristic SAFT in the time domain. This algorithm takes relatively long computation time compared to the Fourier transform based FT-SAFT that is used nowadays. The algorithm has been implemented in the software developed in this project and will be applied in the measurements.

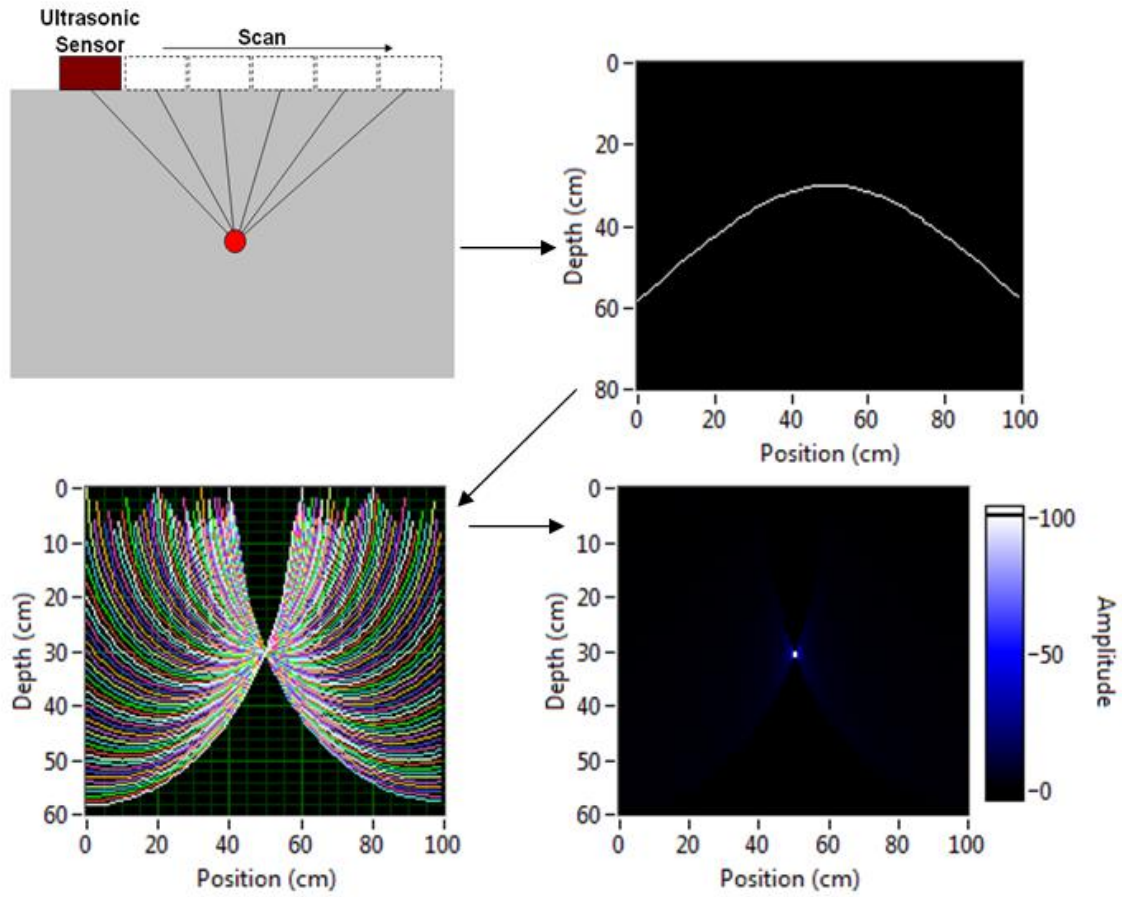


Figure 15: Simplified illustration of the SAFT algorithm.

4 Hard- and Software

4.1 Automated Testing Frame

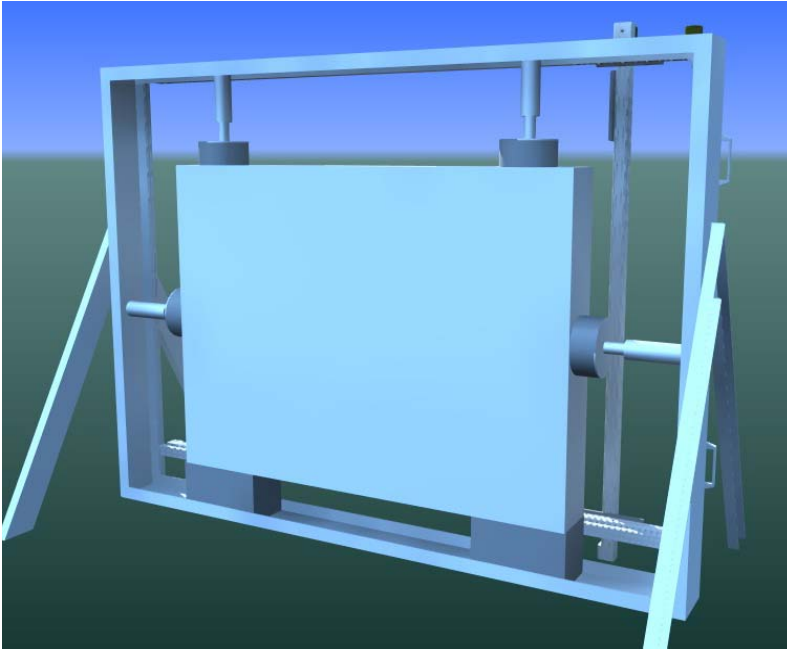


Figure 16:
CAD Visualization of the testing frame, consisting of scanners attached to a steel frame. The block is brought in the frame for measurement and is held in place by hydraulic cylinders.
(Picture by Florida Motion and Control)



Figure 17: The scanning system during operation in the laboratory at the State Materials Park, FDOT, Gainesville, FL.

The automated testing frame represents a major aspect of this project. The automation of the NDT technology makes it possible to:

- make the process of validation as objective as possible because the human factor is reduced to a minimum.
- collect an extremely large number of measurements and therefore create a meaningful statistical basis.
- visualize the data in images with high resolution.
- assure constant quality for all measurements.
- position the sensors very accurately.
- make the measurements reproducible.
- make the data collection as convenient as possible.
- reduce the measurement time to a minimum.

Since BAM, VIII.2 in Germany is the group with the most experience regarding the automation of technology in the field of NDT of concrete structures, it was the plan at first to purchase their latest large scale system for use in the laboratory. This could not be established due to legal restrictions that did not permit BAM to sell the system. Having a third party manufacturer build a duplicate of their system turned out to be not practicable either. Therefore, it was decided to design our own system in collaboration with a manufacturer in the state of Florida, *Florida Motion and Control*, and have them build and deliver the system. This solution turned out to be very practicable.

The design of the system is based on the design of the BAM systems; however, it was designed and adapted exactly to the needs and conditions at the FDOT facility. Furthermore, this system is not limited to the use in the laboratory only; it can as well be used in the field.

The main elements are a steel frame and two scanning systems. The steel frame holds the test blocks in place; the scanners are mounted on the frame. Because of their relatively large dimensions, the heavy weight of the specimens makes it necessary to provide a robust support for them while measurements are being taken. The blocks are secured in the steel frame by a system of hydraulic cylinders. The block is brought in the frame by a forklift. Then the four hydraulic cylinders get activated and secure the block. As a backup, the block is also held by four additional large screws that are secured manually. The scanners are mounted on the steel frame and provide scanning of the block from both sides. They can easily be removed from the frame and loaded on a truck for field applications. The system is therefore a very stabile system for the application in the laboratory in combination with the steel frame, but at the same time it is a mobile system which makes it very versatile and practical.

The sensors are moved by servo motor driven actuators in the x- and y-directions. In z-direction, a pneumatic cylinder presses the sensor against the block surface for measurement. The air pressure can be adjusted as needed for the different sensors. Holding brackets were designed to attach the different sensors to the scanners as stabile as possible, but at the same time give them the flexibility that is needed to self-adjust to the possibly uneven surface of the test object.

The pneumatic system for control of the movement in z-direction is activated and retrieved by a valve relay that can be switched by a 12 V logic (high/low) signal.

Position sensors give a 12 V logic signal to check if the sensor is at *in* or *out* position before the scanner is moved in x- or y-direction. This information is very important because otherwise, e.g., if there is a problem with the pneumatic system (e.g., air pressure is turned off) and the sensor head cannot be retrieved, the equipment could be severely damaged when the sensor scratches along the concrete surface.

4.2 NDT Sensors

An important criterion for the selection of the sensors was in how far they can be operated and synchronized with the scanning system. Therefore, it was necessary that the signals could be obtained either as analog signals from the sensor itself, or that a control device that comes with the sensor provides an interface to trigger it from outside (the scanner control program) and to retrieve the data as soon as they are measured.

Ultrasonic-Echo: Eyecon by ACSYS, distributed through Germann Instruments (Figure 18).

What makes this sensor so unique is that it is dry-coupled, i.e., no coupling fluid is necessary. It consists of two transducer arrays, 12 transmitting and 12 receiving transducers. The transmitters produce shear waves with a center frequency of 55 kHz. Their reflections are measured by the receivers. The transducers are bedded in an elastic foam/spring system, which assures that all sensors are coupled with the concrete, even when the surface is rough or slightly uneven.

The transmitting transducers are pulsed by a high voltage pulse generated by a handheld control device. The analog receiver signal is amplified and converted to a digital signal in the same control device. The pulses are transmitted with a repetition rate of 15 Hz, i.e., 15 measurements per second. The pulses are sent out nonstop; through a USB interface the currently measured signal can be retrieved by the control program.



Figure 18: Ultrasonic Echo System EYECON .

Left: Mounted on scanning system.

Right: Sensor head and handheld control device (source: ACSys).

Impact-Echo: IE1 by Olson Instruments (Figure 19).

This is an impact-echo sensor head, consisting of a transducer and an impactor. The impactor is driven by a solenoid. An electric pulse is applied to the solenoid, which fires a small steel impactor held by a spring. A control box creates the pulse for firing the solenoid and amplifies the analog signal received from the transducer. A trigger input makes it possible to fire the impactor by applying a 12 V logic pulse, and is thus well suited for automated use in combination with the scanning system. The amplified analog signal can be transferred to a DAQ system by a BNC cable.



Figure 19: Impact-echo sensor head IE1 manufactured by Olson Instruments.
Left: Mounted on scanning system.
Right: Transducer and impactor of the sensor head.

Covermeter: Profometer 5+ by Proceq (Figure 20).

This is a covermeter using eddy current technology to measure the depth of steel reinforcement bars. The sensor is connected to a handheld control box, where the signal is processed and the depth is determined. In a special agreement with the manufacturer, a modified EPROM has been provided. With this EPROM, the measured thickness values are constantly sent to a serial RS232 interface and can be read by the control program. The sensor comes with a little cart, which makes it possible to slide the sensor along the surface with a constant and very small gap between the sensor and the surface, just enough to ensure that the sensor is not getting damaged. For use with the scanner, the sensor is mounted on the cart, which is then mounted on the scanner.



Figure 20: Covermeter PROFOMETER 5+ by Proceq.
Left: Mounted on scanner.
Right: Sensor and handheld control device.

GPR: SIR 3000 Structure Scan by GSSI (Figure 21).

This is a GPR system consisting of a 2.6 MHz RADAR antenna mounted on a cart and a control device. At the moment, there is no interface that would make it possible to control the system from outside (the scanner control program) and to retrieve the data while it is being recorded. At the same time, the system works very well by itself and is the state of the art. Therefore, the idea is to let it run on the scanner but let the GSSI control device do the actual data acquisition and just download it when the scans are complete.

However, this would mean that the red button and the wheel that is supposed to be pressed down during the measurement will have to be fixed in the down position thus emitting electromagnetic waves over the continuous scanning and testing time. To ensure that this will not be harmful for people, it will still require certain adjustments and investigations.



Figure 21: SIR 3000 GPR System by GSSI

4.3 Software Development

To control the scanner, synchronize the measurement devices with the scanner, store and post-process the data, a software platform is needed. Precise synchronization of the measurement device with the scanner makes it not possible to use software that might come with the device and was designed for manual measurements. Therefore, a software platform that satisfies those needs had to be developed in the project.

4.3.1 Interfaces

The software was developed in the National Instruments Lab View measurement and control programming environment. Lab View is a graphical programming environment; instead of typing text based source code, the source code is completely icon based. Lab View shows excellent compatibility with various data acquisition systems, especially in combination with National Instruments hardware. It is widely used in the field of automation, data acquisition and signal processing.

The software controls the scanner servo motor through a serial RS232 interface. The commands concern the scan positions, scan speed, acceleration, etc. It controls the data acquisition through the PXI controller, or directly through a USB interface in combination with USB driver software as is the case with the ultrasonic echo device, or through an additional serial RS232 port, as is the case with the covermeter.

As indicated earlier in chapter 2.7, the selection of an adequate coordinate system is crucial especially when scanner measurements are being conducted. This is because the two coordinate systems, scanner and block coordinate system have to be adjusted to each other. The normal scenario will be that a certain block is supposed to be scanned and the block coordinates for this area will have to be determined. Now the scanning system needs the information that is necessary to scan the selected area on the block. Therefore, it has to be known at which position of the block the scanner has its origin and how it is orientated. Handling two coordinate systems can become quite complex. Therefore, the software was designed in a way that it walks the operator through the scanner and coordinate system setup step by step, which makes the setup easy and precise.

4.3.2 Operation

The software was designed to make the scanner control and data acquisition as intuitive and easy as possible. Figure 22 shows the main window of the software during data collection. A 3D graphic illustrates the measurement situation, the block geometry, scan grid, orientation of the scanner in the block coordinate system and the current measurement position. For every measurement position the acquired waveform is displayed. The B-scan image is obtained in real-time during the measurement in progress. The estimated remaining time to finish the measurement is displayed and updated at every measurement position.

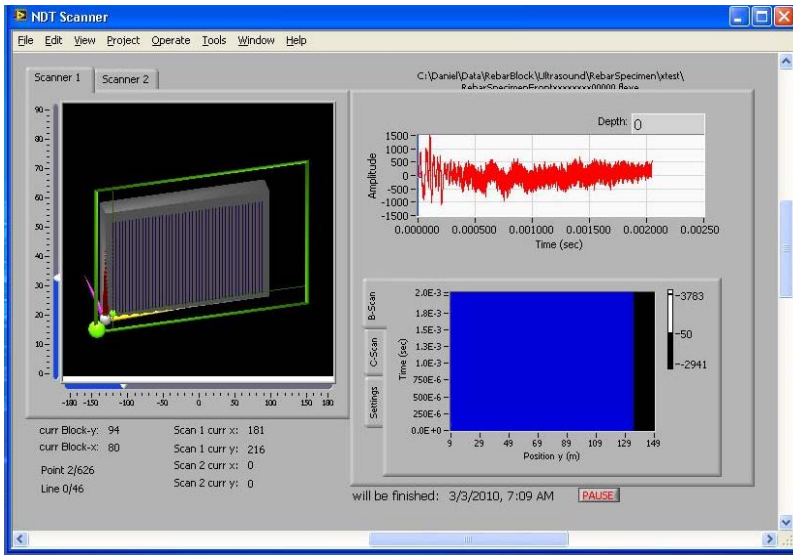


Figure 22: Measurement window

As complex as the scanner/block geometrical setup can get in general, and underneath the user interface of the program, it has been the intention to hide this complexity from the user and make it appear as simple as possible. The program guides the user through the scanner and DAQ setup step by step, starting with the selection of the COM-ports for the scanner control (Figure 23).

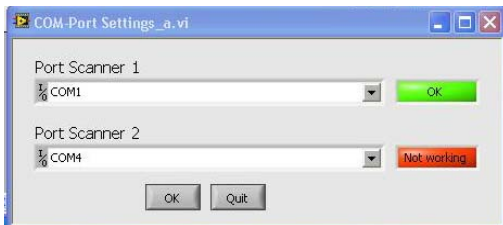


Figure 23: COM port selection for scanner control

In the next step, the functionality of both scanners as well as the pneumatic system, which is needed to press the sensor against the surface of the block, can be checked by joystick like arrow buttons in the program (Figure 24).

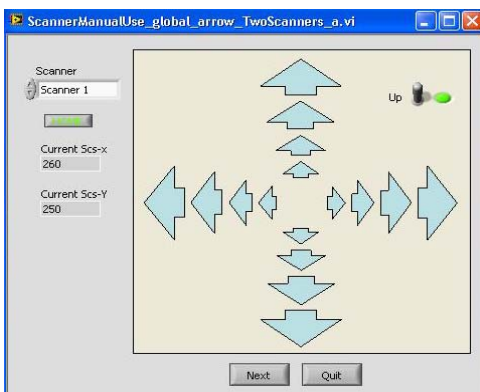


Figure 24: Joystick scanner control for scanner test and setup.

The geometry of the block can be edited and stored under the block identifier and is displayed in either a 3D illustration of the block or a plan view (Figure 25).

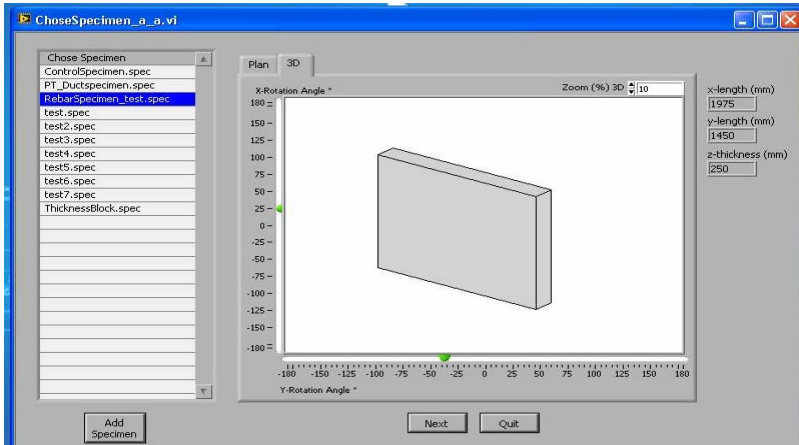


Figure 25: Selection or creation of specimen geometry. Storage of the geometry by specimen identifier.

Three simple dialogs provide the program the information it needs to define the scanner/block geometry and orientation. With the arrow buttons the scanner can be moved precisely to the origin of the block coordinate and the setup is saved (Figure 26). No complicated calculations or coordinate transforms are required from the user to define the position of block origin in the scanner coordinate system.

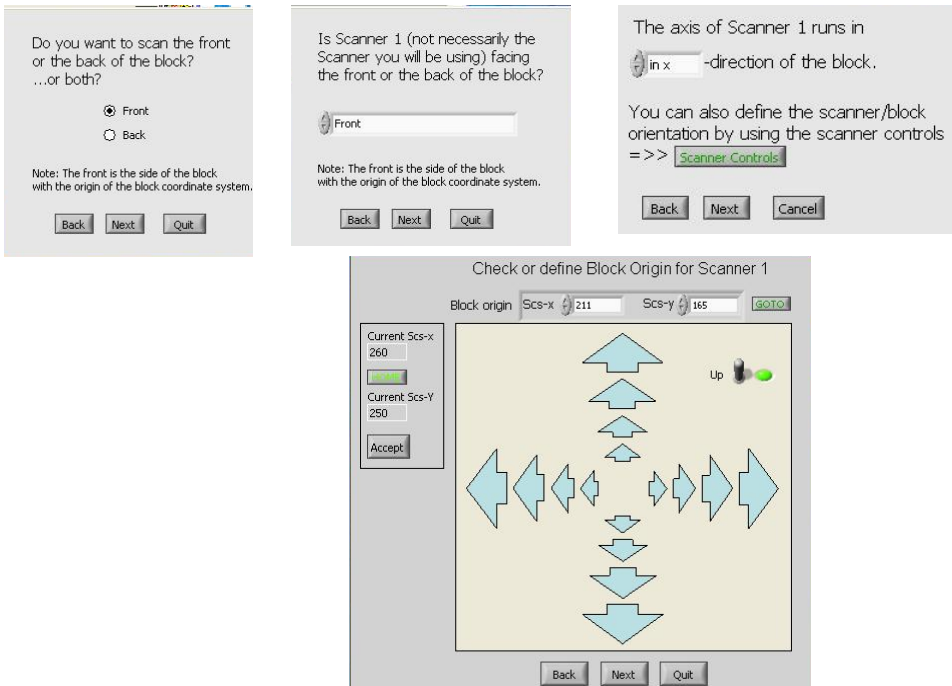


Figure 26: Easy scanner setup, just a few dialogs and an intuitive, joystick based selection of the block origin, thus avoiding complex handling of coordinate system.

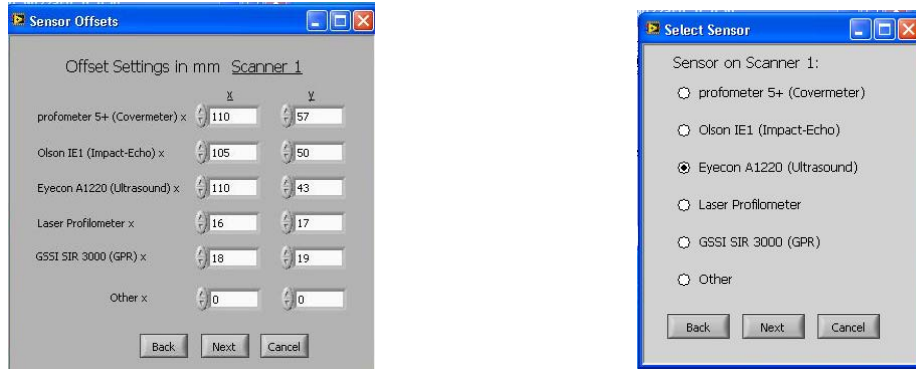


Figure 27: Entering and storing the sensor specific offsets simplifies the scanner setup. Block origin and coordinate system have to be defined only once and remain the same for all sensors.

Instead of having to adjust the block origin every time the sensor is changed, it has to be adjusted only once and the coordinate offsets for the different sensors (Figure 27) are automatically added by the program when needed.

The measurement grid is defined by the start coordinates and the x- and y-increments per point along a scan line, the x- and y-increments per scan line and the number of scan lines and points per scan line. Based on those parameters the scan grid is displayed in a 3D illustration that can be freely rotated (Figure 28).

As an alternative to defining the grid by point and line increments, a grid wizard can make the setup even easier. With the arrow buttons the scanner is moved to the four corners surrounding the grid and the point and line distance is entered. Either way the settings can be checked in a test run before the actual measurement is started. There the scanner moves along the outline of the scan grid. This serves to check again that the grid is defined correctly and that the scanner can reach all points of the grid without getting damaged by cables or other objects that might be in the way.

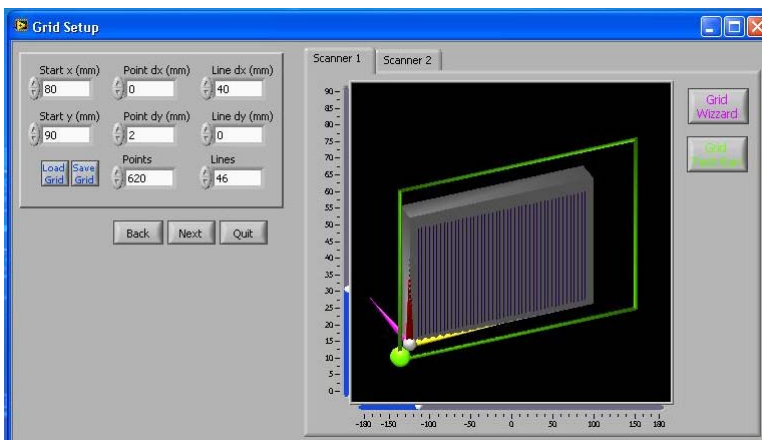


Figure 28: Intuitive 3D graphic based setup of the measurement grid.

Finally, before the measurement is started, the DAQ parameters can be adjusted according to the needs for the measurement and the functionality of the sensor can be tested by acquiring test waveforms (Figure 29).

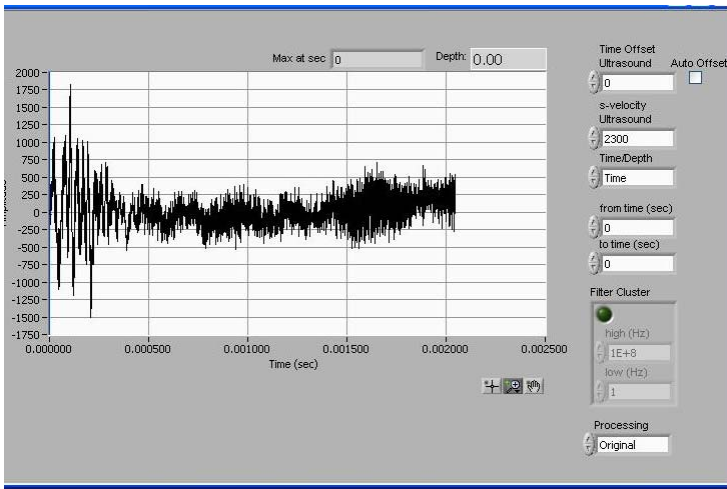


Figure 29: Sensor check and parameter adjustment before the measurement is started.

When the setup is finished, the measurement starts. The scanner runs completely automated so that measurements can be taken overnight or even over days or weeks, the only limitation being the capacity of the storage device. The data is imaged in B- and C-scans in real-time and can be analyzed while the measurement is running.

5 Measurements on Laboratory Specimens

Scanning measurements were performed on all four laboratory specimens. The blocks were brought in the test stand using a forklift and held in place by the hydraulic securing system. Impact-echo as well as ultrasonic-echo measurements were conducted on all four blocks. In addition, covermeter measurements were carried out on block 1 (reinforcement block) and block 3 (tendon ducts). Prior to the covermeter measurements, the functionality of the device was studied in calibration experiments that were conducted on a small control block with a single rebar in it. The measurements and the results obtained will be described in the following.

5.1 Control Block, Reference Measurements

5.1.1 Impact-Echo

Automated impact-echo measurements (Figure 30) were taken along 94 scan lines with 65 measurement positions per scan line (grid of 20 mm × 20 mm, 0.8" × 0.8"), resulting in more than 6000 measurement positions per side.

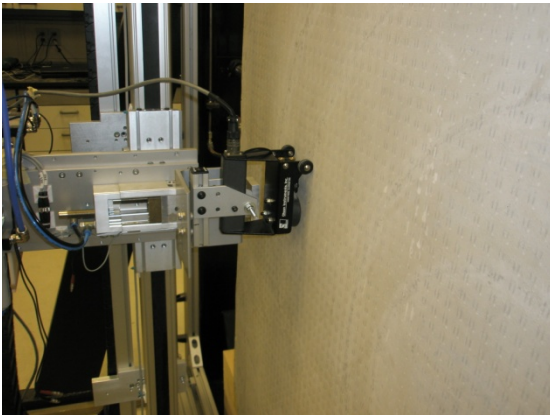


Figure 30: Automated impact-echo measurements.

Figure 31 shows an example waveform, the averaged frequency spectrum is shown in Figure 32, in which the thickness indication at 8.69 kHz can be identified. With a known block thickness of about 104" (260 mm), a longitudinal wave velocity of $c_L = d \cdot 2f = 0.26 \cdot 2 \cdot 8690 = 4519 \text{ m/s}$ is obtained, which is relatively high due to the low density of the material.

Figure 33 shows the averaged B- and D-scans obtained. Herein the backwall reflection and also the geometry effects, i.e., reflections of especially the Rayleigh waves ([29], [30], [31], [32]) at the edges of the specimen, which are typical for impact-echo measurements, become clearly visible. Since this is a solid specimen with no defects or other objects built in, it is clear that all indications appearing in the scans have to be

either backwall reflections (intended) or geometry effects. This will help to avoid misinterpretation of the results obtained from the other blocks because they can always be compared with the results obtained on this control block. Especially when looking at the C-scans given in Figure 35, the misleading effect of the geometry effects becomes clear. Although this is a solid specimen with no objects or voids built in, there are indications occurring over the entire frequency range. The backwall reflection appearing at around 8.69 kHz is actually the only indication that would normally be used in the interpretation of impact-echo measurements. The geometry effects occurring in all other C-scan images can be identified as such because they appear as regular patterns, which become smaller with increasing frequency. As challenging as it may be to identify these effects in measurements taken in practice, only in scanning measurements can they be identified at all. In single point measurements where the data is analyzed as isolated waveforms, they could easily be misleading.

Figure 34, left, gives a 3D representation of the measured thicknesses over the measurement positions. The surface obtained is mostly even and shows a slight increase in thickness towards the middle, which can be assumed to be the natural variation in concrete thickness. For the histogram (Figure 34, right) a mean value of 239 mm (0.96”) with a standard deviation of 25 mm (1.0”) is obtained.

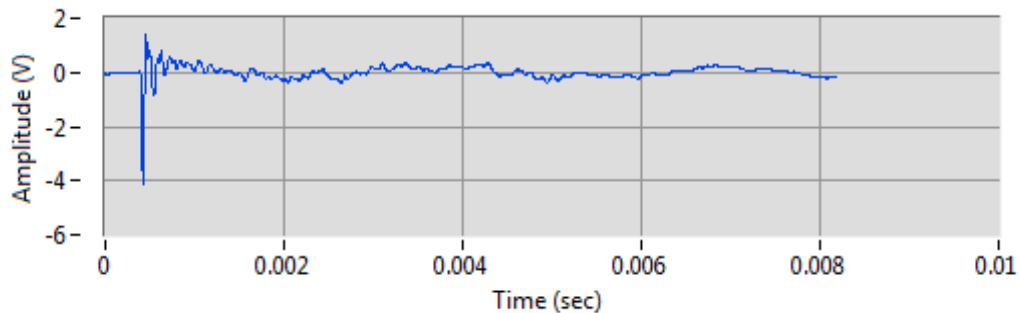


Figure 31: Example of an impact-echo waveform.

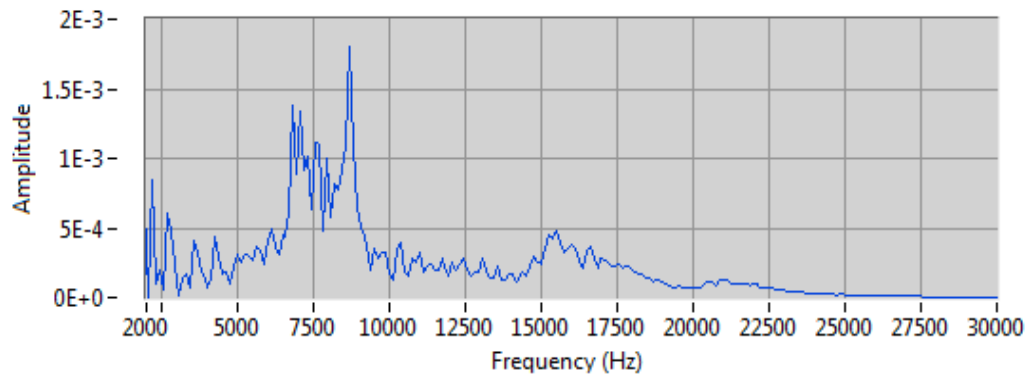


Figure 32: Example of an impact-echo frequency spectrum.

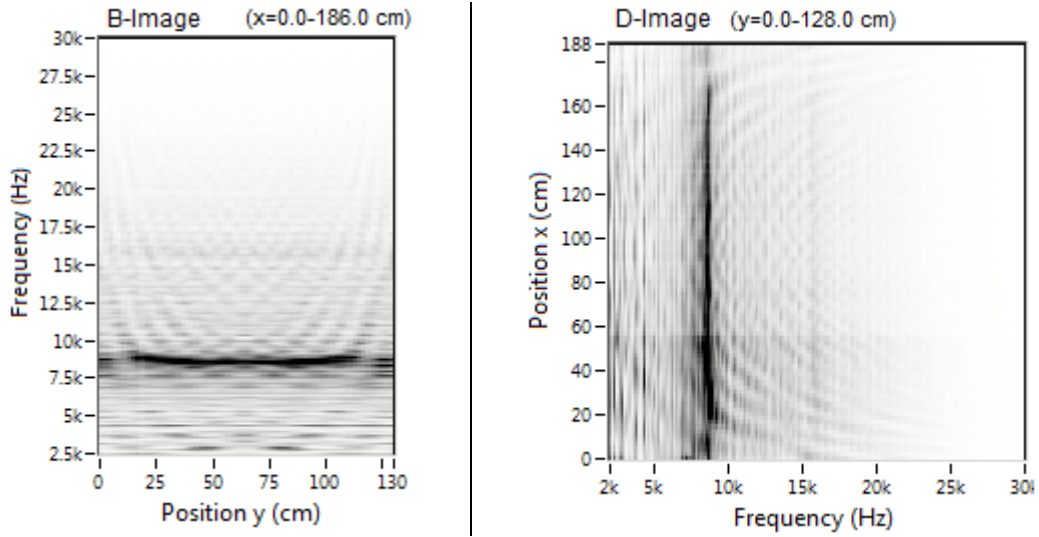


Figure 33: Averaged impact-echo B-scan (left) and D-scan (right).

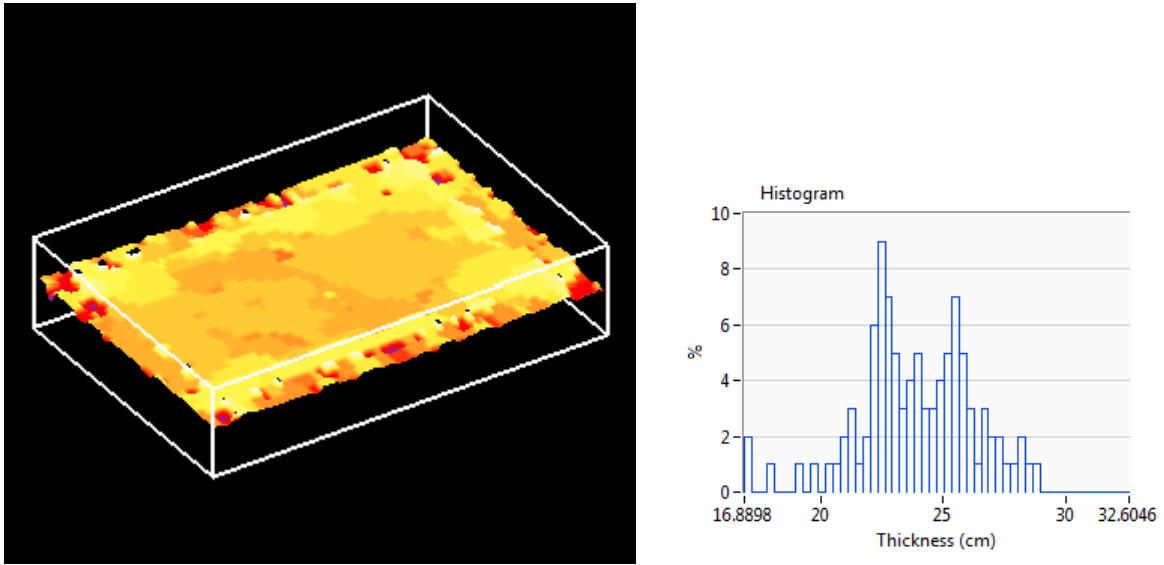


Figure 34: Impact-echo results.
 Left: 3D plot of the measured thicknesses over the measurement position.
 Right: Statistical distribution of the results.

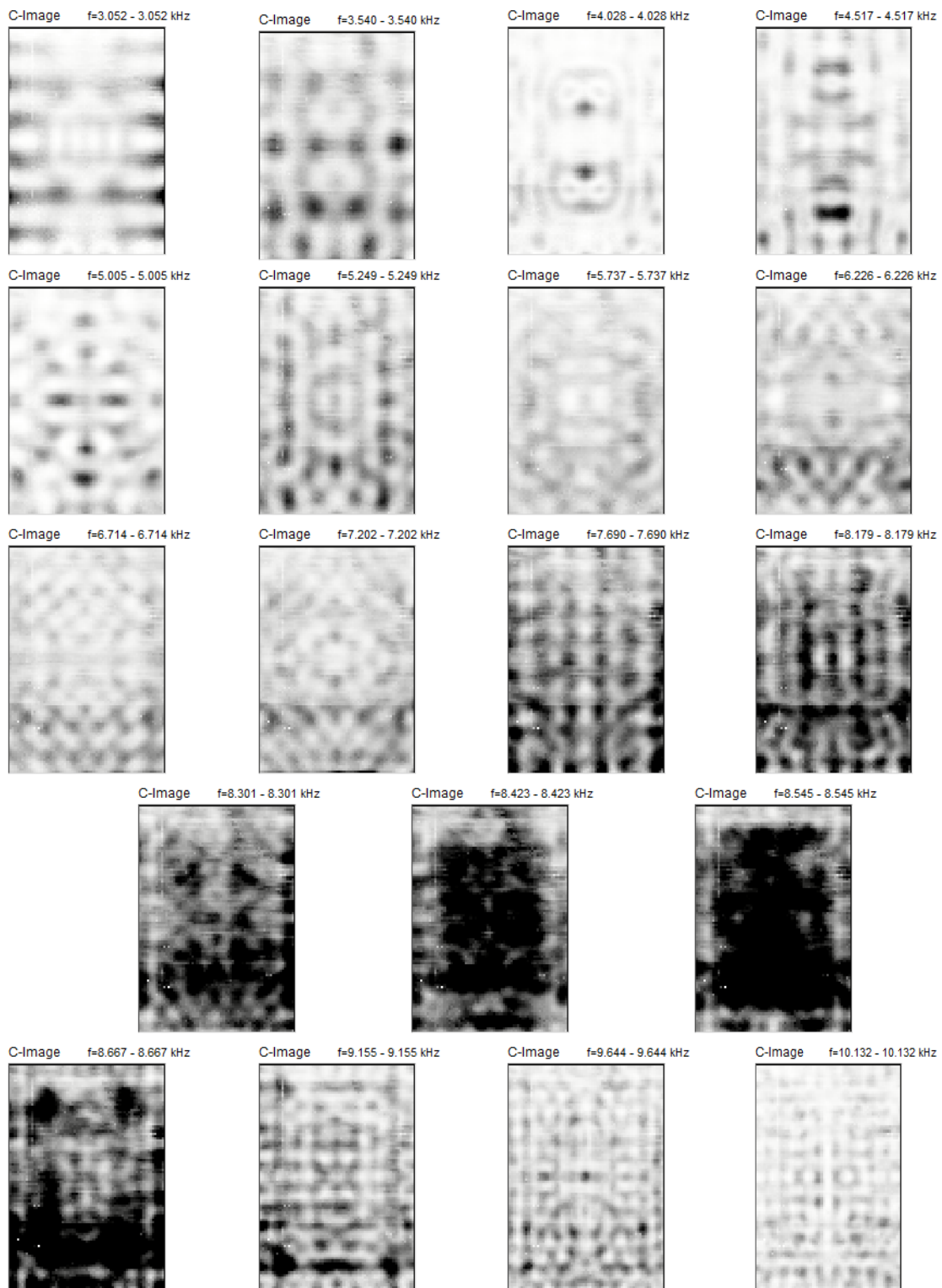


Figure 35a: C-Scans obtained from impact-echo measurements on Specimen 0-0.



Figure 35b: C-Scans obtained from impact-echo measurements on Specimen 0-0.

5.1.2 Ultrasonic-Echo Measurements

The ultrasonic-echo measurements (Figure 36) were conducted along the same grid as the impact-echo measurements. Figure 37 gives the waveform (HF signal) averaged over all measurement positions. From this a shear wave velocity of 2712 m/s can be determined. The averaged B- and D-scans (averaged over all B/D-scans) are shown in Figure 38.



Figure 36: Automated Ultrasonic-echo measurements.

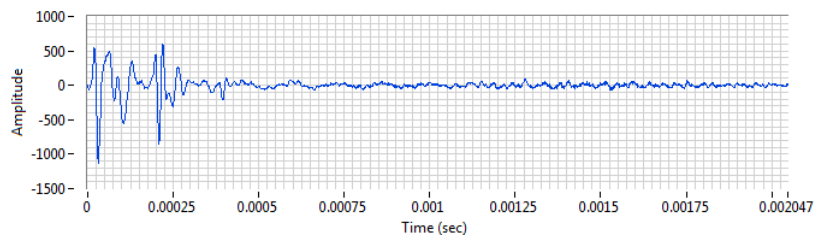


Figure 37: Averaged waveform, ultrasonic-echo.

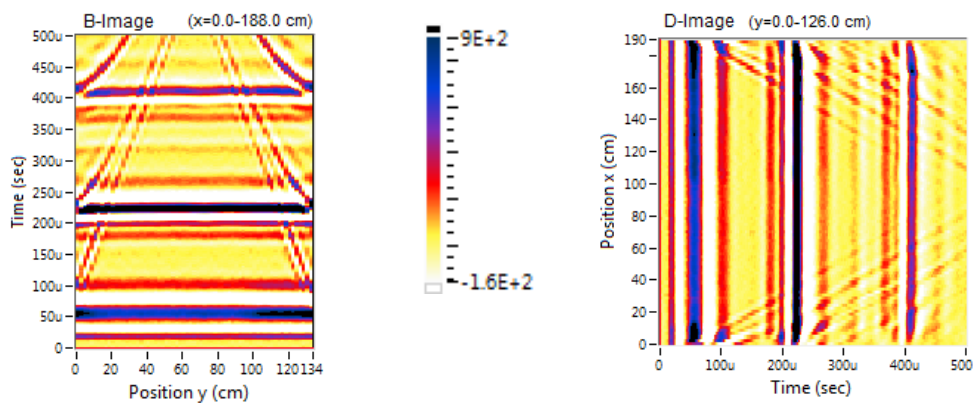


Figure 38: Averaged ultrasonic-echo B-scan (left) and D-scan (right).

Figure 39 gives a 3D representation of the measured thicknesses over the measurement positions as well as the statistical distribution with a mean of 261 mm (1.04”) and a standard deviation of 6 mm (0.024”).

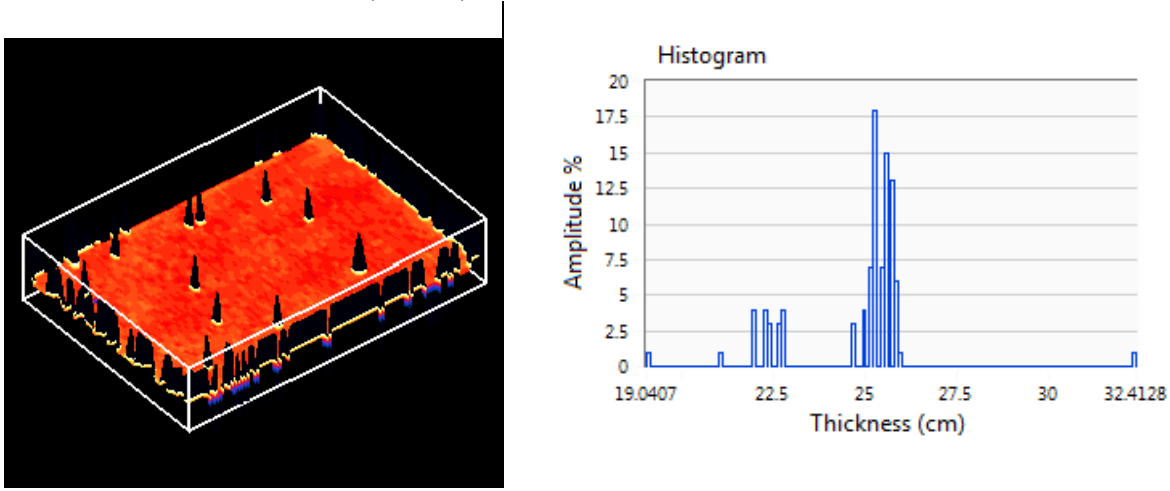


Figure 39: 3D plot of the measured thicknesses over the measurement position, ultrasonic echo.

The standard deviation obtained from ultrasonic echo is significantly lower than for impact-echo. A reason for that might be the influence of the geometry effects that impact-echo suffers from. The data collected on this block will be further discussed in chapter 6, where it is used to determine the elastic parameters of the concrete based on the longitudinal and shear wave velocity.

5.2 Covermeter Calibration Experiments on a Small Concrete Block with Rebar

To study the effect of certain parameters, such as rebar depth, rebar diameter, orientation of the probe and adjacent rebars, some preliminary experiments were carried out on a small calibration block (Figure 40).



Figure 40: Small concrete block with a #4 rebar for covermeter calibration.

Its dimensions are about 254 mm x 254 mm x 127 mm (10'' x 10'' x 5'') and contains a single #4 rebar. The rebar is located so that its concrete cover is 25 mm (1.0'') from one side of the specimen, 50 mm (2.0'') from the second side, 100 mm (4.0'') from the third side and 200 mm (8.0'') from the fourth side. Since the measurement depth of the modified device is limited to 80 mm (3.2''), only two of the sides on this block (25 mm and 50 mm cover, 1.0'' and 2.0'') will be used for the calibration experiments.

5.2.1 Calibration Experiment No. 1, Rebar Depth

This experiment served to investigate the accuracy with which the concrete cover over a rebar can be measured. The probe was positioned on the side of the control block with a 25 mm (1.0'') concrete cover, in parallel polarization and exactly over the center of the rebar. The diameter of the #4 rebar was entered in the handheld controller device and a concrete cover of 27 mm (1.08'') was measured, which is 2 mm (0.08'') higher than the actual concrete cover. The 2 mm (0.08'') difference is caused by a pad underneath the probe, which is supposed to protect it from damage, as well as a little gap between the probe and the concrete surface when the probe is mounted on the little cart. It will be referred to as the pad offset in the following, and has to be taken into account and subtracted from the readings for the concrete cover. Next, the concrete cover (distance to the rebar) is increased step by step by adding non-metallic spacers between the probe and the surface of the concrete block (Figure 41).

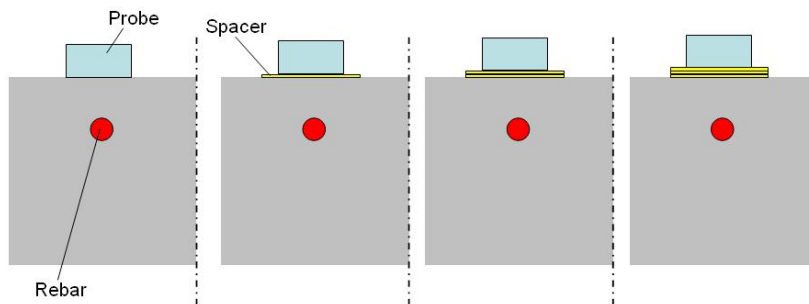


Figure 41: Calibration Experiment, increasing the distance between the probe and the rebar (cover) step by step by adding non-metallic spacers.

The readings for the different concrete covers (Table 5) confirm the 2 mm (0.08'') pad offset. Other than that, they differ from the actual concrete cover by no more than 1 mm (0.04''). Figure 42 shows the linearity of the concrete cover measurements (left) and the hyperbolic relation between the amplitude and the concrete cover (right). As a rough estimate, it can be derived from the data that doubling the concrete cover from 27.0 mm (1.08'') to 53 mm (2.12'') reduces the signal amplitude from 139.9 a.u. to 8.6 a.u., which is a factor of roughly 16. For both curves the pad offset has not been subtracted and is still included in the results.

Furthermore, to investigate how far a false rebar diameter setting on the device would affect the measurement, the experiment was repeated as described above but with false diameter settings. Instead of the actual rebar diameter of 13 mm (0.52''), the diameter was set to 19 mm (0.76'') and 10 mm (0.40''). The results were obtained as given in Table 6

Table 5: Measured covers and amplitudes obtained for a reinforcement bar with a diameter of 13 mm, incrementally increasing the cover.

Rebar Size Setting on the Device (mm)	Metric Bar Size (mm)	In-Lb Bar Size	Cover (mm) (actual distance between probe and rebar)	Measured Cover (mm)	Signal Amplitude (a.u.)
13	13	#4	25.0	27	139.9
13	13	#4	31.4	34	61.8
13	13	#4	37.8	40	29.6
13	13	#4	44.2	46	15.7
13	13	#4	50.6	53	8.6
13	13	#4	57.0	59	5.1

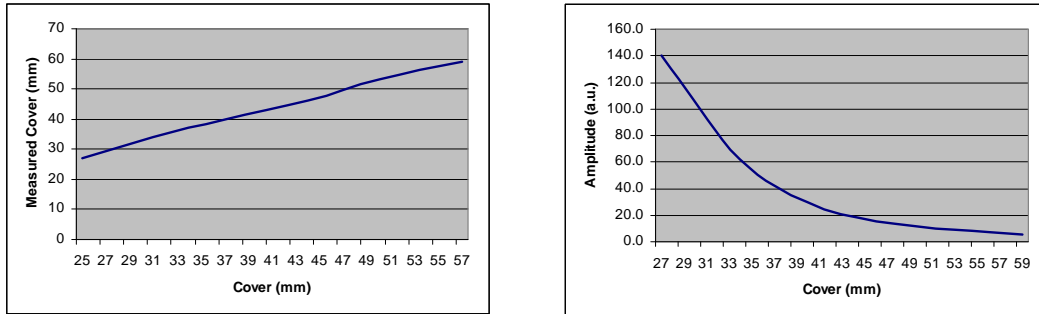


Figure 42: Curves obtained by increasing the distance between the probe and the rebar (concrete cover) step by step. The curves describe the measured cover (left) and the amplitude of the signal (right).

and Table 7. It can be seen that the signal amplitude is independent from the (estimated) rebar size settings on the device. However, the value that is obtained for the concrete cover changes indeed when the rebar size setting is changed on the device. The concrete cover is calculated internally based on the signal amplitude and the rebar diameter. In other words, high signal amplitude can be caused by a rebar even with a smaller diameter but located near the probe, or as well by a rebar that is a little further away but has a significantly larger diameter. In both cases, the 10 mm (0.40”) setting as well as the 19 mm (0.76”) setting, the 2 mm (0.08”) pad offset still needs to be subtracted from the results. With the pad offset taken into account, a false rebar setting on the device would result in measuring a cover that is too low in the case of the 10 mm (0.4”) setting, and too high in the case of the 19 mm (0.76”) setting.

Table 6: Measured covers and amplitudes obtained for a false diameter setting of 19 mm (0.76”) instead of 13 mm (0.52”).

Rebar Size Setting on the Device (mm)	Metric Bar Size (mm)	In-Lb Bar Size	Cover (mm) (actual distance between probe and rebar)	Measured Cover (mm)	Signal Amplitude (a.u.)
19	13	#4	25.0	29	135.6
19	13	#4	31.4	37	60.3
19	13	#4	37.8	43	29.4
19	13	#4	44.2	51	15.0
19	13	#4	50.6	58	8.1
19	13	#4	57.0	64	4.9

Table 7: Measured covers and amplitudes obtained for a false diameter setting of 10 mm (0.4”) instead of 13 mm (0.52”).

Rebar Size Setting on the Device (mm)	Metric Bar Size (mm)	In-Lb Bar Size	Cover (mm) (actual distance between probe and rebar)	Measured Cover (mm)	Signal Amplitude (a.u.)
10	13	#4	25.0	25	135.2
10	13	#4	31.4	32	62.5
10	13	#4	37.8	38	30.6
10	13	#4	44.2	45	15.8
10	13	#4	50.6	50	8.8
10	13	#4	57.0	56	5.0

In summary, this experiment showed that:

- There is a 2 mm (0.08”) pad offset that has to be subtracted from the measured cover.
- The measurements remain mostly linear when the concrete cover is increased (note that this experiment was conducted on a block with only a single rebar inside; adjacent rebars will affect the accuracy).
- There is a hyperbolic relation between the concrete cover and the amplitude of the received signal. Increasing the concrete cover by a factor of 2 reduces the amplitude by a factor of roughly 16.
- Slight changes in amplitude will hardly have an effect on measurements in the low cover range, but will have a significant effect when the concrete cover is near the maximum limit of the measurement range of the device.
- A false diameter setting in the menu of the device will not affect the signal amplitudes measured but will indeed affect the resulting values for the concrete cover. Estimating the rebar diameter too high will result in concrete cover being measured too high, while underestimating the rebar diameter will result in measuring the concrete cover too low.

5.2.2 Calibration Experiment No. 2

The probe was scanned manually along the four sides of the specimen. The scans were carried out along a line with a distance of 2.5 mm (0.1”) between the consecutive points. Two different probe polarizations, parallel as well as perpendicular to the rebar orientation, were used (Figure 43). The parallel polarization is the polarization that should be used during actual measurements for the probe to give meaningful data, because the response in parallel polarization is significantly stronger than in perpendicular polarization. However, in perpendicular polarization, a (weaker) response is still received. This means that a second rebar layer running perpendicular to the rebars in the layer that is actually being measured, will affect the measurement. The experiment is supposed to determine to what extent the measurement will be affected.

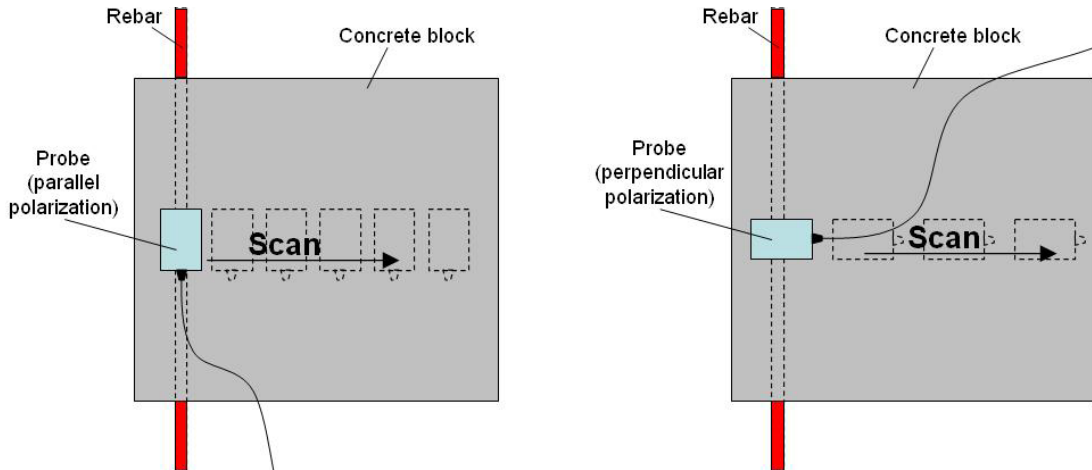
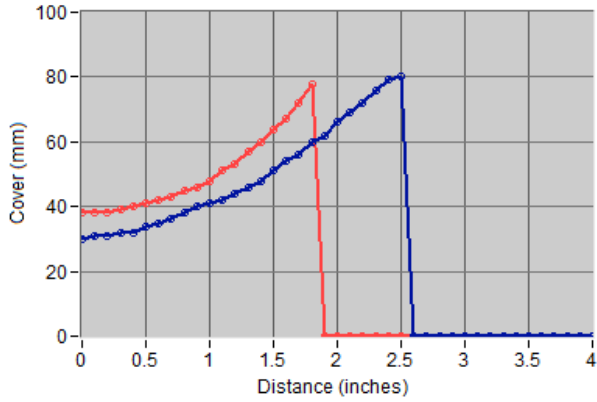


Figure 43: Calibration experiment, scanning the probe along the surface, away from the rebar, measuring the signal strength in relation to the probe position, determining up to what distance the rebar still has an effect on the measurement.

Figure 44 gives the measured cover over the distance along the surface in parallel polarization (blue curve) and perpendicular polarization (red curve) to the rebar with an actual concrete cover of 25 mm (1"). In parallel polarization and with the probe positioned right above the rebar (distance = 0), a value of 30 mm (1.2") for the concrete cover is obtained. The measured value increases with distance until it reaches a value of 80 mm (3.2"). This is the maximum value that can be obtained from the device in the automatic mode, for any value above 80 mm (3.2") a value of zero will be obtained instead.

In perpendicular polarization and with the probe positioned right above the rebar (distance = 0), a concrete cover of about 39 mm (1.56") is measured. This is because of the "wrong" polarization. Although the measured cover is higher than the actual cover, which means that the intensity of the response is lower, there is still a response received in this polarization. Increasing the distance along the surface gives a curve (red curve) that is above the curve obtained in parallel polarization (blue curve). After reaching a value of 80 mm (3.2"), it drops to zero. This does not necessarily mean that the response is exactly zero, it is just set to zero internally.

Figure 45 gives the measured signal amplitudes for the calibration curves shown in Figure 44. The relation between signal amplitude and concrete cover becomes even clearer in Figure 46, where the signal amplitude is plotted over the measured concrete cover. The hyperbolic relation becomes clear herein. For different rebar diameters, this curve would have to be adapted accordingly. The effect of the rebar diameter on a covermeter measurement will be demonstrated in calibration experiment no. 3.



**Figure 44: Concrete cover calibration curve taken on a rebar with a 25 mm (1") cover.
 Blue curve: parallel polarization of the probe
 Red curve: perpendicular polarization of the probe**

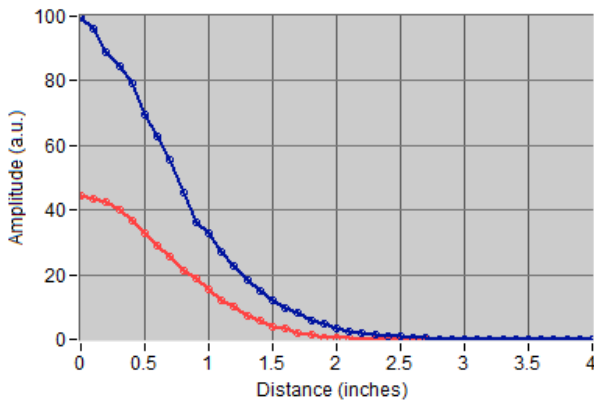


**Figure 45: Signal amplitude calibration curve at a rebar with a 25 mm (1") cover.
 Blue curve: parallel polarization of the probe
 Red curve: perpendicular polarization of the probe**

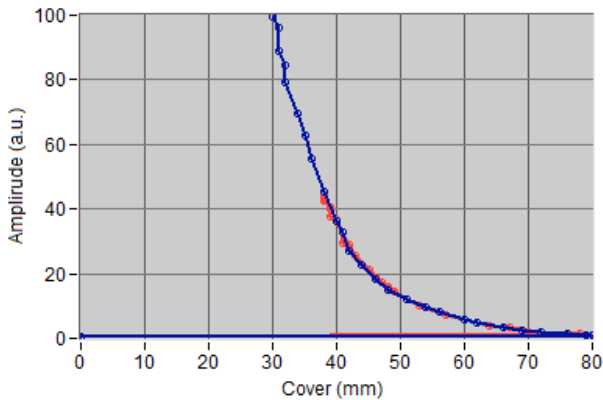


**Figure 46: Relation between signal amplitude and concrete cover for a #4 rebar diameter.
 Blue curve: parallel polarization of the probe
 Red curve: perpendicular polarization of the probe**

In the same way as it was done in Figure 44 for a concrete cover of 1", Figure 47 gives the measured concrete cover in relation to the scan position for a concrete cover of 50 mm (2.0"). The blue curve shows the measurements taken in parallel polarization; the red curve describes the ones taken in perpendicular polarization. In accordance with Figure 44, it can be seen that the blue curve starts at a value of 60 mm (2.4") and rises up to a value of about 80 mm (3.2"), while the red curve starts at about 77 mm (3.08") and lies above the blue curve. Increasing the concrete cover by a factor of two increased the measured values in the same way, which naturally is expected. The amplitudes of the signal (Figure 48), however, dropped by a significantly higher factor, thus confirming the relation between signal strength and concrete cover described in Figure 46.

Based on this calibration experiment:

- The effect of the adjacent (parallel or crossing) rebars on the measurement at a particular rebar location can be estimated.
- The difference in signal amplitude between probe polarization (parallel as well as perpendicular) to the rebar becomes clear.
- The relation between signal strength and distance to the rebar (concrete cover) becomes clear.
- The device specific characteristic of setting any value of measured concrete cover higher than 80 mm (3.2") to zero becomes clear.

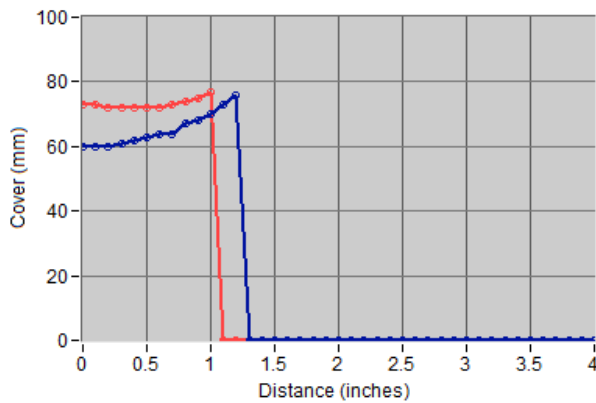


**Figure 47: Concrete cover calibration curve at a rebar with a 50 mm (2'') cover.
Blue curve: parallel polarization of the probe
Red curve: perpendicular polarization of the probe**

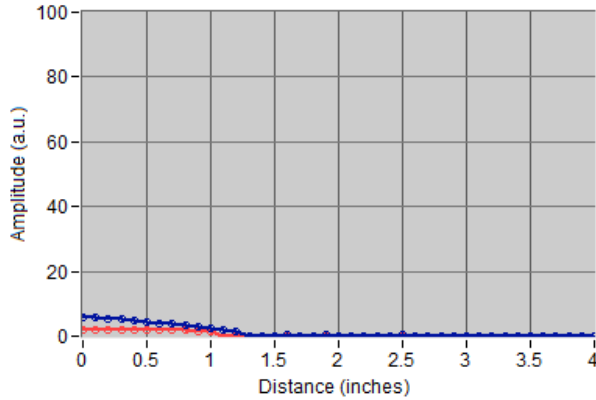


Figure 48: Signal amplitude calibration curve at a rebar with a 50 mm (2'') cover.
Blue curve: parallel polarization of the probe
Red curve: perpendicular polarization of the probe

5.2.3 Calibration Experiment No. 3, Rebar Size

In this experiment the influence of the rebar diameter on the signal amplitude is investigated. Therefore, a setup as shown in Figure 49 was used, where the distance between the probe and a rebar stays constant and only the rebar diameter is changed.

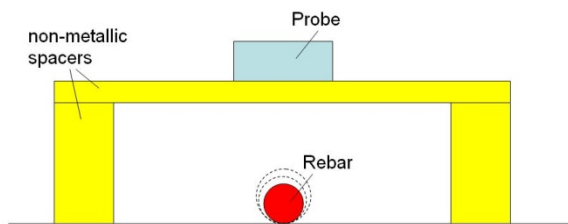


Figure 49: Experimental setup for investigation of the influence of the rebar diameter on the signal amplitude.

The rebar diameter was varied over a range from 13 mm (0.52'') to 50 mm (2.0'') and the following data given in Table 8 was obtained.

Table 8: Measured cover and amplitude depending on the bar size.

Rebar Size Setting on the Device (mm)	Metric Bar Size (mm)	In-Lb Bar Size	Cover (mm) (actual distance between probe and rebar)	Measured Cover (mm)	Signal Amplitude (a.u.)
13	13	#4	26.1	29	102.3
19	19	#6	26.1	29	148.1
29	29	#9	26.1	29	181.6
50	57	#18	26.1	29	236.0

In all cases a cover of 29 mm (1.16”) was measured. Subtracting the pad offset of 2 mm (0.08”) gives a cover of 27 mm (1.08”). The actual cover was determined to be 26.1 mm (1.044”). This means a difference of less than 1 mm (0.04”), which as well might be caused by some slight inaccuracies in the caliper measurement to determine the position of the probe. The signal amplitudes vary with the rebar diameter. This is shown in the graphs in Figure 50, where the amplitude is plotted as a function of the rebar diameter (Figure 50, left) and as a function of the cross sectional area of the rebar (Figure 50, right). It can be seen that the curves become more linear the larger the size becomes. In any case, the size of the rebar diameter has to be known for the depth measurement to be accurate. Especially for diameters in the lower range, an error in the rebar size will have a significant effect.

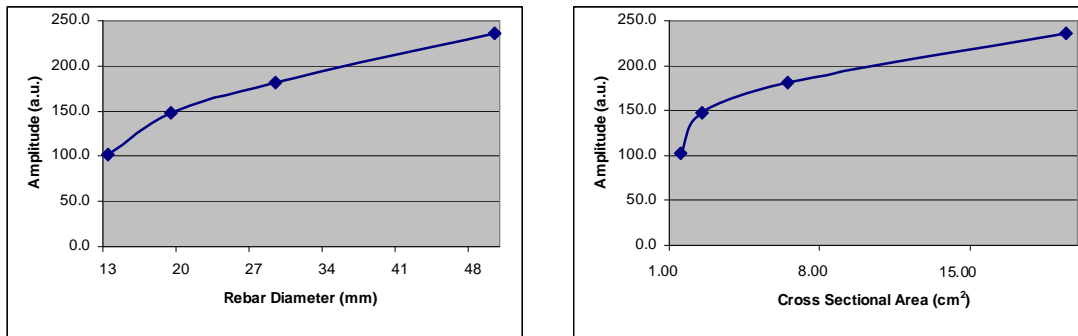


Figure 50: Signal amplitude in relation to the cross sectional area of the rebar, revealing a linear relation.

From this experiment, it can be seen that:

- The covermeter provides good accuracy (at least in this case where a single rebar was measured) as long as the rebar diameter entered in the settings matches the actual size of the rebar.
- Increasing the rebar diameter will increase the amplitude of the signal; this effect is higher for smaller rebar diameters than for larger diameters.

5.2.4 Calibration Experiment No. 4, Rebar Spacing

This experiment serves to verify the findings of experiment 2 (rebar scan). Two rebars of the same size (13 mm, #4) were placed right next to each other. The rebar diameter was entered in the settings menu of the device. The probe was positioned exactly over the center of the first rebar at a distance (cover) of 52 mm (2.08”). The second rebar was moved step by step away from the first rebar while the probe as well as the first rebar was not moved. For every position of the second rebar the signal amplitude and the resulting concrete cover were measured. The following readings are listed in Table 9.

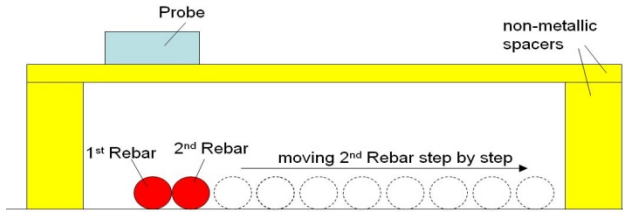


Figure 51: Investigating the effect of an adjacent rebar and the spacing between the two rebars.

Table 9: Measured cover and amplitude depending on the bar spacing.

Bar Spacing (mm)	Measured Cover (mm)	Measured Amplitude (a.u.)
0	49	11.6
5	49	11.7
10	50	10.8
15	50	10.8
20	51	10.4
25	51	9.7
30	52	9.3
35	52	9.2
40	53	8.5
45	53	8.4
50	53	8.1
55	53	8.1
60 to ∞	54	7.9

Figure 52 displays the data as measured cover over bar spacing (left curve) as well as signal amplitude over bar spacing (right curve). The 2 mm (0.08”) pad offset has to be subtracted from the data. Taking into account this offset, the true value for the concrete cover is obtained when the spacing between the two rebars is more than 60 mm (2.4”). If the rebars are located right next to each other, i.e., bars spacing = 0, a cover of (49 - 2) mm = 47 mm (1.88”) is measured. That means the concrete cover is measured 5 mm (0.2”) too low for an actual rebar depth of 52 mm (2.08”). In that case the amplitude measures 11.6 instead of the value of 7.9, which is determined when there is just one rebar. This is consistent with the data shown in Figure 48 (blue curve).

On the other hand it means that not taking into account the adjacent rebars within a rebar layer at a depth of 52 mm (2.08”) and #4 rebars will affect the measurement by no more than 5 mm (0.2”) as long as there is no further reinforcement in other layers close to the rebar on which the measurement is being conducted.

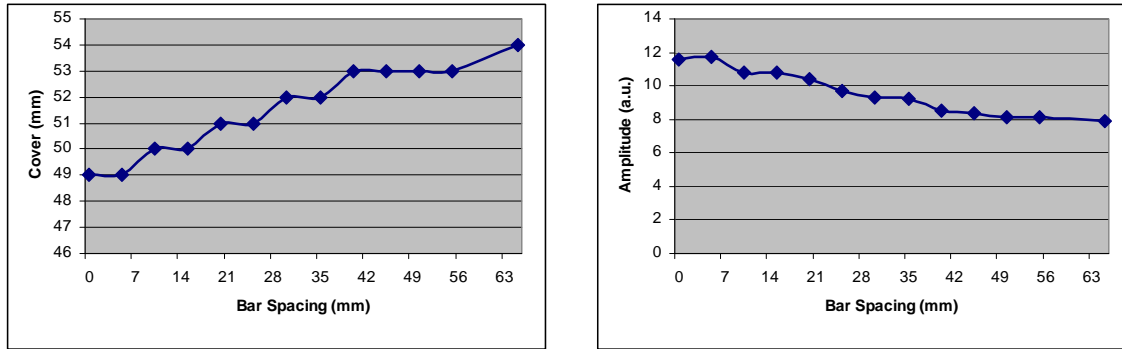


Figure 52: Cover readings (left) as well as signal amplitudes (right) in relation to the bar spacing. The pad offset of 2 mm (0.08”) has to be subtracted from the measured cover in the curve.

In summary, this experiment shows that:

- Adjacent rebars affect the measurement; the measured cover will be lower than the actual cover because of increased signal amplitude.
- For #4 rebars at a depth of approximately 50 mm (2.0”), the measurement will hardly be affected if the rebar spacing is more than 40 mm (1.6”), and will not be affected at all if the rebar spacing is more than 60 mm (2.4”).
- For #4 rebars at a depth of approximately 50 mm (2.0”), the effect of adjacent rebars will not change the measurement by more than 5 mm (0.2”), assuming that there is no further reinforcement in further layers.
- The findings from Experiment No. 2 are further confirmed.

5.2.5 Conclusion from the Experiments

The experiments served to understand the functionality of the covermeter being used. A pad offset of 2 mm (0.08”) was found and has to be taken into account in the measurements. The relation between measured signal amplitude and the rebar depth, diameter, and adjacent rebar parallel as well as perpendicular to the respective rebar were investigated. These findings will be taken into account in the analysis of the measurements described in the following chapters.

The findings are mostly consistent with the information on the accuracy that can be found in the manual [1] of the device and depicted in Figure 53. For example, a #4 rebar with a diameter of 13 mm (0.52”) at a depth of 50 mm (2.0”) would require a minimum spacing of about 56 mm (2.24”) according to the diagram to be resolved, which is about the value that was determined in the experiments described above for the measurement not to be affected by adjacent rebars.

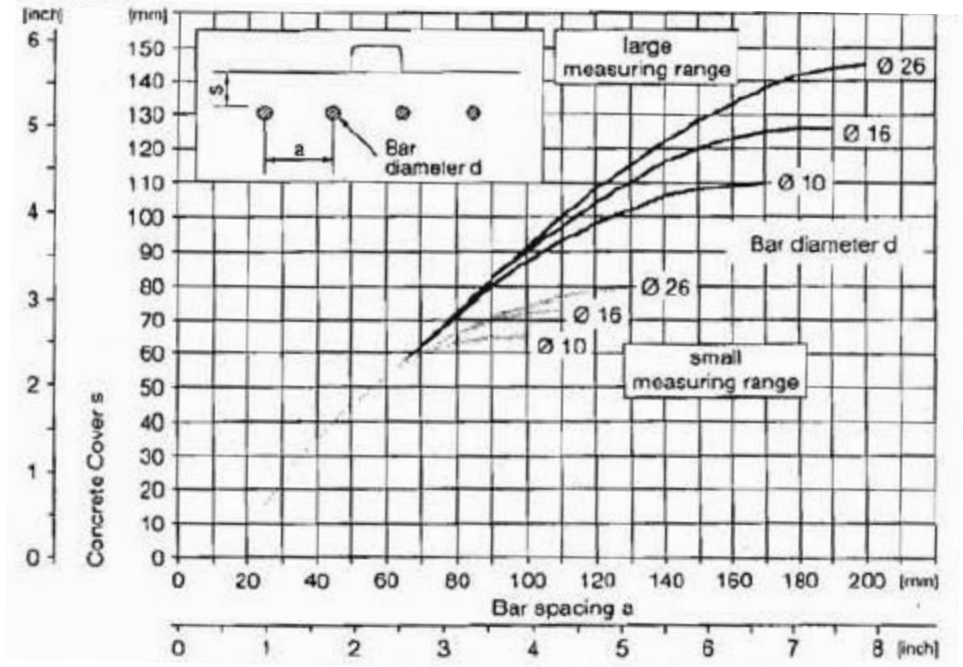


Figure 53: Diagram describing the resolution of the covermeter. Provided by the manufacturer [1].

5.3 Specimen 1, Steel Reinforcement



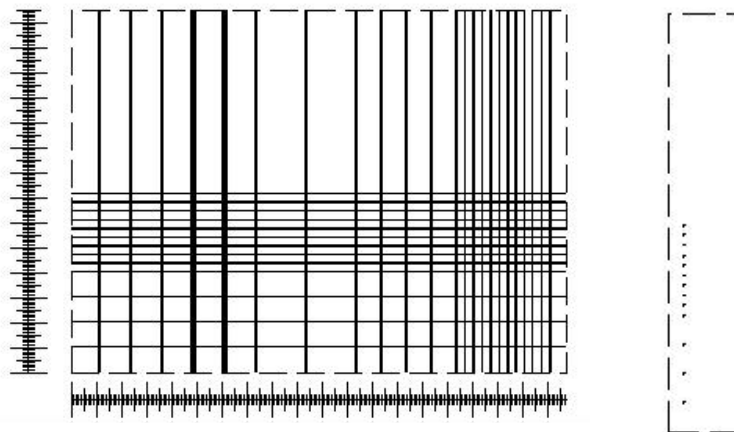
Figure 54: Block with steel reinforcement in the test frame during measurement.

Covermeter measurements as well as complementary ultrasonic-echo measurements were conducted on this block (Figure 54) and will be described in the following.

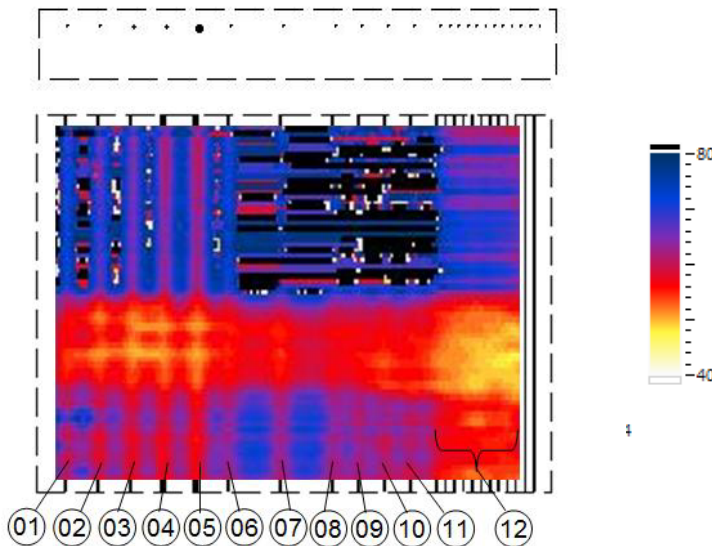
5.3.1 Covermeter Measurements

Covermeter measurements were conducted from both sides of the block, in x- as well as in y-direction to resolve reinforcement in both orientations, so that altogether four data sets were obtained. The measurements were conducted along scan lines. To ensure that the positioning of the probe at the measurement position is exact, the probe was not continuously dragged along the surface but moved point by point. Since it was mounted on the cart, it did not have to be lifted up and was moved directly to the next measurement position. The distance between two consecutive measurement positions was 2 mm (0.08”), the distance between two consecutive scan lines was 20 mm (0.8”). Figure 55 shows the results obtained from the scans on the front of the block while similar results are shown for the back of the block in Figure 56. All rebar indications that are related to a rebar are numbered.

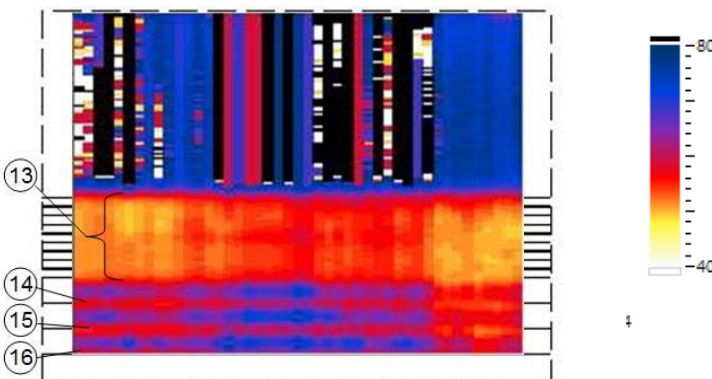
Figure 57a-e allocates the indications to the actual rebar positions in the block according to Table 22 and Table 3, and shows the measured cover over the respective block length in x- or y-direction at the position of the indication. The details are revealed by the curves. The solid blue curve gives the measured data, the dotted red line indicates the actual concrete cover of the respective rebar in the block.



a) Steel reinforcement layers on the front of the block.

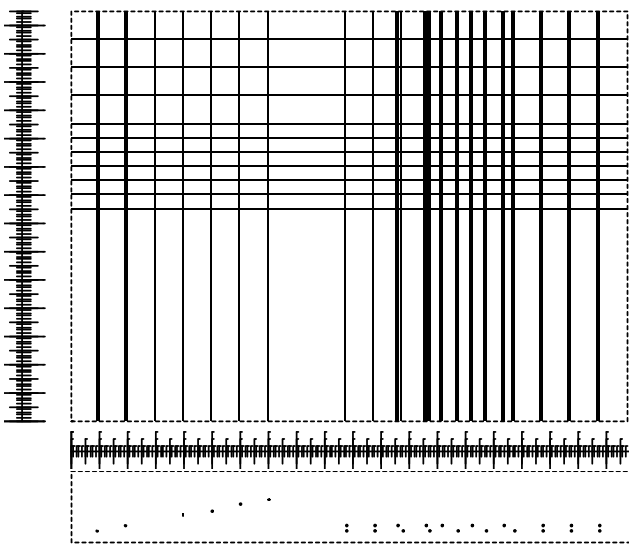


b) Measured covers, scans in horizontal (x-) direction to detect rebars running in y-direction. Besides the response from the rebars in y-direction, there is also a weaker and unintended response measured from the reinforcement running in x-direction.

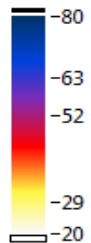
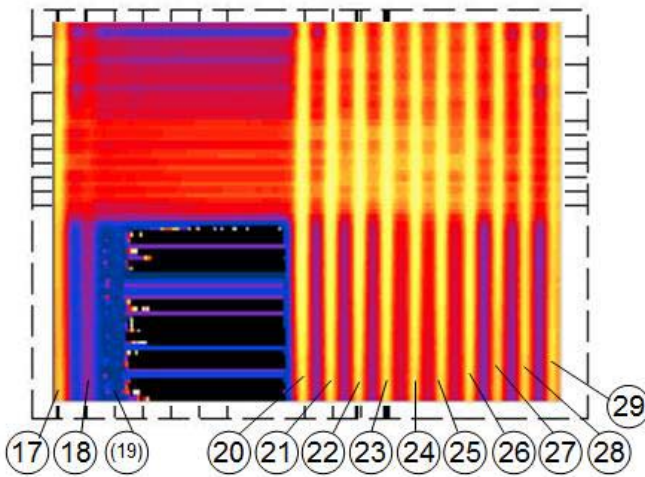


c) Measured covers, scans in vertical (y-) direction to detect rebars running in x-direction. Besides the response from the rebars in x-direction, there is also a lower and unintended response being measured from the reinforcement running in y-direction.

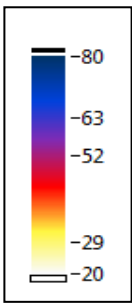
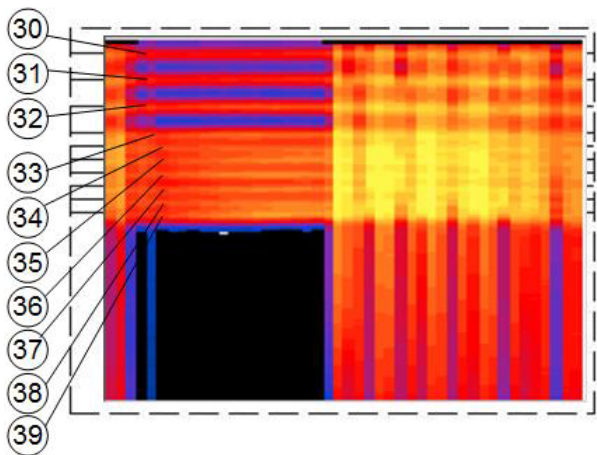
Figure 55: Results obtained from the front of the block.



a) Steel reinforcement layers on the back of the block.



b) Measured covers, scans in horizontal (x-) direction to detect rebars running in y-direction. Besides the response from the rebars in y-direction, there is also a weaker and unintended response measured from the reinforcement running in x-direction.



c) Measured covers, scans in vertical (y-) direction to detect rebars running in x-direction. Besides the response from the rebars in x-direction, there is also a lower and unintended response being measured from the reinforcement running in y-direction.

Figure 56: Results obtained from the back of the block.

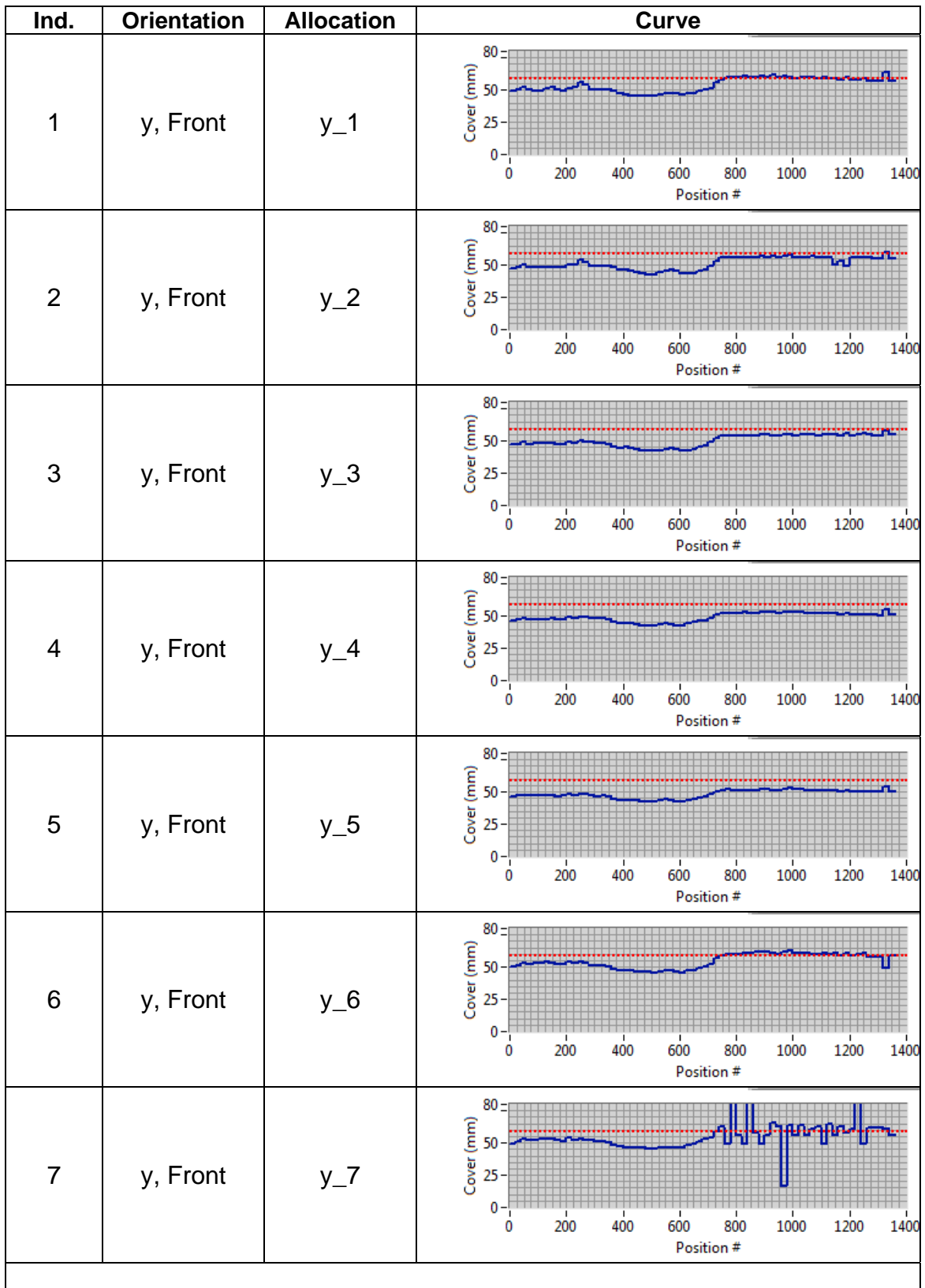


Figure 57a: Evaluation of the rebar indications.

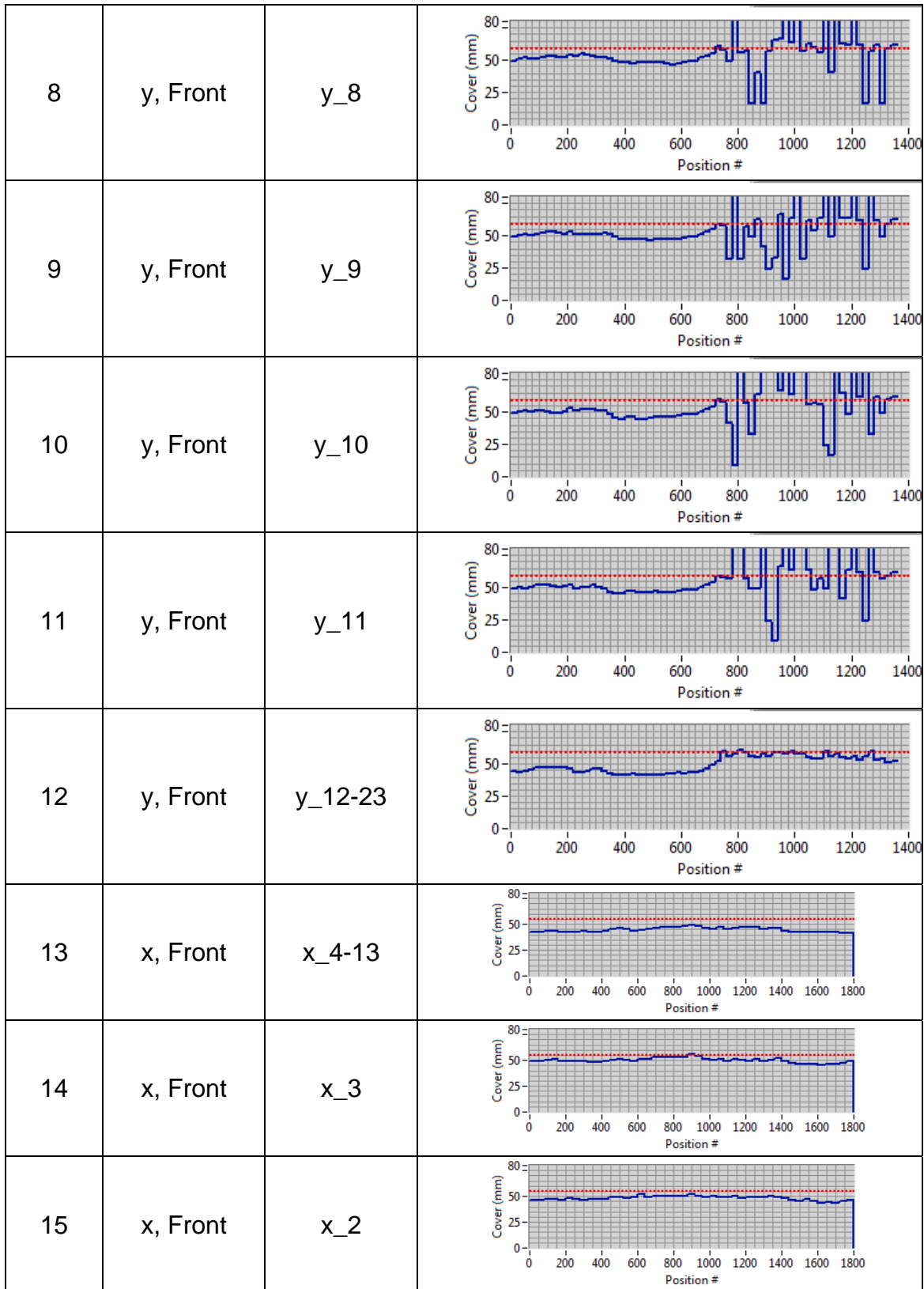


Figure 57b: Evaluation of the rebar indications.

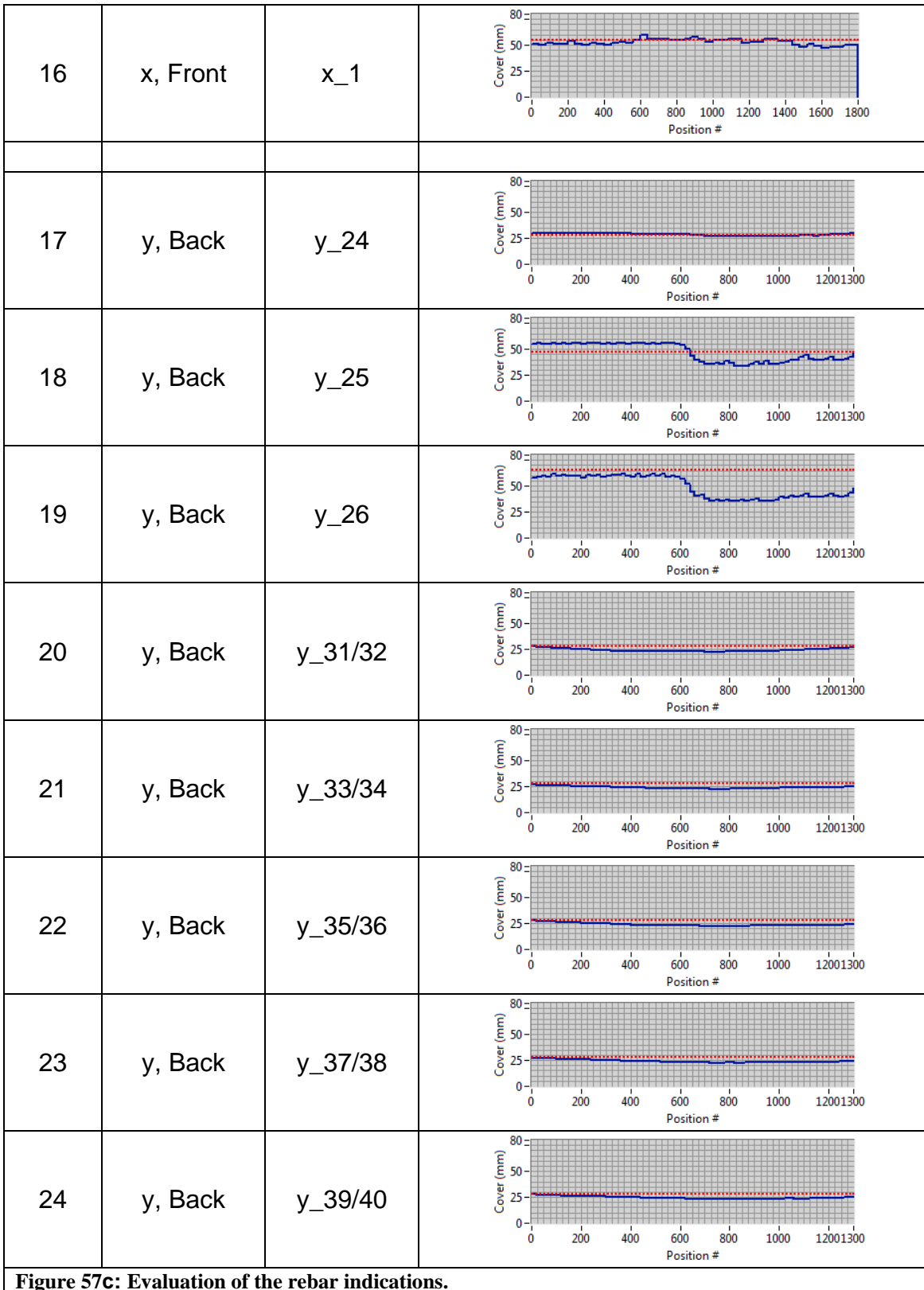
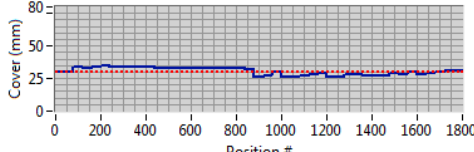
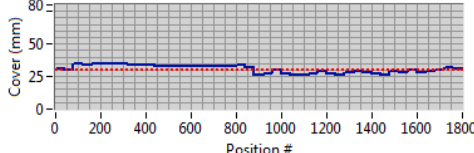
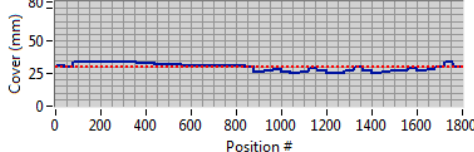
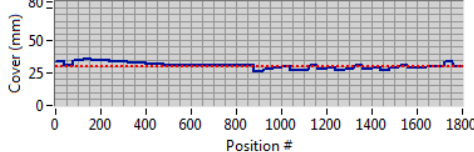


Figure 57c: Evaluation of the rebar indications.

25	y, Back	y_41/42	
26	y, Back	y_43/44	
27	y, Back	y_45/46	
28	y, Back	y_47/48	
29	y, Back	y_49/50	
30	x, Back	x_23	
31	x, Back	x_22	
32	x, Back	x_21	
33	x, Back	x_20	

Figure 57d: Evaluation of the rebar indications.

34	x, Back	x_19	 <p>The graph shows cover depth (mm) vs. Position # (0-1800). The y-axis ranges from 0 to 80 mm. The x-axis ranges from 0 to 1800. A solid blue line represents the measured cover, which fluctuates around a mean value of approximately 30 mm. A horizontal dashed red line is drawn at approximately 30 mm, representing the target cover depth.</p>
35	x, Back	x_18	 <p>The graph shows cover depth (mm) vs. Position # (0-1800). The y-axis ranges from 0 to 80 mm. The x-axis ranges from 0 to 1800. A solid blue line represents the measured cover, which fluctuates around a mean value of approximately 30 mm. A horizontal dashed red line is drawn at approximately 30 mm, representing the target cover depth.</p>
36	x, Back	x_17	 <p>The graph shows cover depth (mm) vs. Position # (0-1800). The y-axis ranges from 0 to 80 mm. The x-axis ranges from 0 to 1800. A solid blue line represents the measured cover, which fluctuates around a mean value of approximately 30 mm. A horizontal dashed red line is drawn at approximately 30 mm, representing the target cover depth.</p>
37	x, Back	x_16	 <p>The graph shows cover depth (mm) vs. Position # (0-1800). The y-axis ranges from 0 to 80 mm. The x-axis ranges from 0 to 1800. A solid blue line represents the measured cover, which fluctuates around a mean value of approximately 30 mm. A horizontal dashed red line is drawn at approximately 30 mm, representing the target cover depth.</p>
38	x, Back	x_15	 <p>The graph shows cover depth (mm) vs. Position # (0-1800). The y-axis ranges from 0 to 80 mm. The x-axis ranges from 0 to 1800. A solid blue line represents the measured cover, which fluctuates around a mean value of approximately 30 mm. A horizontal dashed red line is drawn at approximately 30 mm, representing the target cover depth.</p>
39	x, Back	x_14	 <p>The graph shows cover depth (mm) vs. Position # (0-1800). The y-axis ranges from 0 to 80 mm. The x-axis ranges from 0 to 1800. A solid blue line represents the measured cover, which fluctuates around a mean value of approximately 30 mm. A horizontal dashed red line is drawn at approximately 30 mm, representing the target cover depth.</p>
<p>Figure 57e: Evaluation of the rebar indications.</p>			

5.3.2 Ultrasonic Echo

The objective of the ultrasonic echo measurements was to see how far ultrasound would be able to detect reinforcement in this challenging scenario. To detect the bars, it was assumed that the distance between the points along the scan line would have to be very small. Therefore, it was chosen to be 2 mm (0.08”). Scans were taken in x-as well as in y-direction and measured from the back of the specimen. With a point distance that small, it was hoped to have good conditions (clear hyperbolas obtained from the rebar reflections) for the application of the SAFT algorithm and to be able to focus the rebar reflections to a clear point like reflector.

The distance between the consecutive scan lines was 16 cm (6.4”) for both scan directions. Figure 58 shows the B-scans obtained from scans in vertical (y-) direction, thus crossing the rebars running in x-direction. Depicted are the B-scans obtained from the original HF-signal as well as the B-Scans of the HF-signal after the application of the SAFT algorithm. Especially in the SAFT B-scans it becomes obvious that the reflections of the reinforcement steel can indeed be seen. Also, reinforcement close to the backwall can be detected, and, in the area with very dense reinforcement, the bars close to the surface can be located.

Figure 59 shows the B-scans obtained from scans in horizontal (x-) direction, thus crossing the reinforcement running in y-direction. Almost all the reinforcement bars are detected. In the rebar layer closer to the backwall the bars can be resolved, while at the same time the bars from the first layer with increasing depth are clearly detected as well.

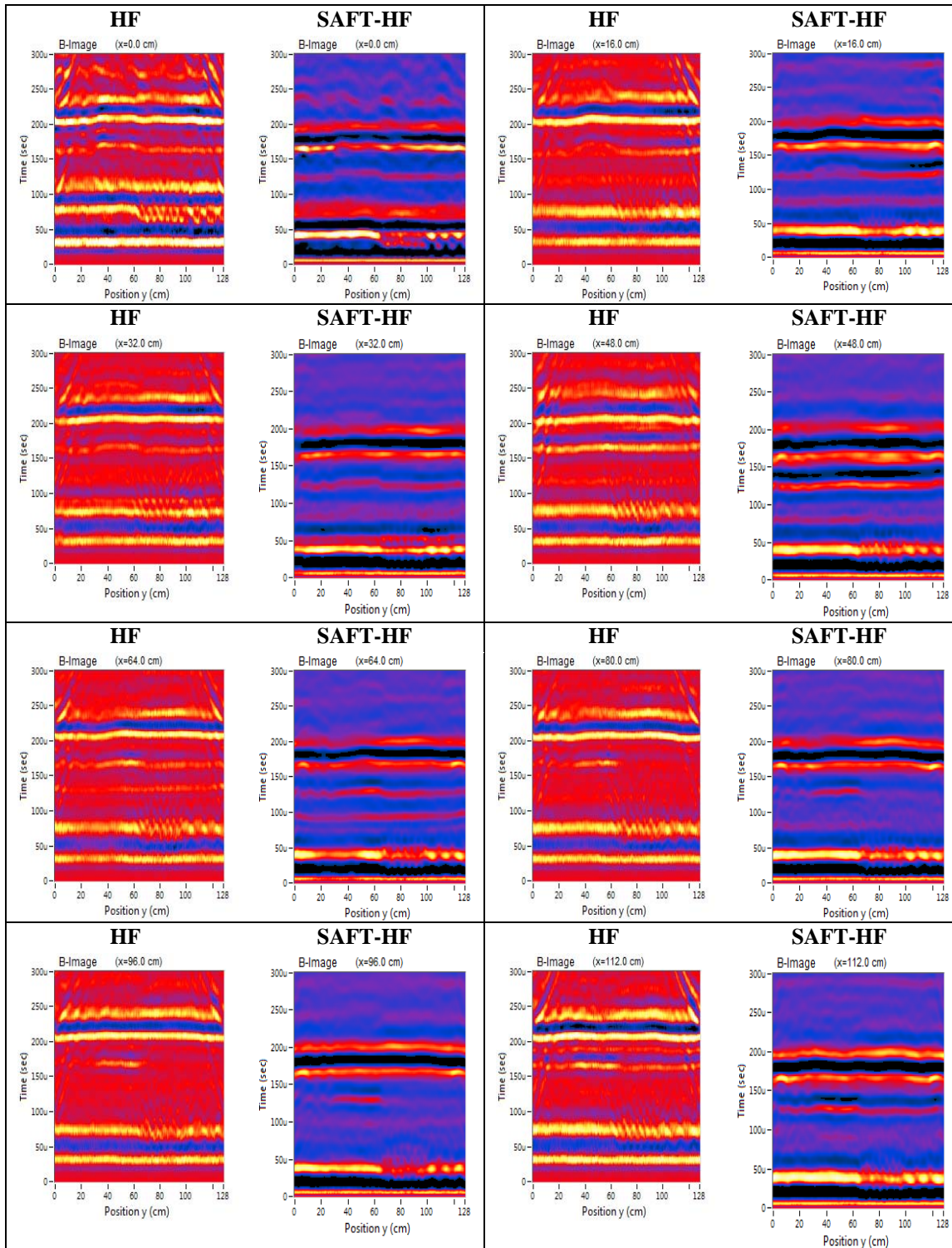


Figure 58a: B-scans at lines $x = 0$ cm to $x = 112$ cm, obtained from vertical scans (y -directions) with and without the application of the SAFT algorithm. With and without SAFT, the rebars running in x -direction can be detected in the B-scan. The application of SAFT makes them appear even clearer.

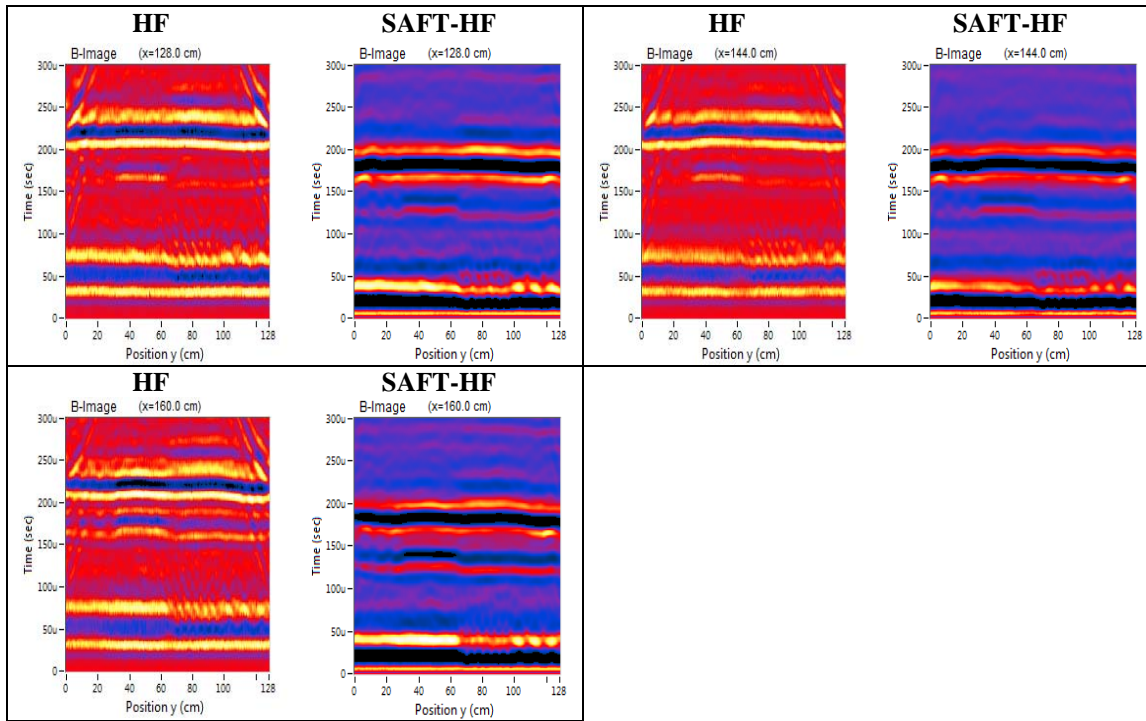


Figure 58b: B-scans at lines $x = 128$ cm to $x = 160$ cm, obtained from vertical scans (y -directions) with and without the application of the SAFT algorithm. With and without SAFT, the rebars running in x -direction can be detected in the B-scan. The application of SAFT makes them appear even clearer.

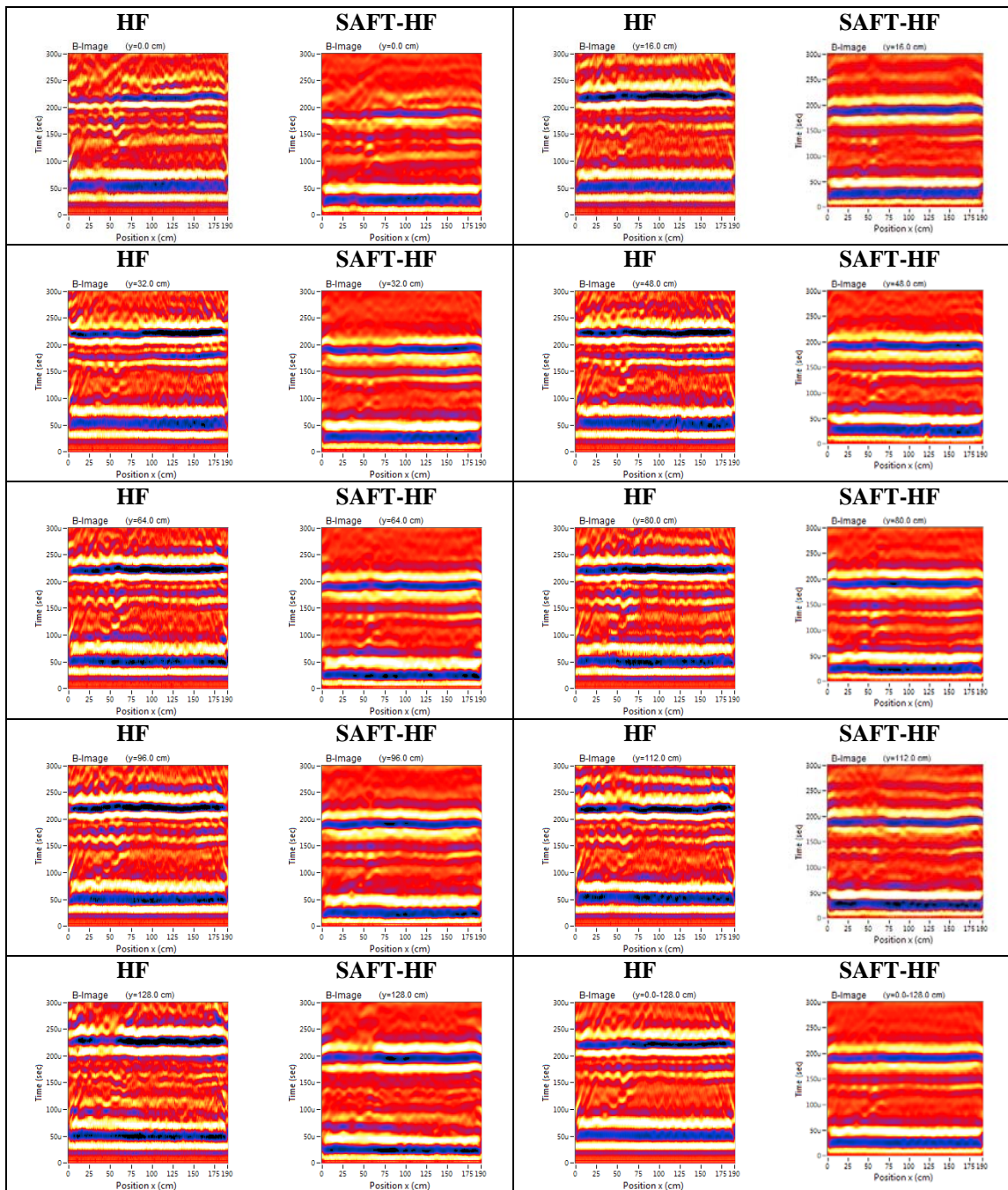


Figure 59: B-scans at lines $x = 0$ cm to $x = 128$ cm, obtained from horizontal scans (x-directions) with and without the application of the SAFT algorithm. With and without SAFT, the rebars running in y-direction can be detected in the B-scan. The application of SAFT makes them appear even clearer.

5.4 Block with Varying Thicknesses

The measurements carried out on the block with varying thicknesses (Figure 60) served to evaluate the capabilities of the different methods in measuring the thickness of a structural member, where the thickness varies over the measurement area, and in detecting minor thicknesses or voids near the backwall. Ultrasonic-echo as well as impact-echo were used. All measurements were carried out from the top (flat side) of the block. In both cases a grid of 20 mm \times 20 mm (0.8" \times 0.8") was used.

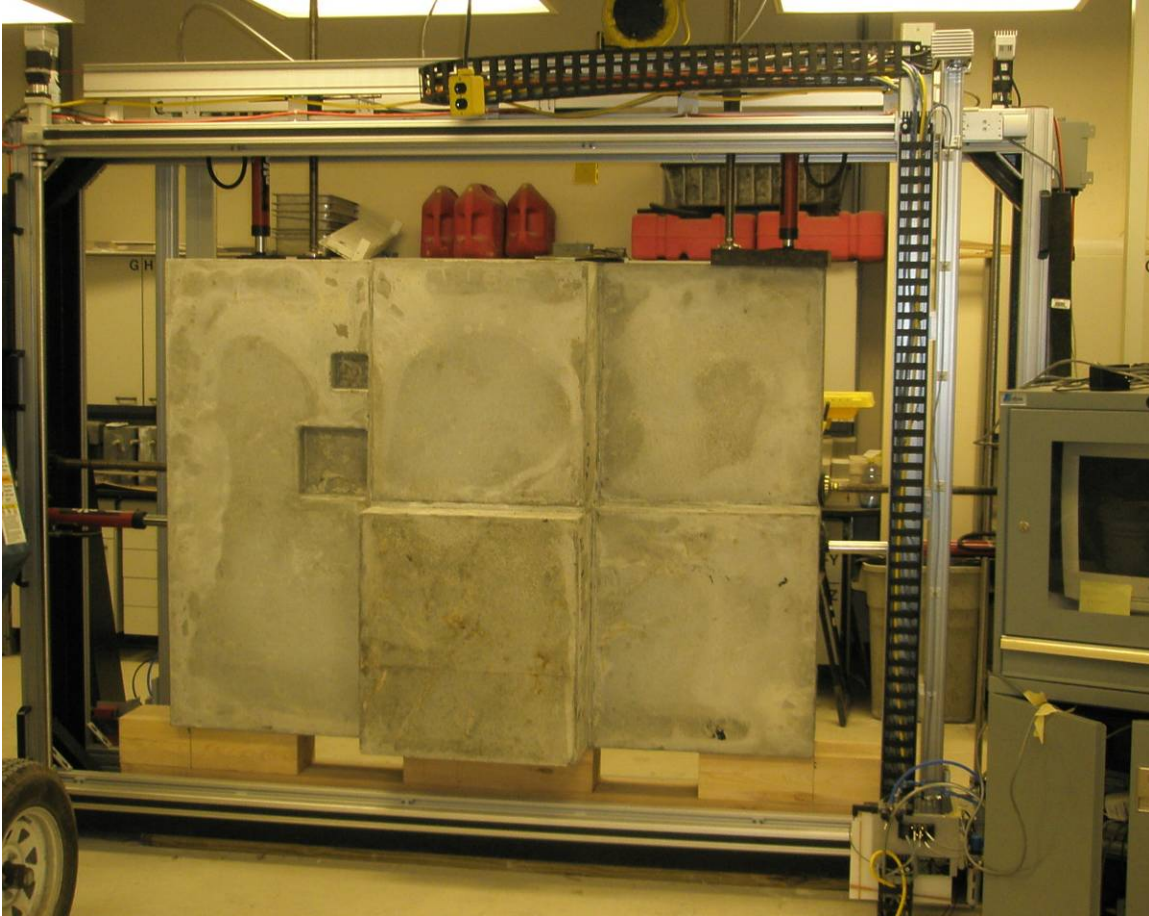


Figure 60: Block with varying thicknesses in the scanning system. Looking at the back of the block, measurements were taken from the other side.

5.4.1 Ultrasonic Echo Measurements

The results obtained from the ultrasonic-echo measurements on a 20 mm \times 20 mm (0.8" \times 0.8") grid are shown as B-scans in Figure 61. In the B-scans, the HF signals, i.e., the entire waveform versus just the absolute values or an envelope of the waveform are given. To evaluate what effect the application of the SAFT has on the results, the B-scans are given with and without the application of the algorithm.

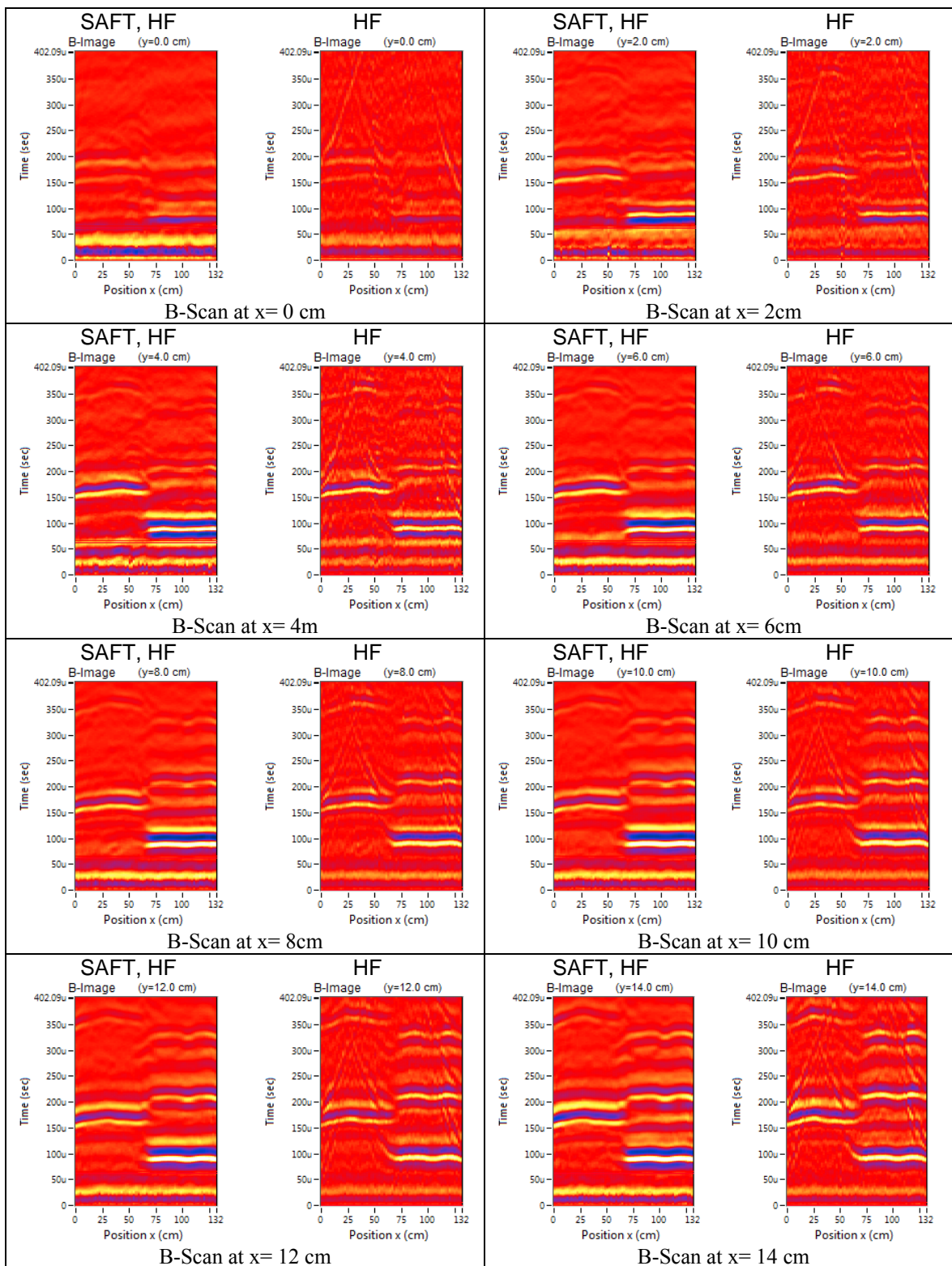


Figure 61a: B-Scans lines 0- 7.

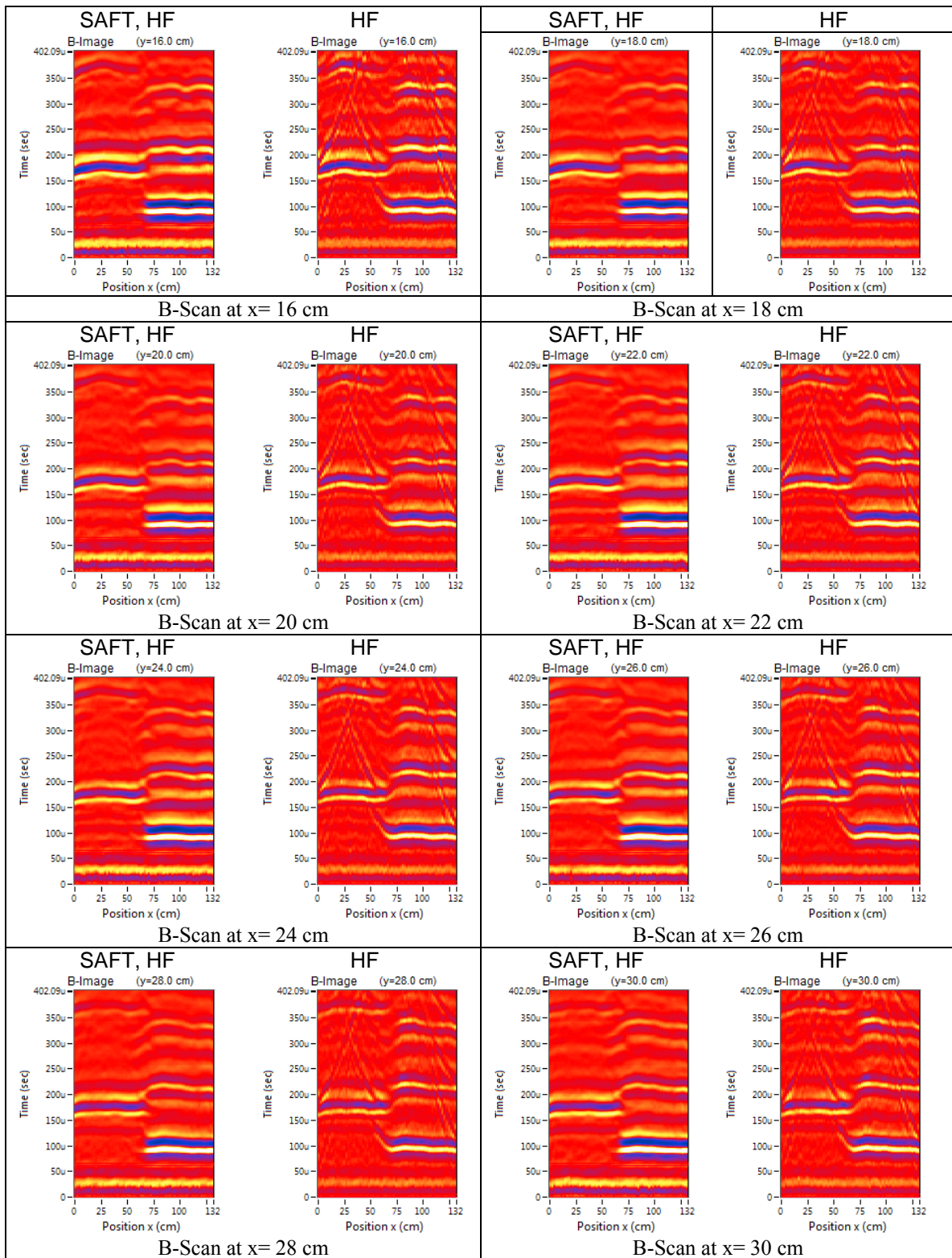


Figure 61b: B-Scans lines 8 – 15.

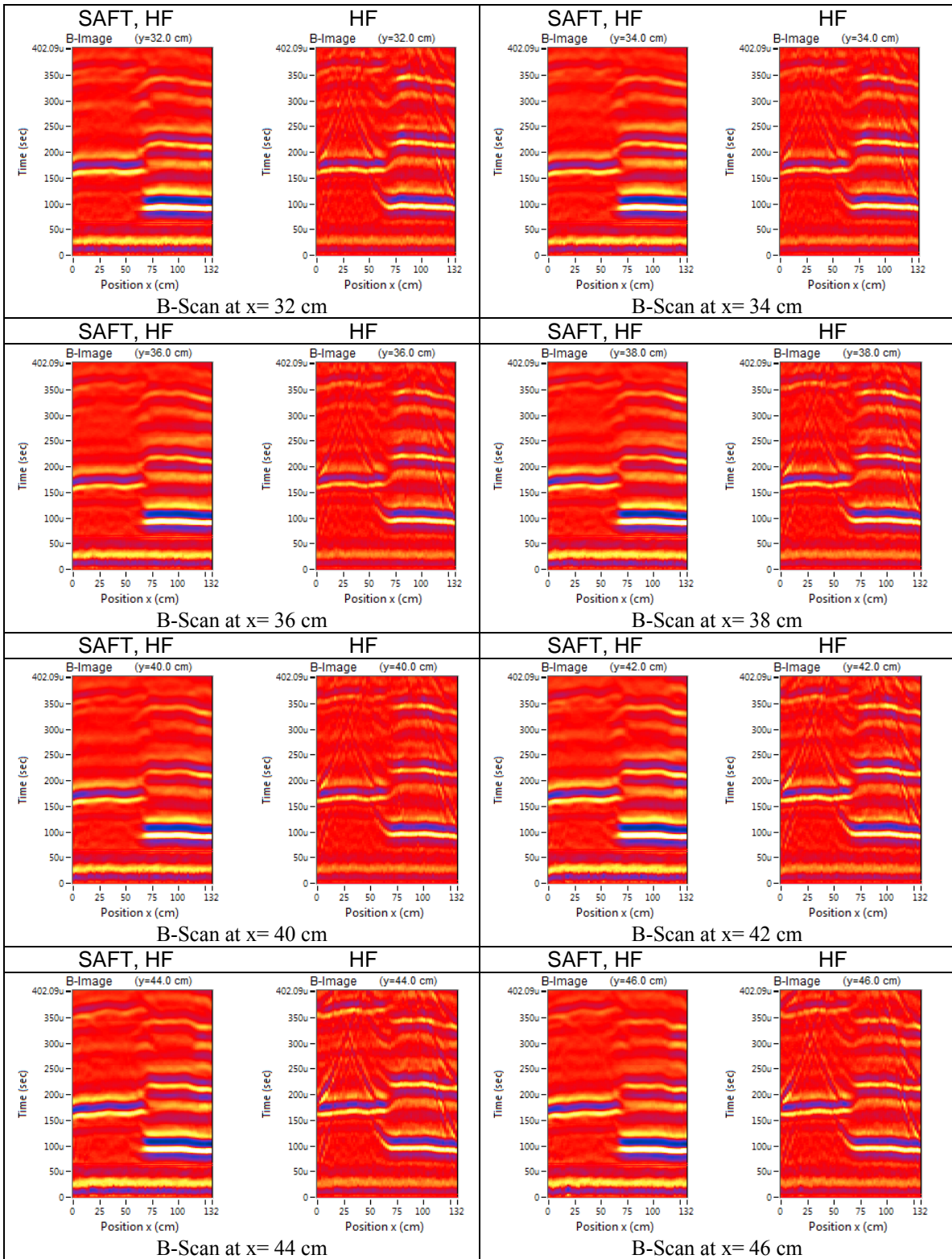


Figure 61c: B-Scans lines 16 – 23.

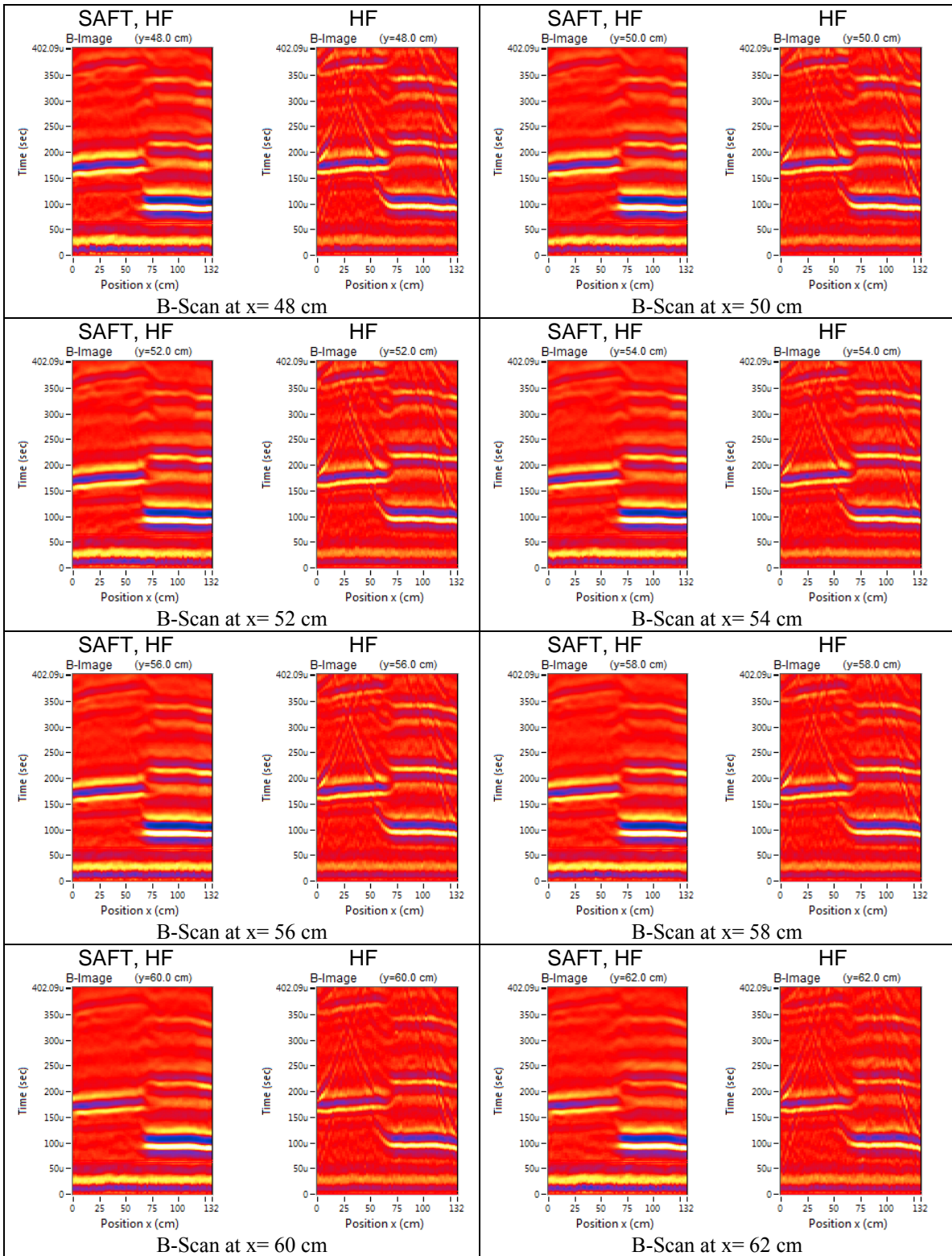


Figure 61d: B-Scans lines 24 – 31.

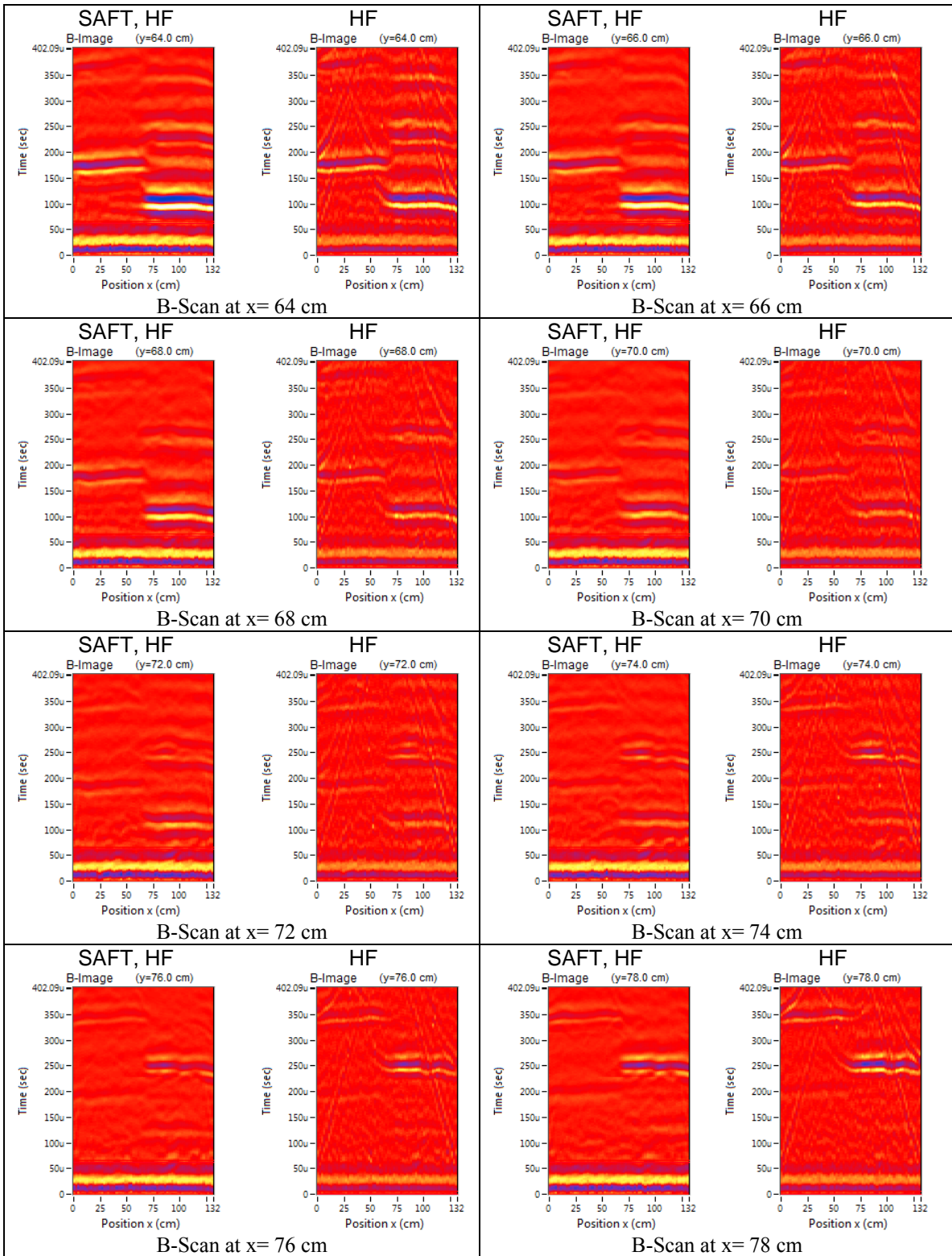


Figure 61e: B-Scans lines 32 – 39.

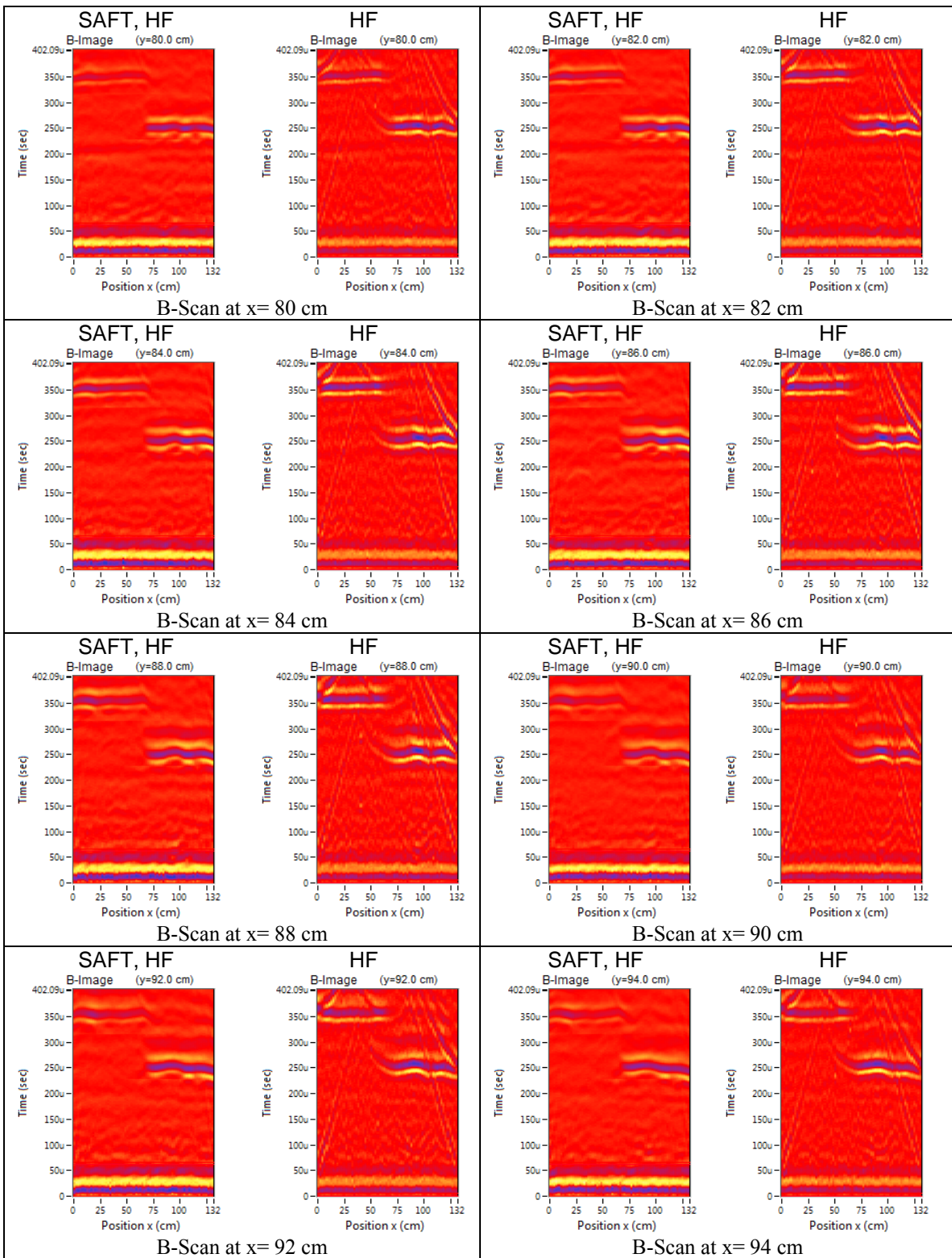


Figure 61f: B-Scans lines 40 – 47.

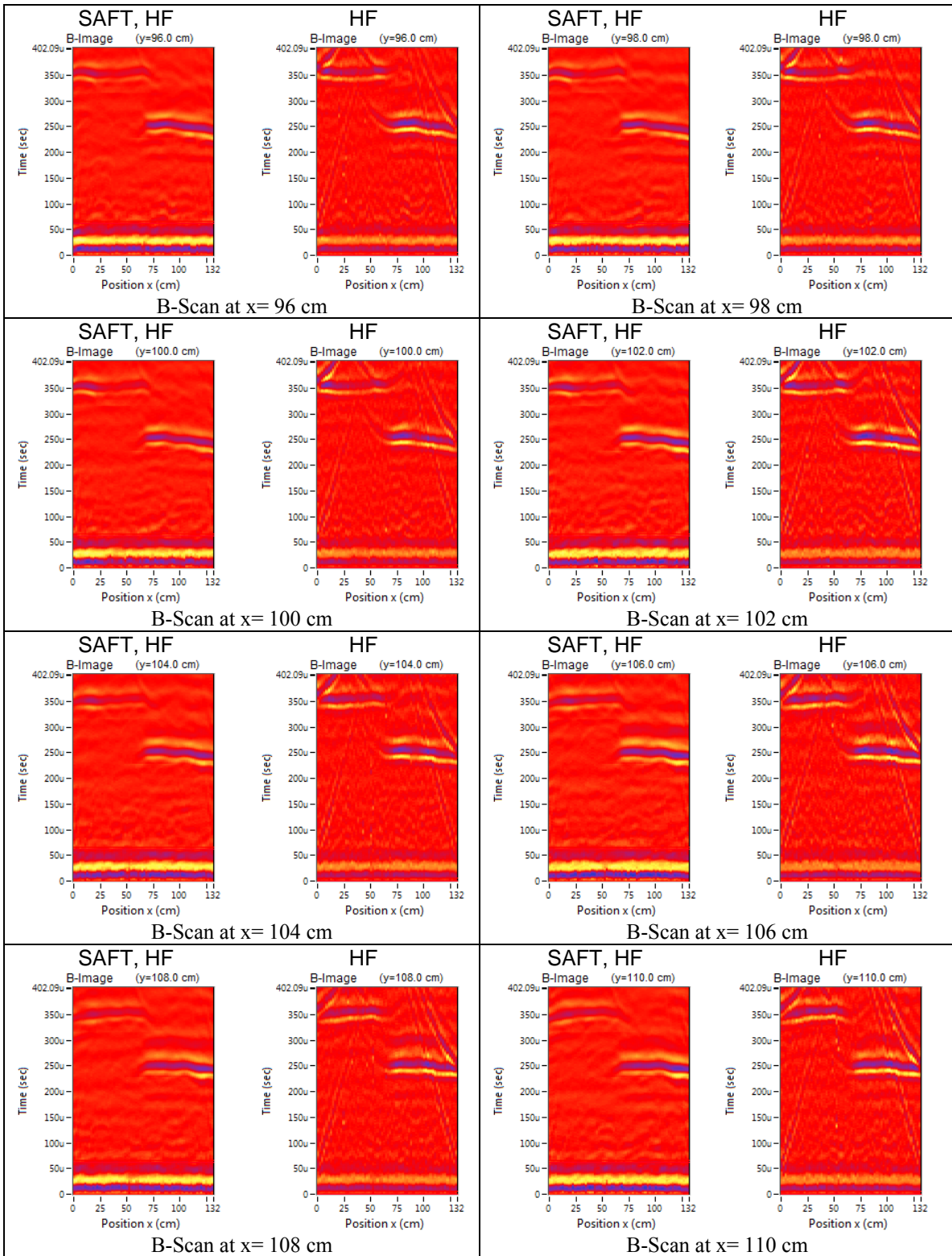


Figure 61g: B-Scans lines 48 – 55.

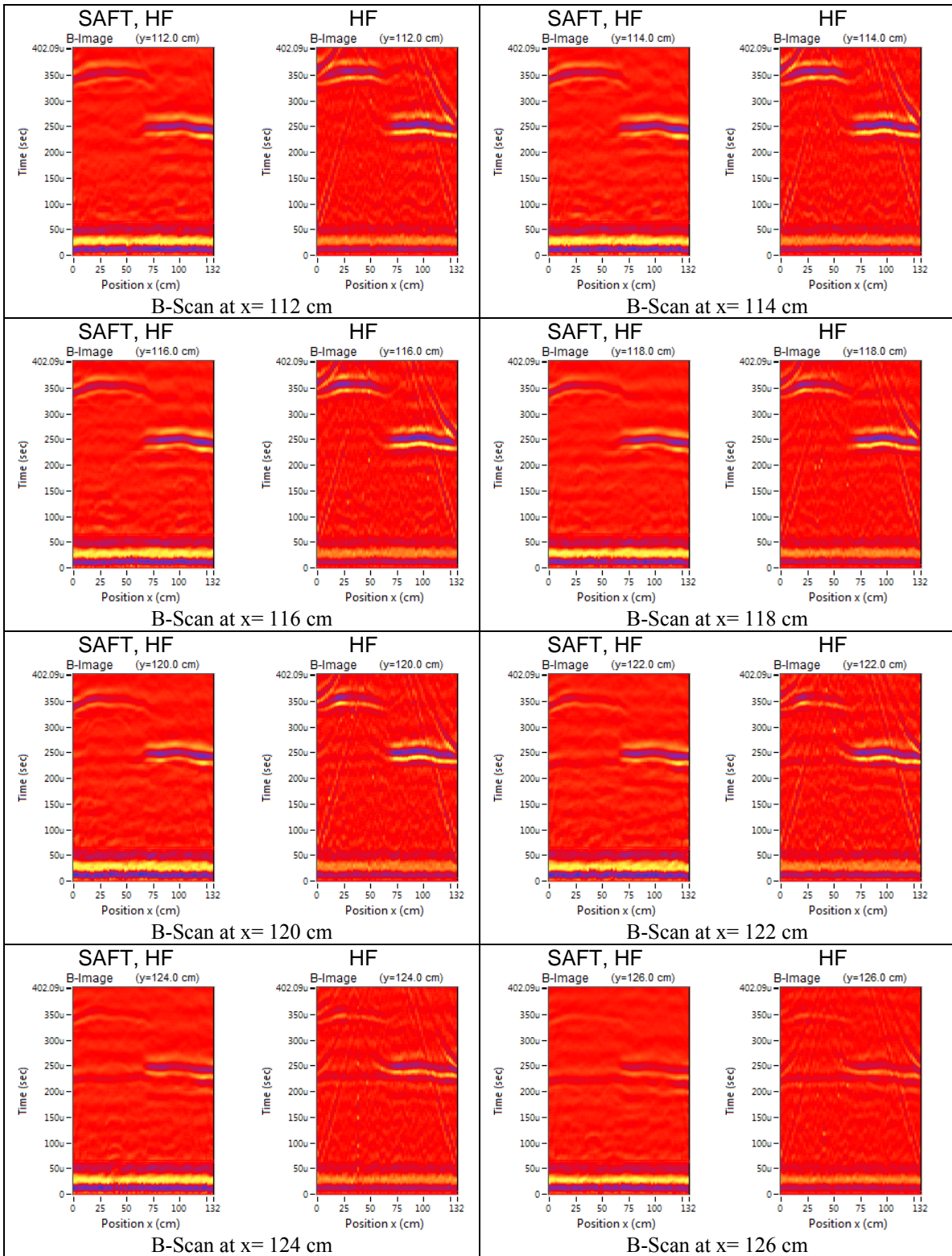


Figure 61h: B-Scans lines 56 – 63.

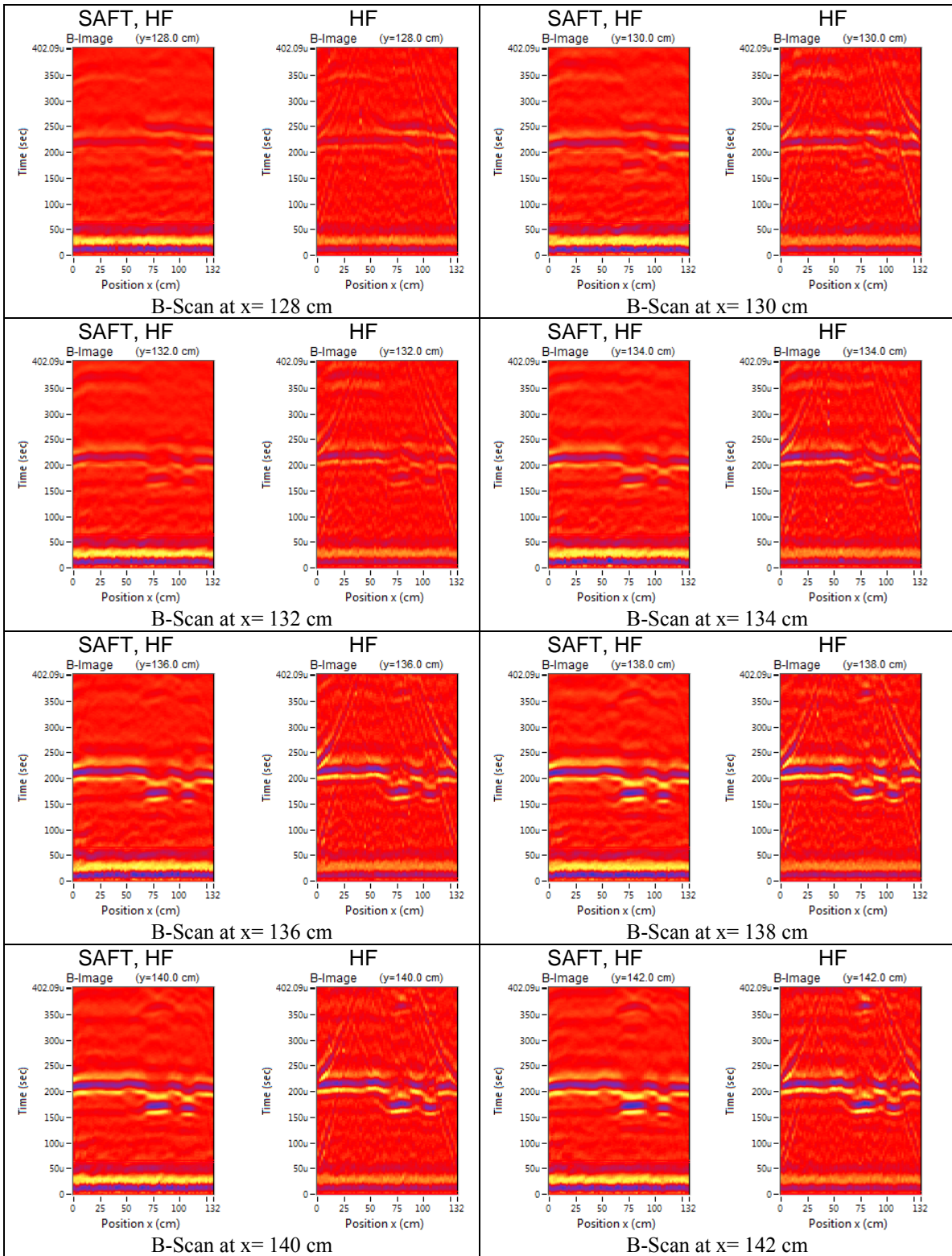


Figure 61i: B-Scans lines 64 – 71.

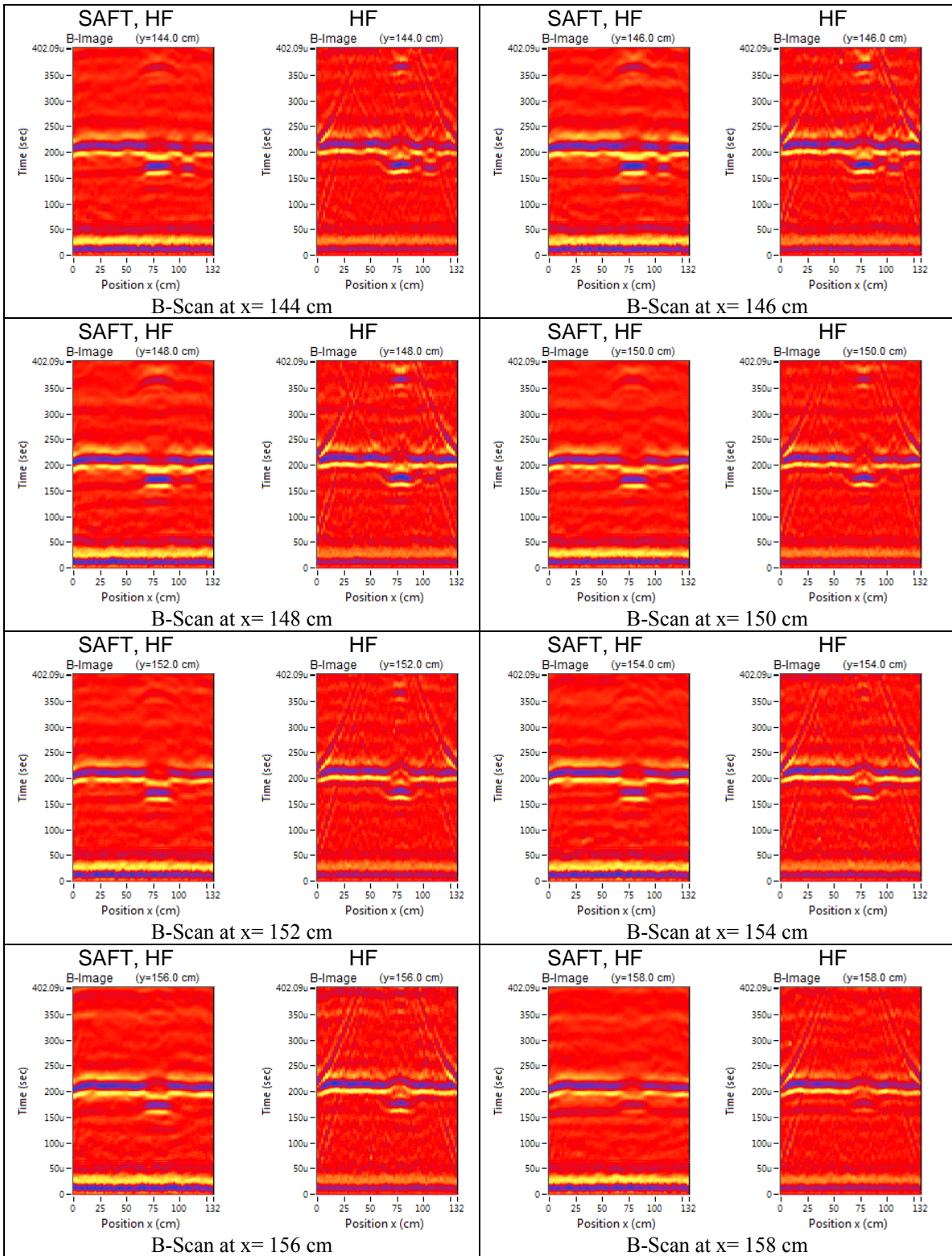


Figure 61j: B-Scans lines 72 – 79.

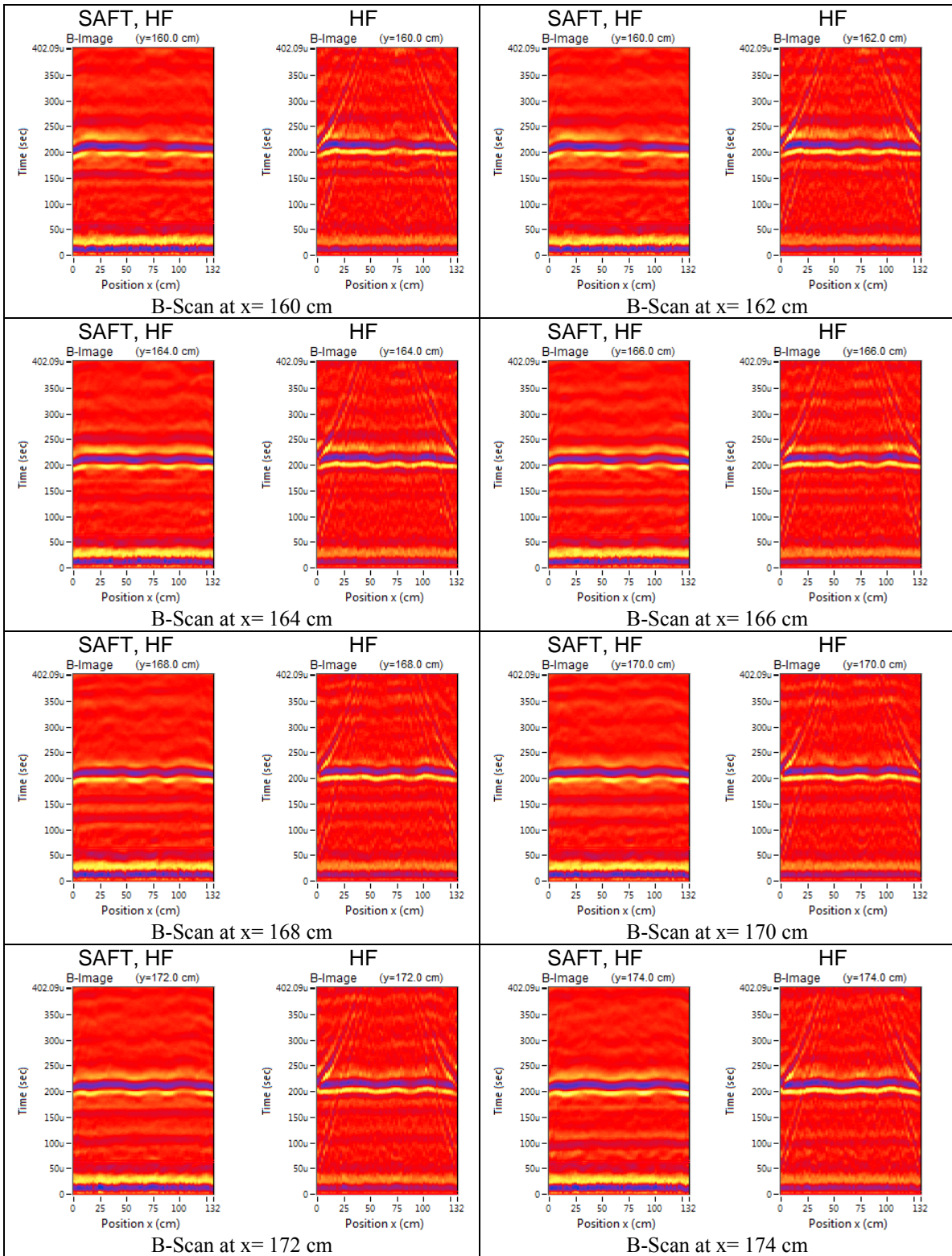


Figure 61k: B-Scans lines 80 – 87.

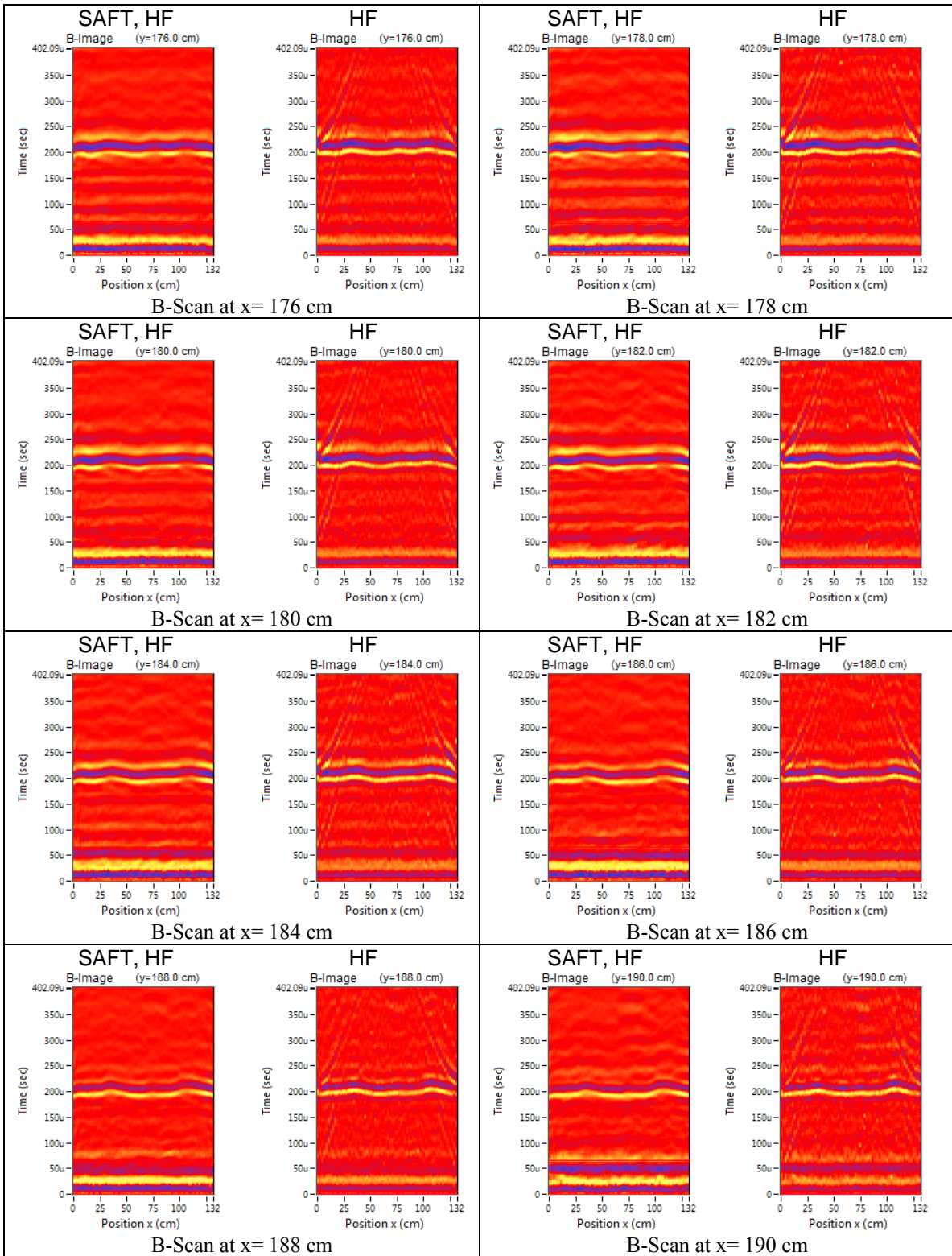


Figure 611: B-Scans lines 88 – 95.

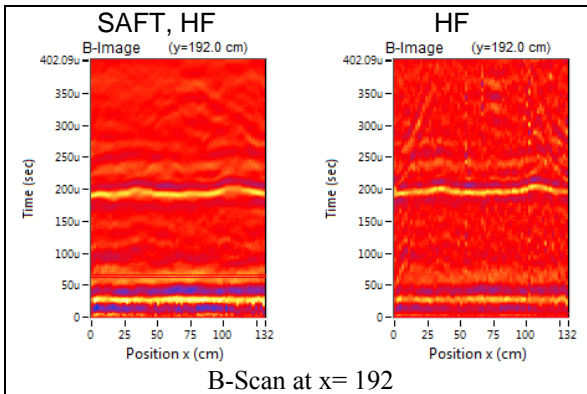


Figure 61m: B-Scan at line 96

A first analysis shows that the backwall reflections are clearly visible for all areas. Using the first and second arrival of the backwall reflection, the shear wave velocity has been determined to an average value of 3056 m/s. This value will be used to determine the depth of a reflector from the measured time of flight. Furthermore, the delay before the actual start of the signal will be subtracted. As the delay is device specific, it is independent from the measured area. As the whole block with all its areas was built out of the same mix (two mixes with same recipe made at the same time and spread equally over the whole block), a significant change in wave velocity is unlikely.

Figure 62 shows the thicknesses obtained as a 3D thickness plot, with and without the application of the SAFT algorithm. In both cases, all six areas with different thicknesses as well as the areas with minor thickness are clearly detected. However, without SAFT, it can be seen that some misleading effects occur at the edges of the areas with different thicknesses. These effects are significantly lower when SAFT is used. Therefore, only the results obtained with SAFT are used for the evaluation in the following.

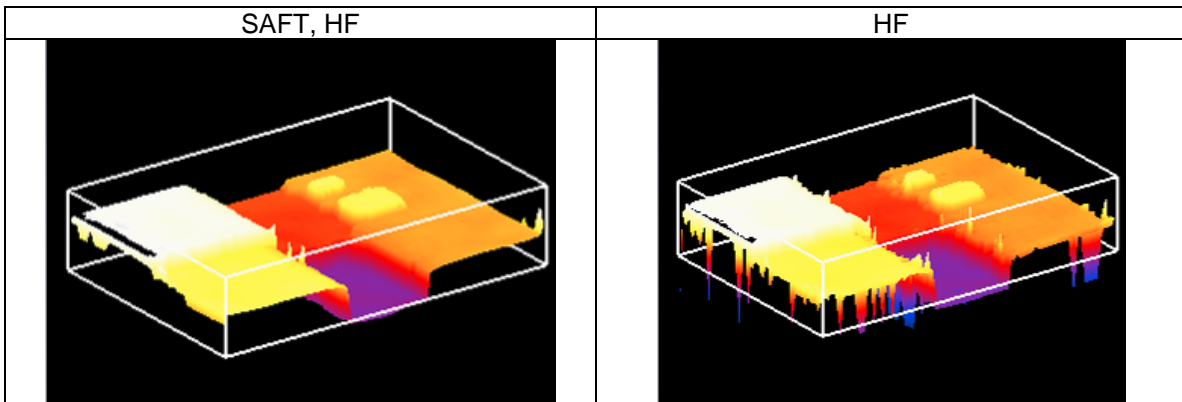


Figure 62: 3D thickness plots, with and without application of the SAFT algorithm.

The histogram in Figure 63 shows five major peaks corresponding to the five different thickness areas (area 3 and 6 both have the same thickness) of the block and two smaller peaks corresponding to the minor thicknesses, respectively.

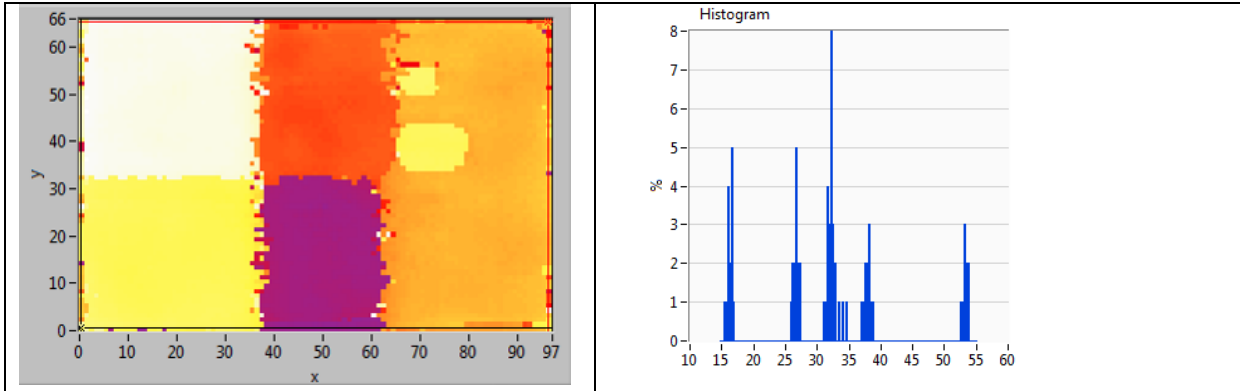


Figure 63: Thickness plot (with SAFT) and histogram.

To evaluate the standard deviation according to the different areas, Figure 64 shows the histograms for all areas separately. To see how far the effects occurring at the edges of the areas with different thicknesses affect the results obtained at these measurement positions, two histograms are determined for every area: one histogram for the whole area including the edges, and one omitting the edges. The statistical parameters obtained for the different areas are listed in Table 10.

The standard deviation is significantly higher if the boundary areas are included in the analysis. This is important for measurement situations where the thickness changes or where the geometry of a structural member is supposed to be assessed, e.g., when the location of girders underneath a slab is supposed to be determined, while at the same time the slab thickness at the edges of the girder is supposed to be measured as accurately as possible. However, there will be many practical cases where the thickness is mostly constant over a wider area and the measurements will be hardly affected by boundary effects. For these cases, the ultrasonic echo method is capable to give relatively precise results with a standard deviation of only a few millimeters.

Including the edges, the standard deviations for the regular thicknesses vary between 6.1 cm and 2.4 cm. If the edges are omitted, the standard deviations are about 0.5 cm, which is relatively low compared to the accuracy that will be relevant for most practical applications.

It should also be noted that the surface of the block is not completely smooth, so that the thickness of the block itself can vary within a range of a few millimeters. The actual accuracy of the ultrasonic echo measurements is therefore even better than the statistical parameters indicate.

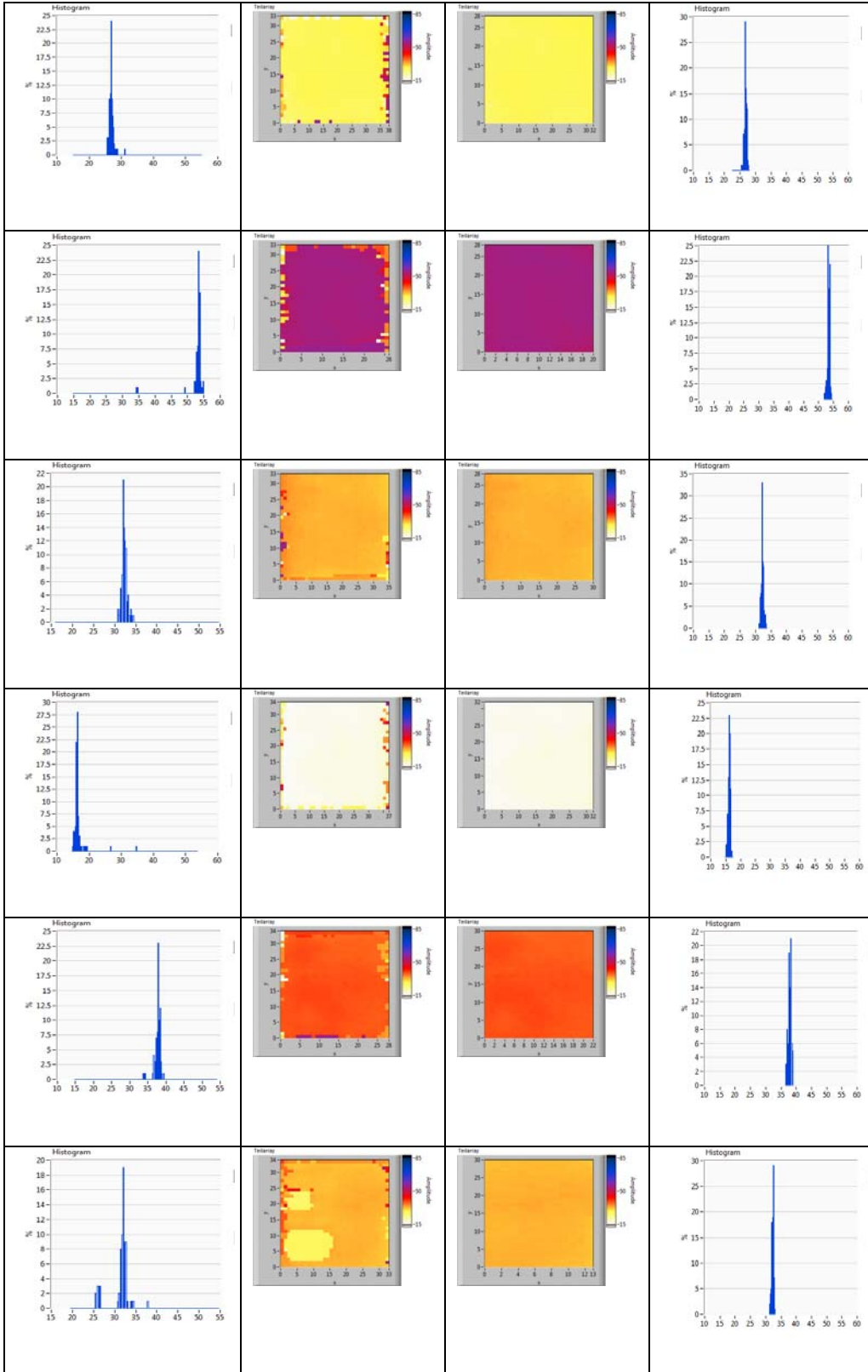


Figure 64: Thickness plots and histograms for the six different areas of the block, with (left) and without (right) the edges of the areas.

Table 10: Statistical results obtained for Specimen 2 with varying thicknesses.

Area 1	Including edges	Omitting the edges
Mean:	27.35 cm	26.84 cm
Standard deviation:	4.21 cm	0.43 cm
Variance:	17.72	0.19
Area 2	Including edges	Omitting the edges
Mean:	51.53 cm	53.36 cm
Standard deviation:	6.13 cm	0.39 cm
Variance:	37.52	0.15
Area 3	Including edges	Omitting the edges
Mean:	32.50 cm	32.25 cm
Standard deviation:	2.38 cm	0.42 cm
Variance:	5.67	0.17
Area 4	Including edges	Omitting the edges
Mean:	17.08 cm	16.18 cm
Standard deviation:	3.80 cm	0.41 cm
Variance:	14.43	0.17
Area 5	Including edges	Omitting the edges
Mean:	37.66 cm	37.90 cm
Standard deviation:	2.84 cm	0.49 cm
Variance:	8.04	0.24
Area 6	Including edges	Omitting the edges
Mean:	31.43 cm	32.18 cm
Standard deviation:	2.91 cm	0.34 cm
Variance:	8.47	0.12

5.4.2 Impact-Echo Measurements

The results obtained from the impact-echo measurements are depicted as B-scans in Figure 65 as well as in the two averaged D-scans in Figure 66, each of them comprising one half (in y-direction) of the block. All B-scans are dominated by geometry effects caused by reflections of the waves at the boundaries of the block. These geometry effects interfere with the actual backwall reflections that appear as mostly continuous lines and indicate the block thickness. In consequence, the thickness becomes less distinctive. The impact-echo sensor used here is designed for frequencies higher than 2 kHz. Therefore, frequencies below 2 kHz are not depicted in the B-scans. Especially in Figure 65a) and b) it becomes clear that thickness indications in the higher frequency range (corresponding to lower thicknesses) normally appear together with indications in the lower frequency range (falsely indicating higher thicknesses). Although a clear indication at around 13 kHz can be seen, it appears together with an indication below 5 kHz. This is due to the flexural oscillation mode, which becomes the more dominant the thinner the slab thickness gets. This effect can be misleading, since the thickness value for every measurement position is determined by picking the frequency value with the highest amplitude and calculating the corresponding depth according to the impact-echo equation: $d=v/2f$. With the low frequency indications due to the flexural oscillation mode, the procedure would pick these low-frequency indications and therefore give very high thicknesses at positions where the actual thickness is rather thin. To avoid this effect, the frequency range, in which the indications are picked, has to be adjusted accordingly, i.e., indications below a certain threshold frequency have to be ignored. However, this requires some prior information about the dimensions of the approximate thickness of the test object. Furthermore, if the thickness changes drastically over the measurement area, parts of this area with higher thicknesses will not be detected because of the threshold frequency, which was set according to those areas with lower thickness. This is demonstrated in the B-scans of Figure 65 where for all B-scans the indication with the highest amplitude above a threshold frequency of 5 kHz is picked and plotted as a red dot at the respective position in the B-scan (small image next to the actual B-scan). It can be seen that the areas with lower thickness (high frequencies) are picked correctly. At the same time, areas with higher thickness are not being detected, because the frequency threshold ignores any indication below 5 kHz.

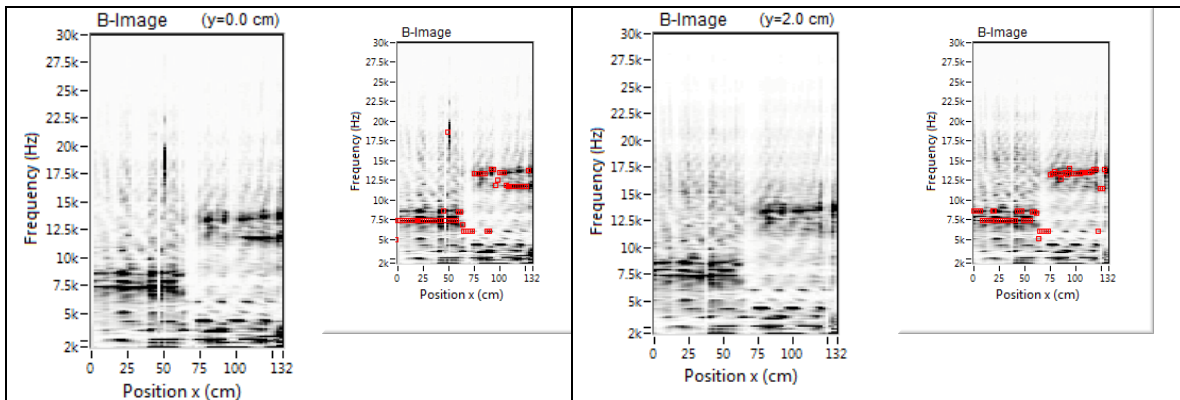


Figure 65a: Impact-Echo B-Scans, lines 0 – 1, (0 - 2 cm)

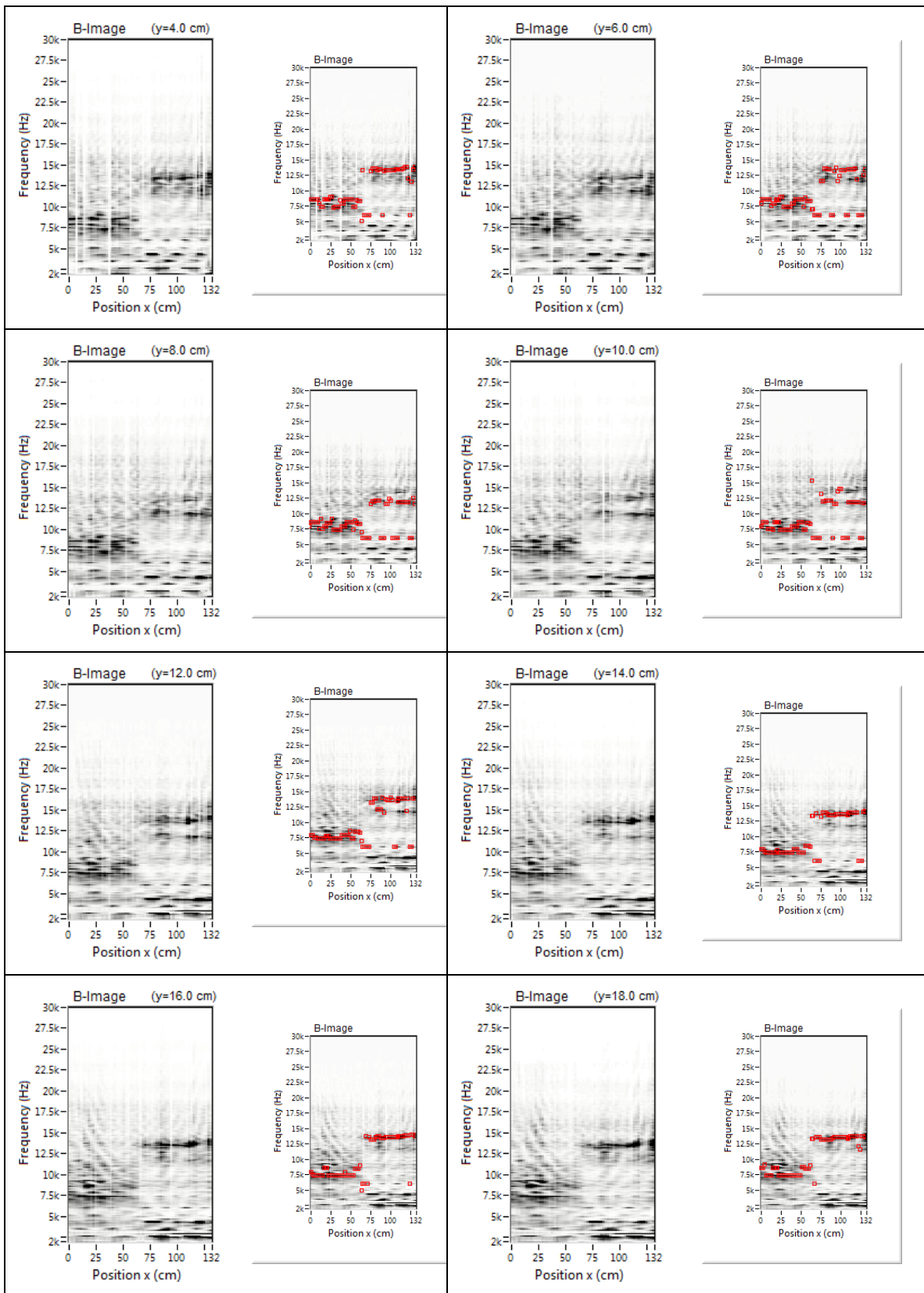


Figure 65b: Impact-Echo B-Scans, lines 2 – 9, (4-18 cm)

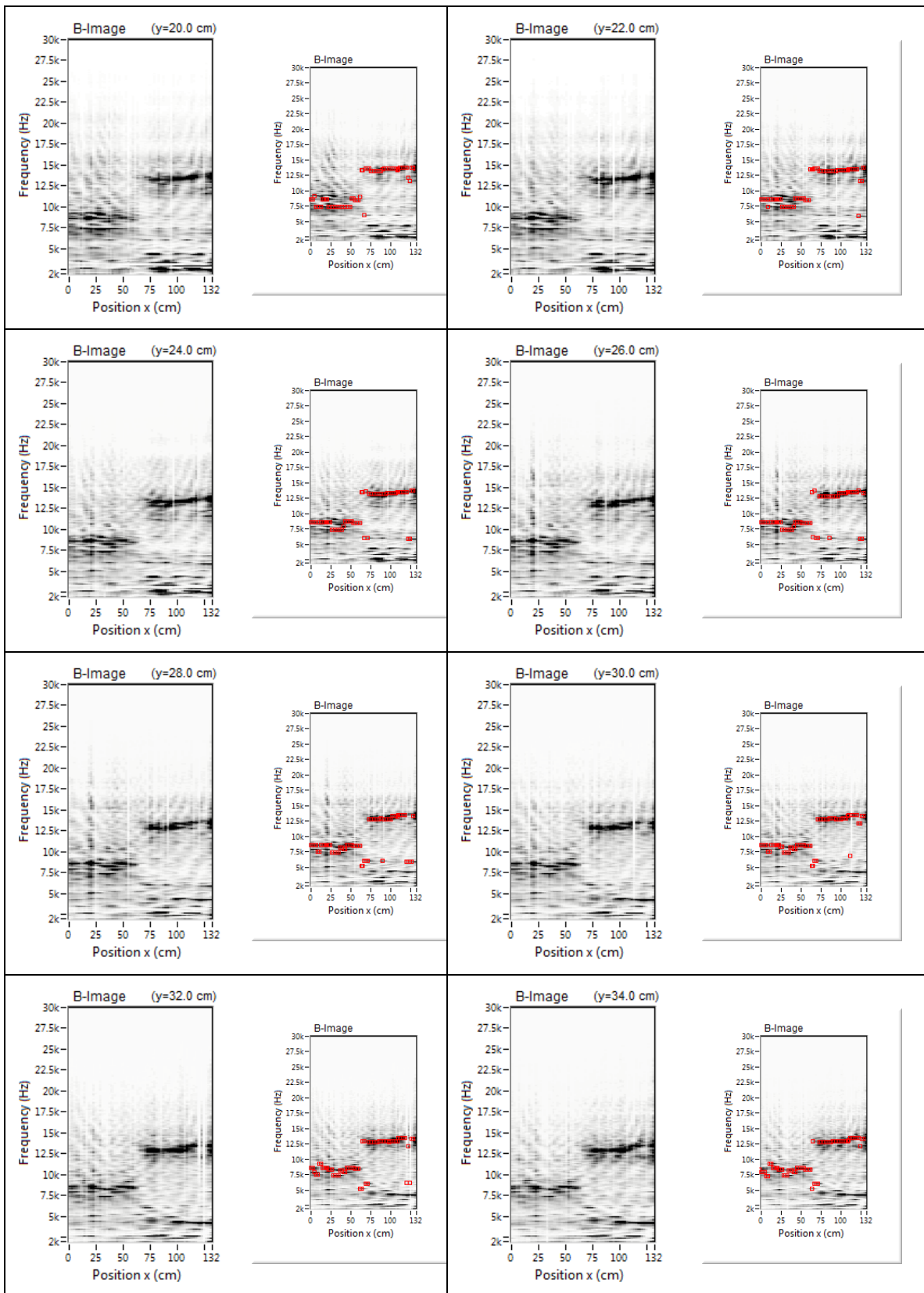


Figure 65c: Impact-Echo B-Scans, lines 10 – 17, (20 -34 cm)

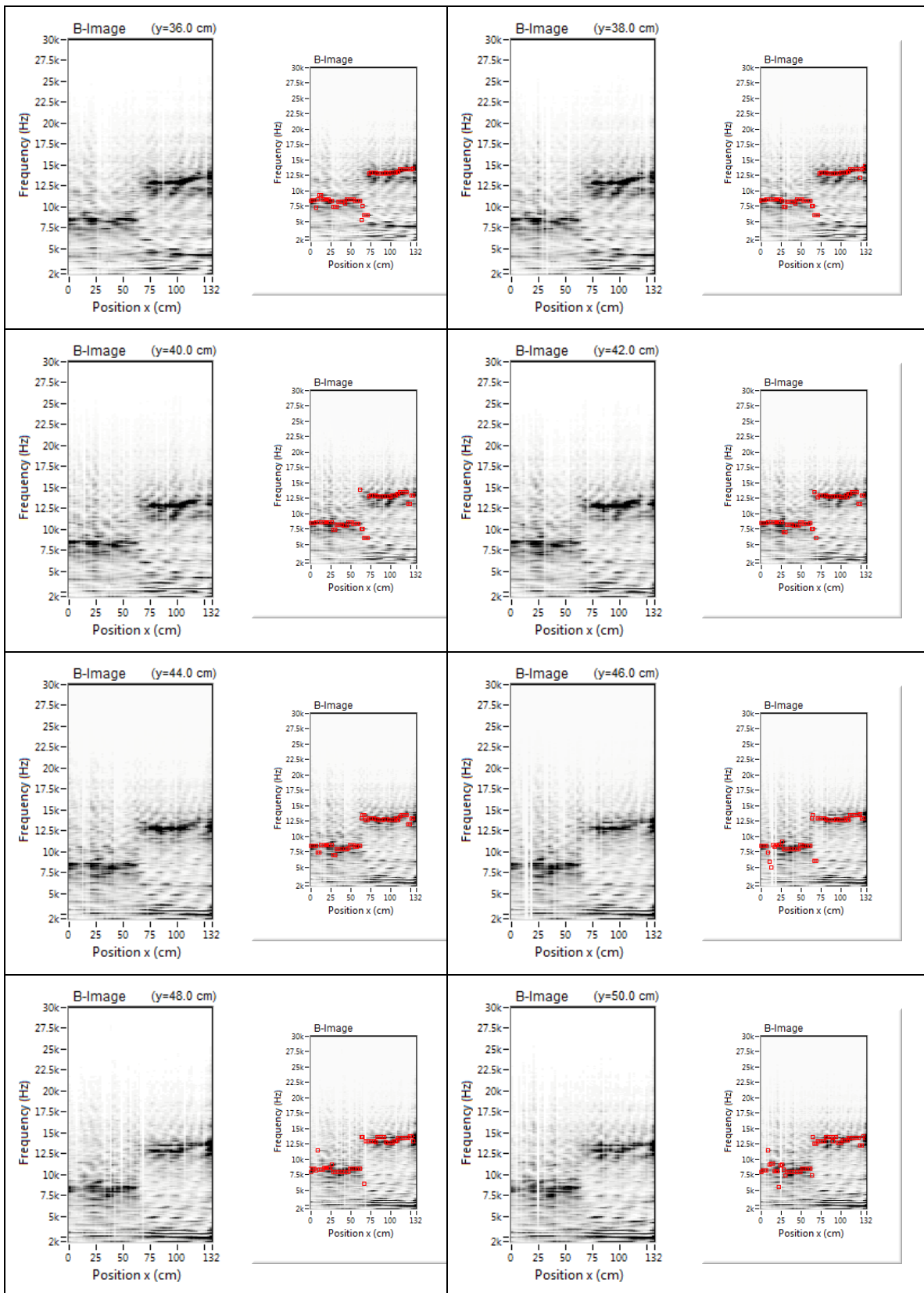


Figure 65d: Impact-Echo B-Scans, lines 18 – 25, (36 – 50 cm)

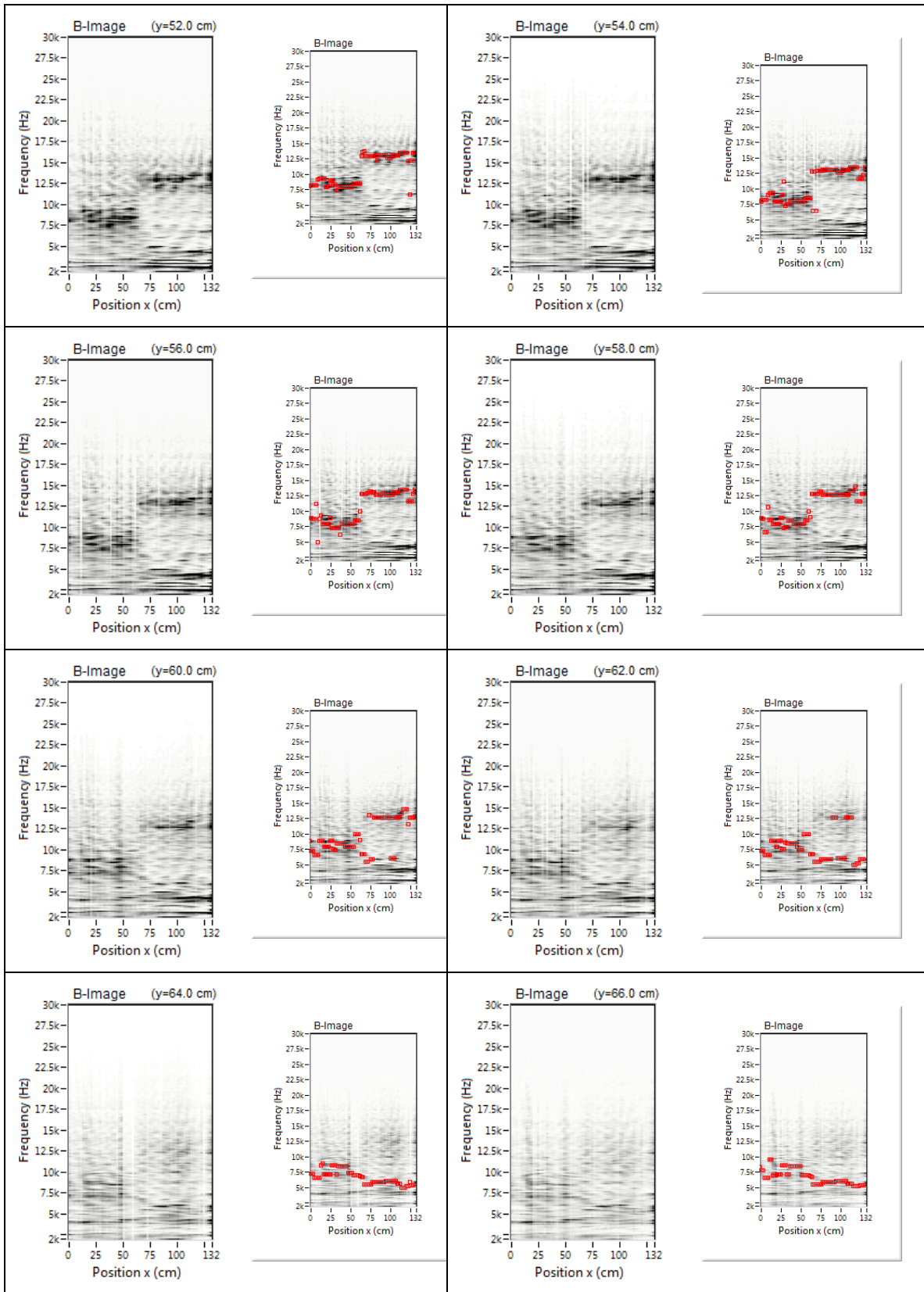


Figure 65e: Impact-Echo B-Scans, lines 26 – 33, (52 -66 cm)

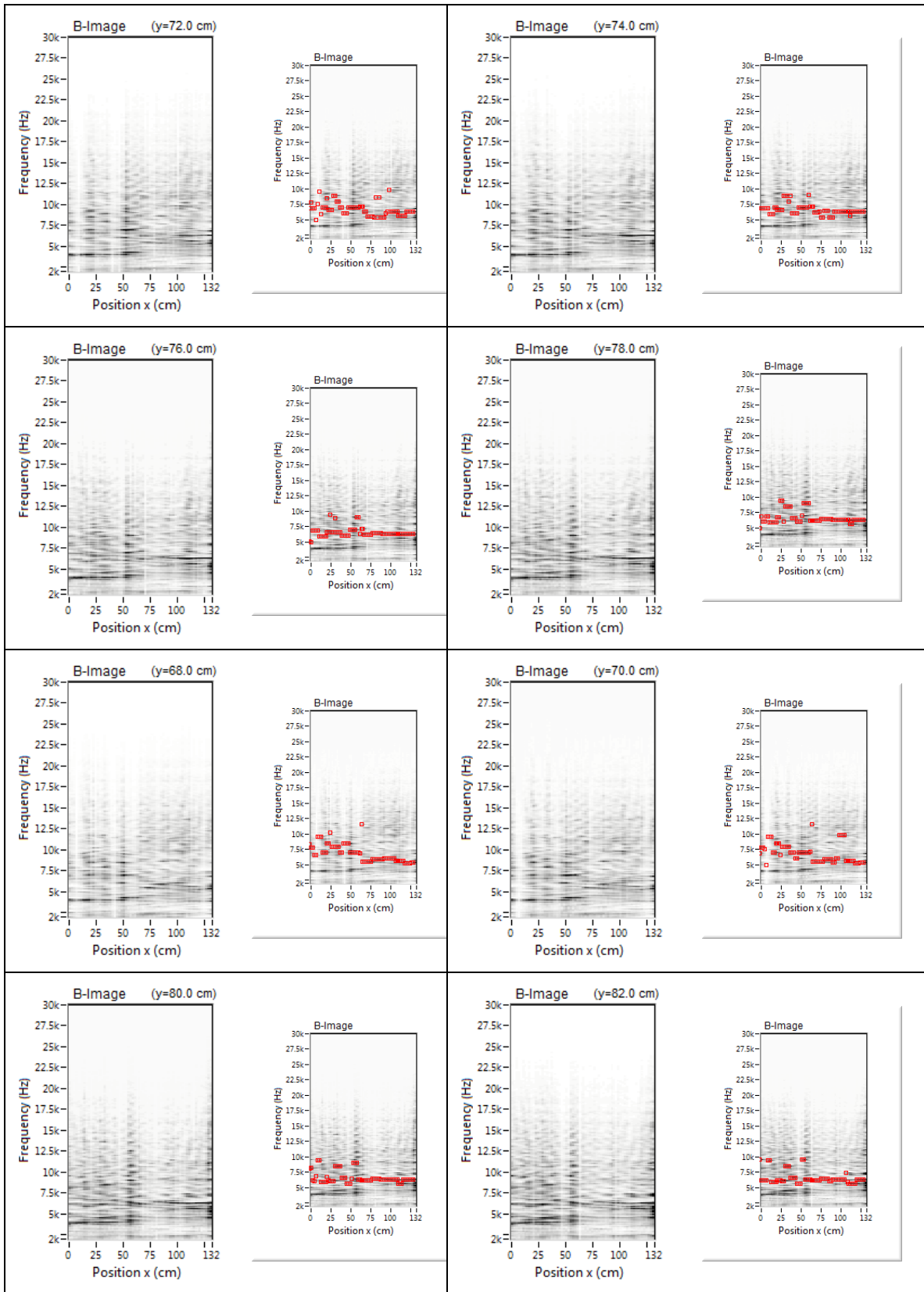


Figure 65f: Impact-Echo B-Scans, lines 36 – 41, (72 -82 cm)

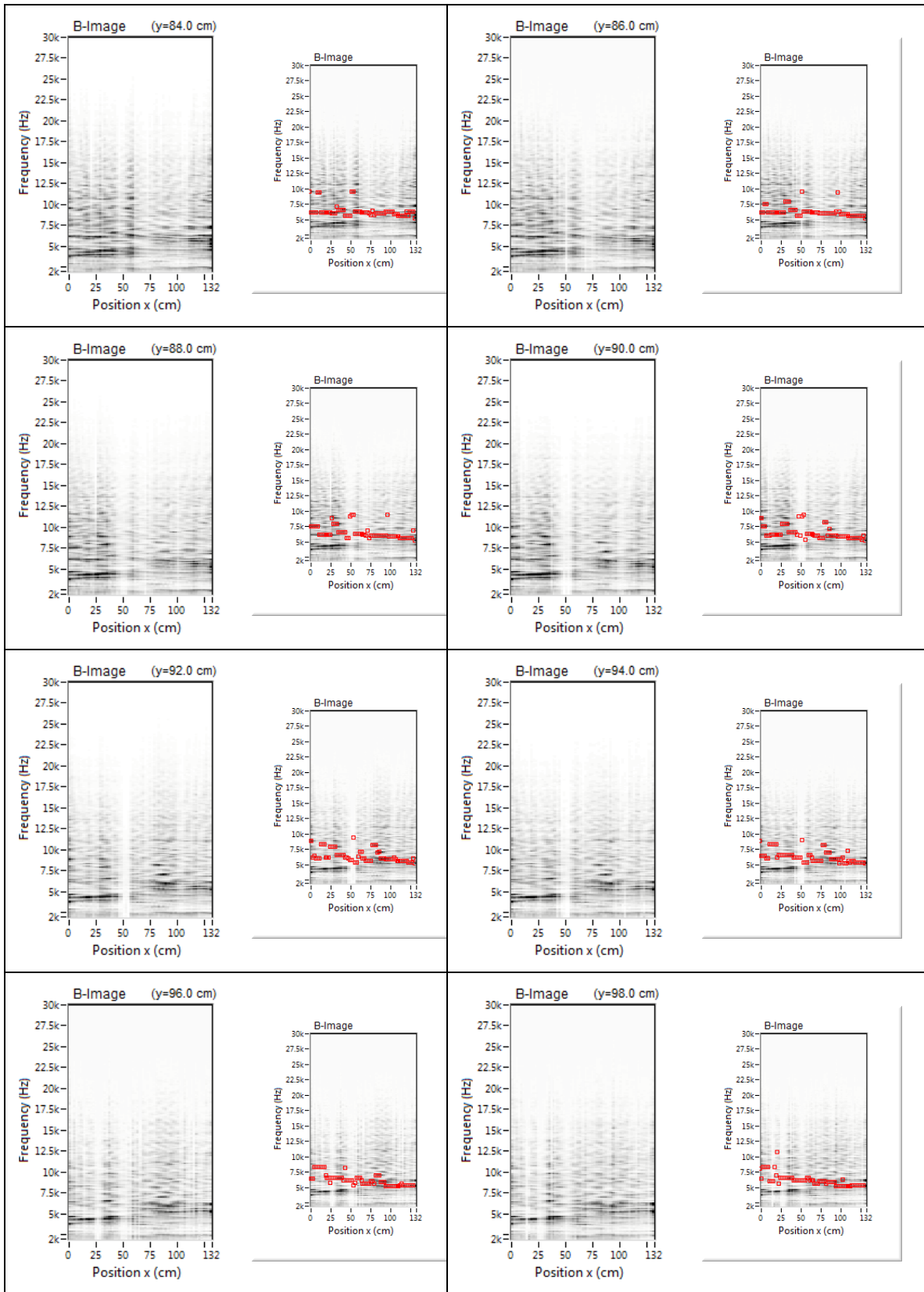


Figure 65g: Impact-Echo B-Scans, lines 42 – 49, (84 -98 cm)

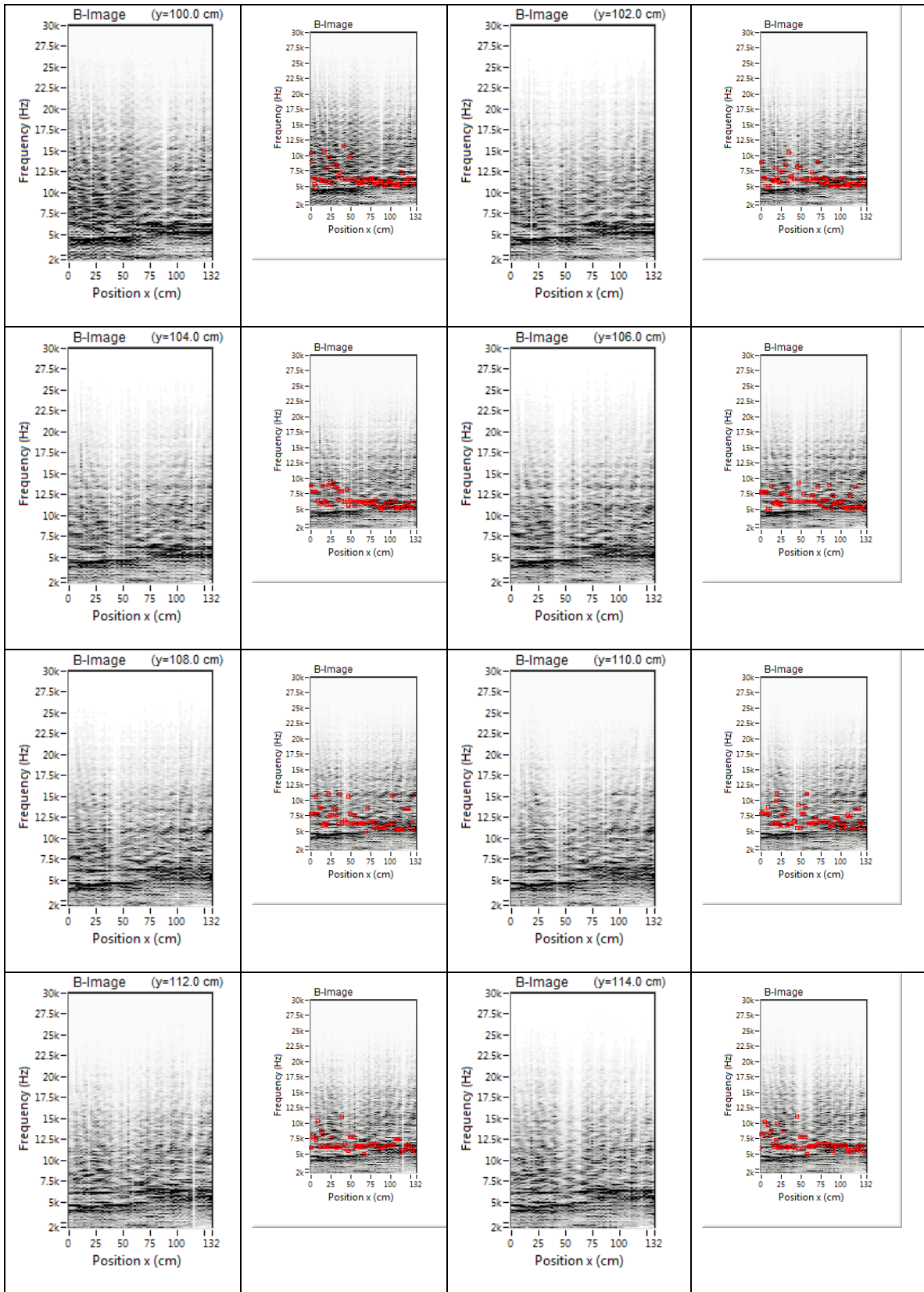


Figure 65h: Impact-Echo B-Scans, lines 50 – 57 (100 -114 cm)

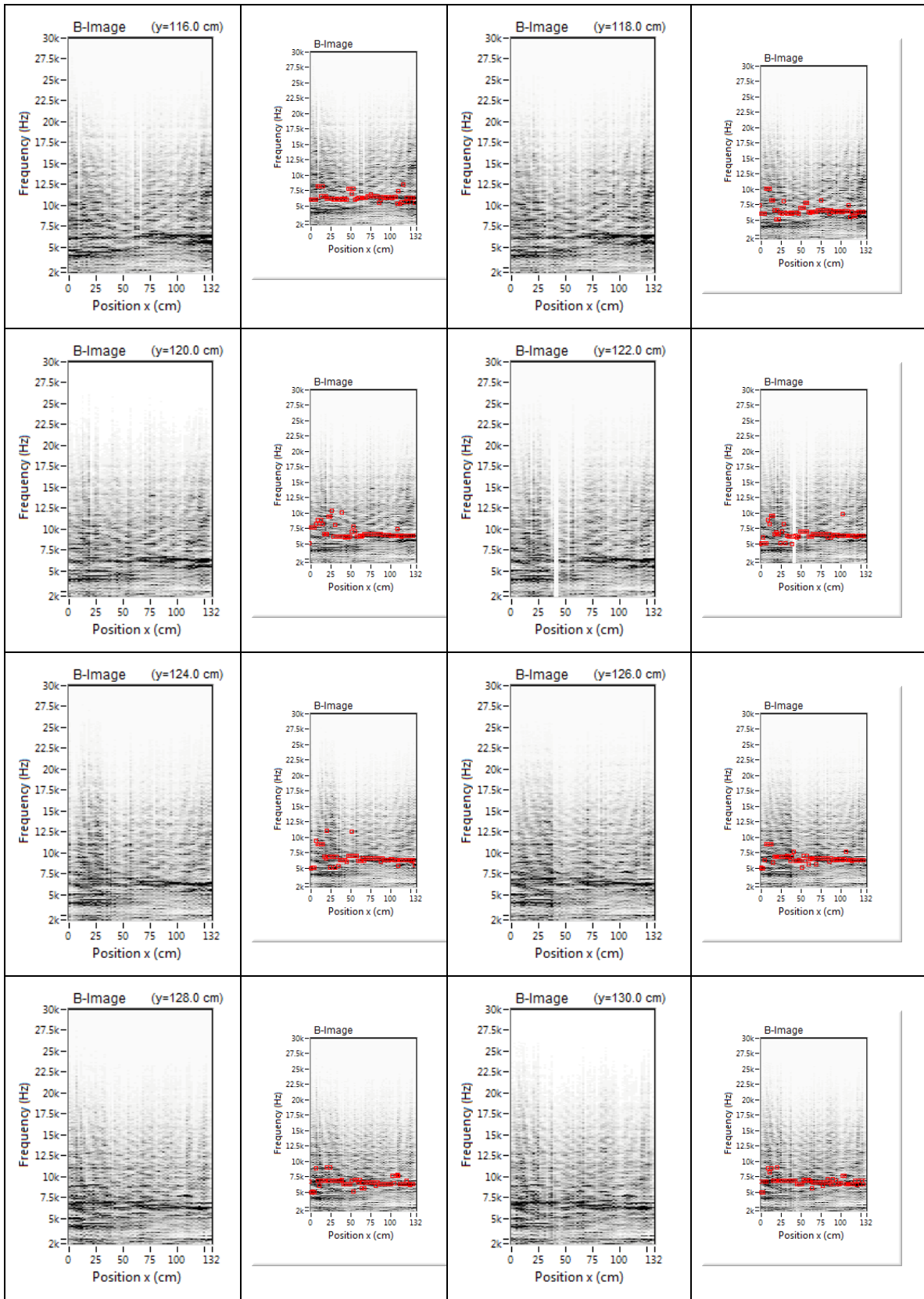


Figure 65i: Impact-Echo B-Scans, lines 58 – 65, (116 -130 cm)

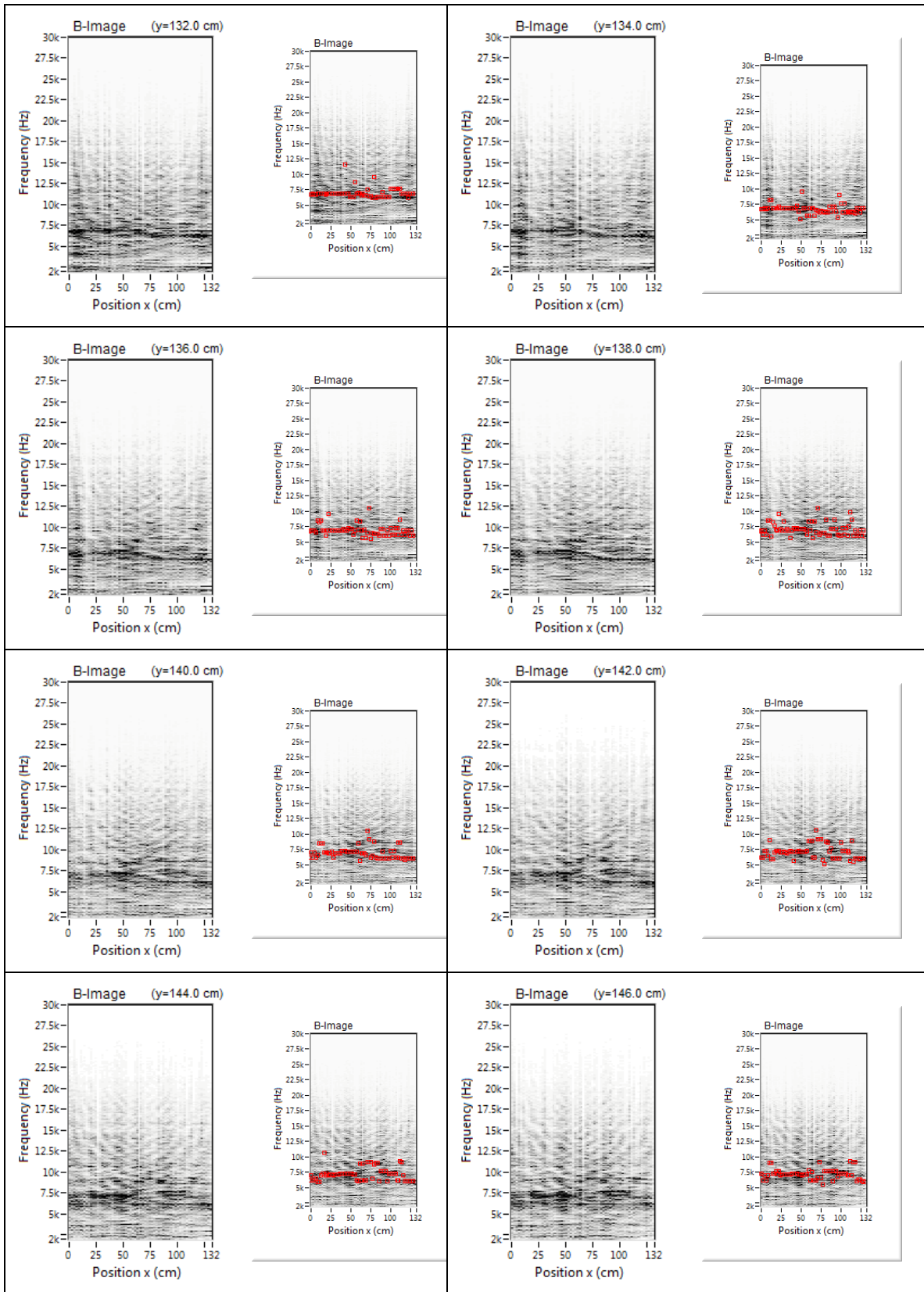


Figure 65j: Impact-Echo B-Scans, lines 66 – 73, (132 -146 cm)

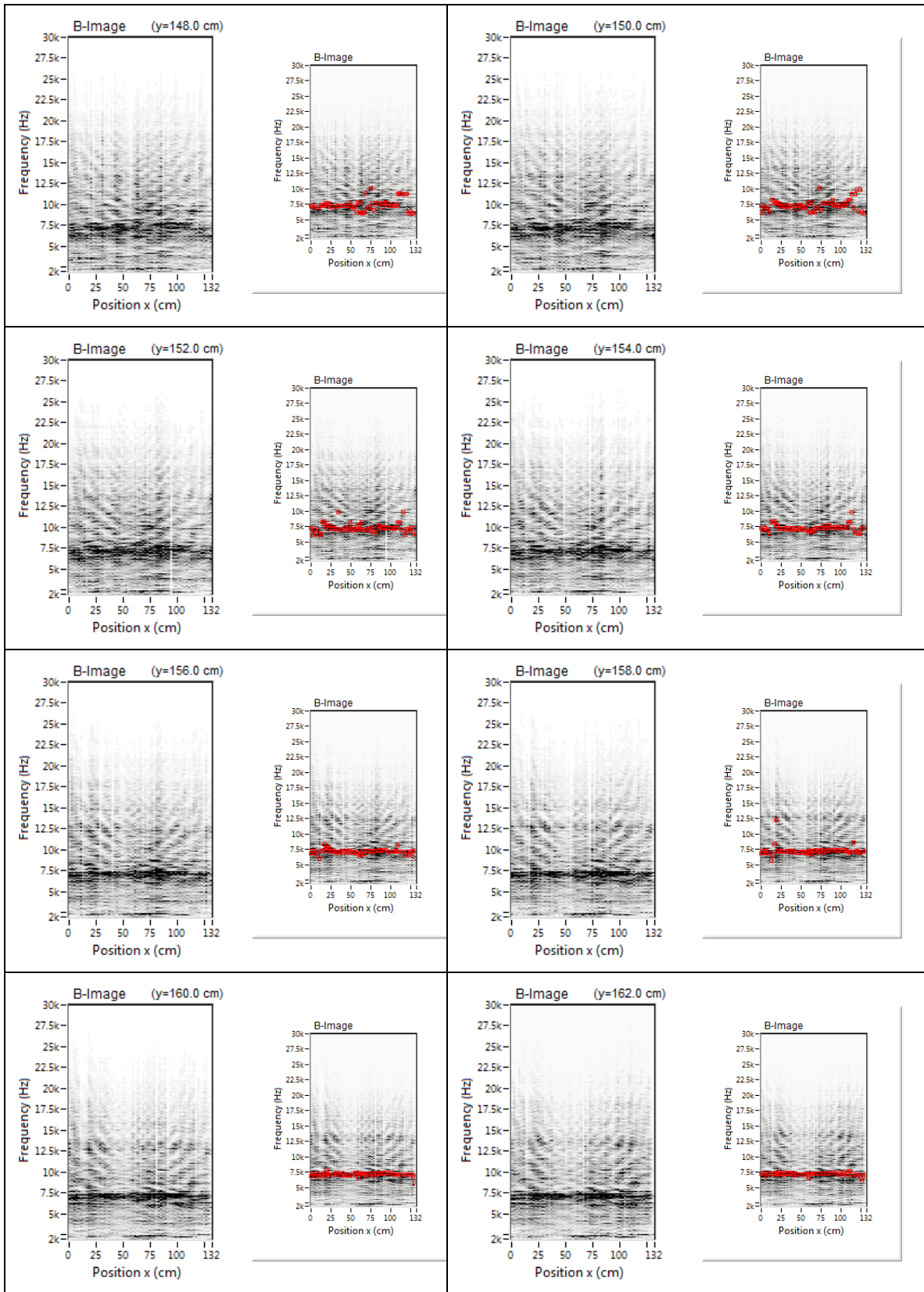


Figure 65k: Impact-Echo B-Scans, lines 74 – 81, (148 -162 cm)

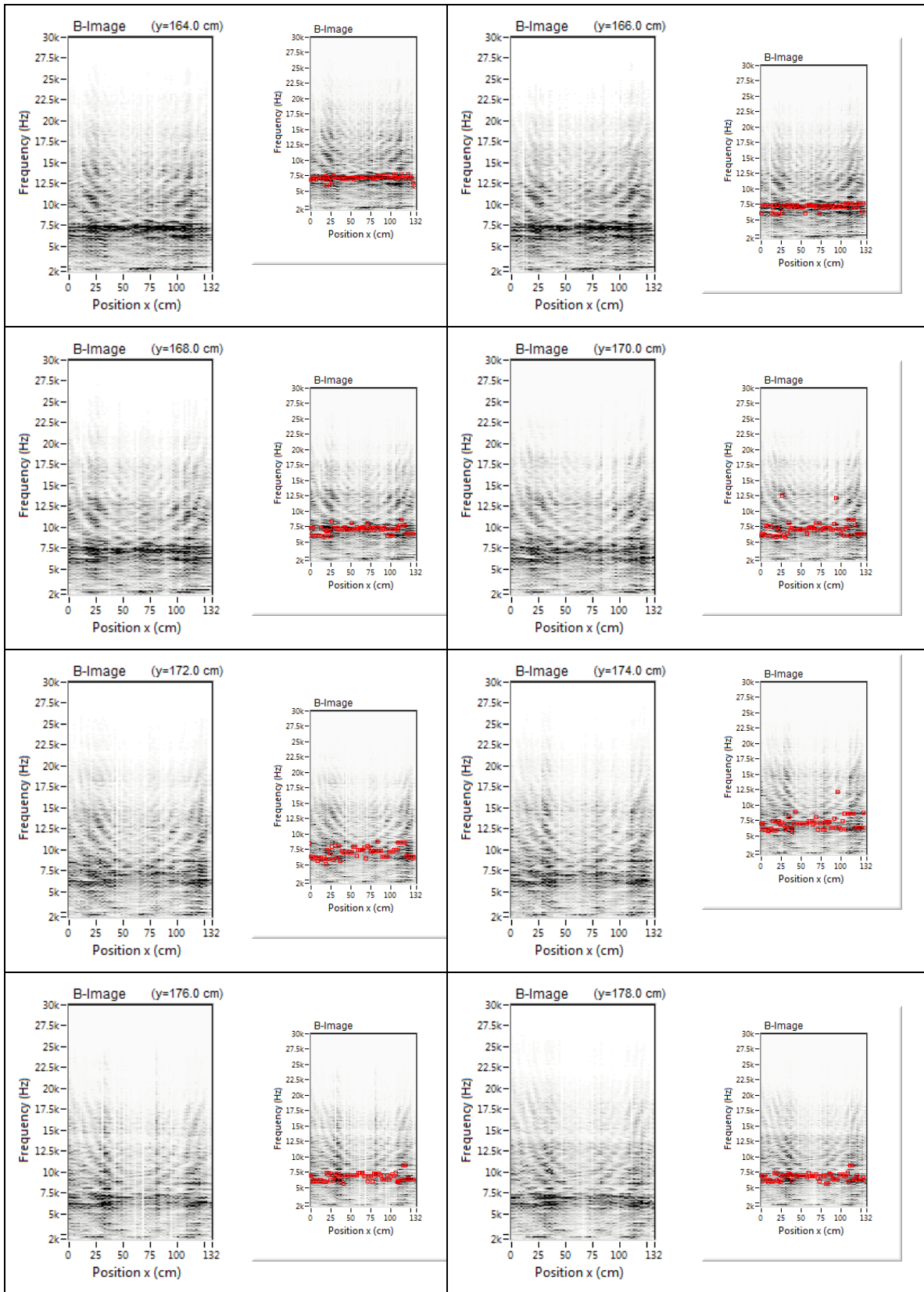


Figure 65I: Impact-Echo B-Scans, lines 82 – 89, (164 -178 cm)

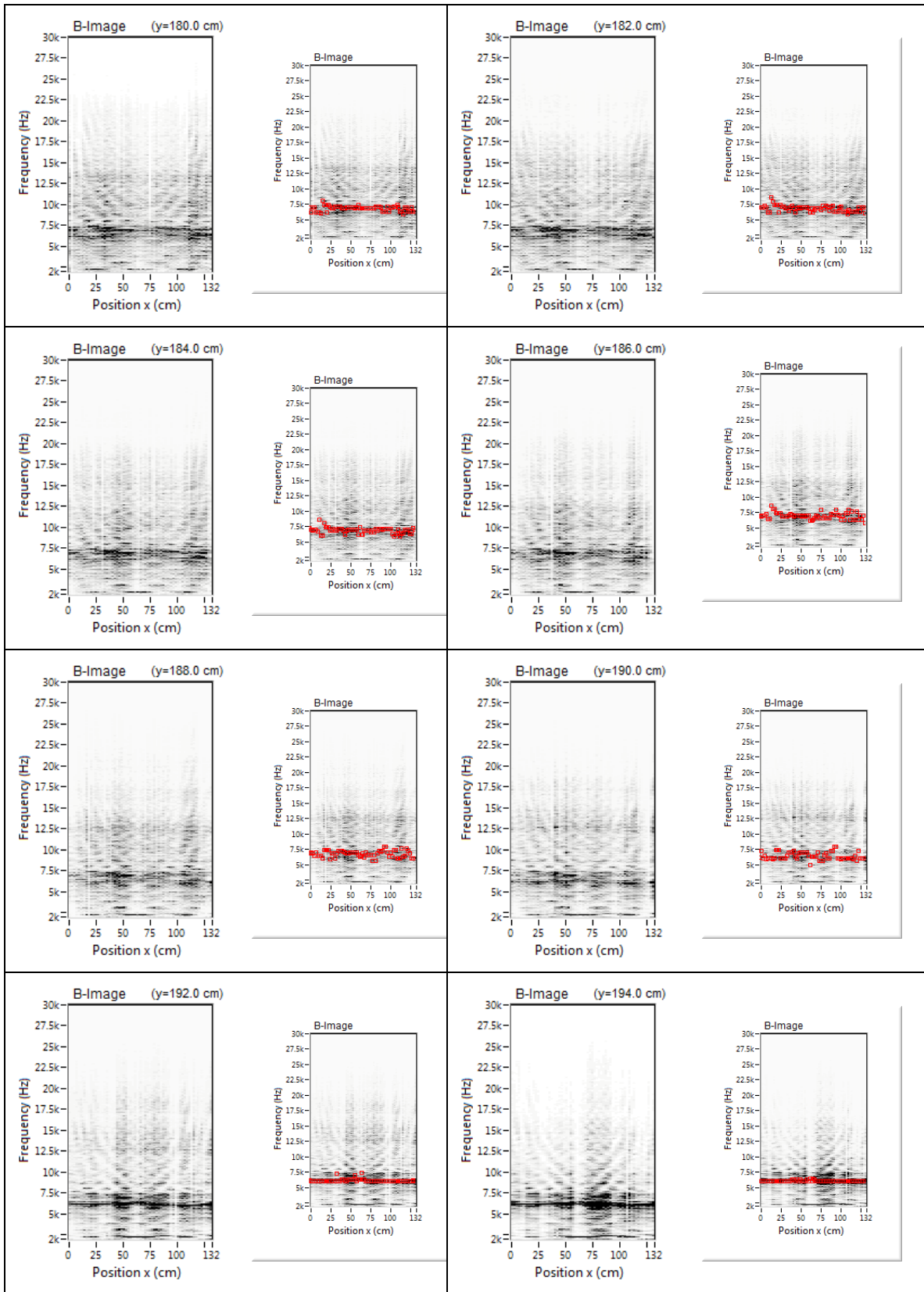


Figure 65m: Impact-Echo B-Scans, lines 90 – 97, (180 -194 cm)

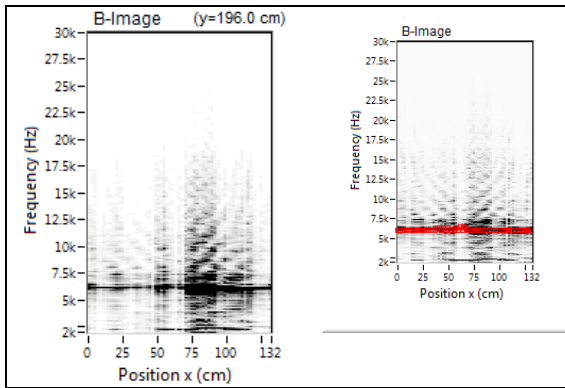


Figure 65n: Impact-Echo B-Scans, line 98, (196 cm)

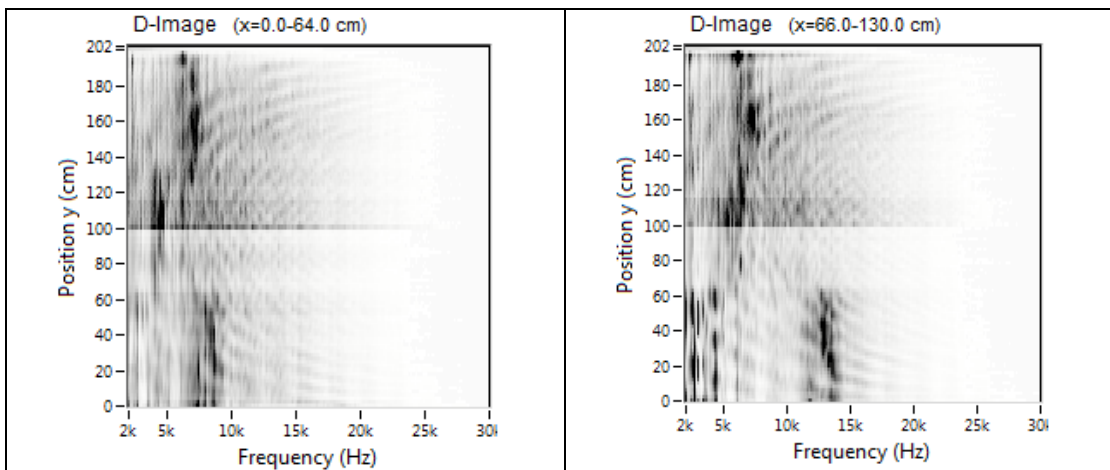


Figure 66: D-Scans (perpendicular to scan direction, crossing the B-Scans) averaged over the lower and upper half of the block. In both cases the three areas with different thicknesses can be seen.

In Figure 67 the thickness values obtained are plotted over the measurement area using a color code. Taking into account indications within the frequency range of 5 kHz to 25 kHz, only areas 1 and 4 show up as relatively smooth surfaces with relatively defined edges in the plot. The areas 2 and 4 cannot be identified, since their thicknesses correspond to frequencies lower than the threshold frequency of 5 kHz. For the areas 3 and 6, the indications obtained are approximately 300 mm (12"). However, the surface obtained is not completely smooth but shows certain variations. Furthermore, due to the artifacts obtained for the areas 2 and 3, the edges between areas 2 and 3 as well as areas 5 and 6 are not well defined. Lowering the frequency threshold to 3 kHz or 2 kHz results in disruption of the indications obtained from the areas with lower thickness and only partly improves the quality of the indications obtained from the thicker areas.

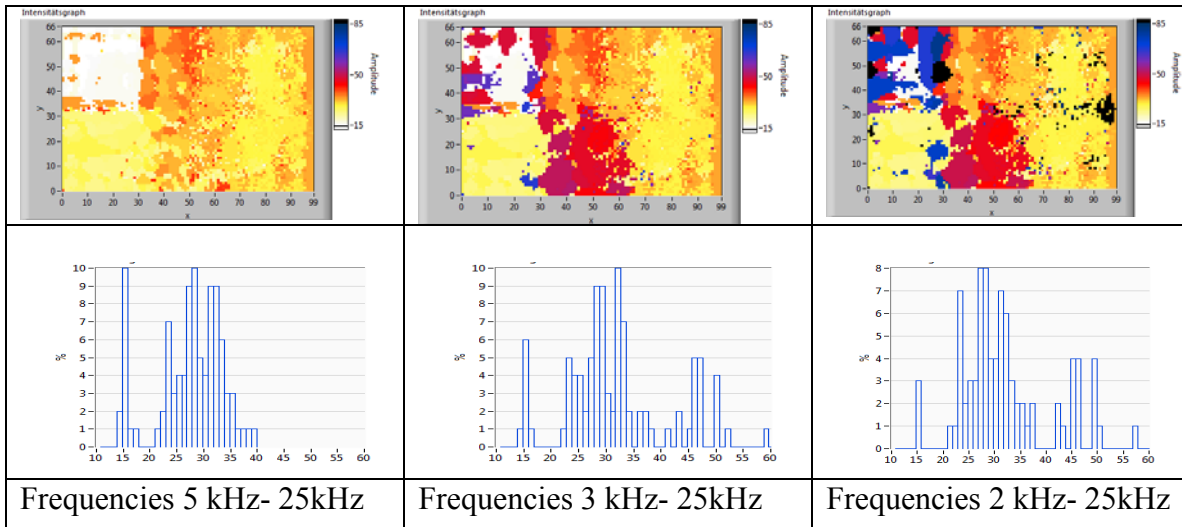


Figure 67: Thickness plots and histograms obtained for different frequency ranges.

The histograms obtained from the different areas 1-6 are listed in Figure 68, Figure 69 and Figure 70 for the different frequency thresholds. The comparison with the histograms obtained from the ultrasonic measurements also makes it obvious that the ultrasound-echo results are by far more precise. The standard deviations are significantly higher for the impact-echo results than for the ultrasonic-echo results.

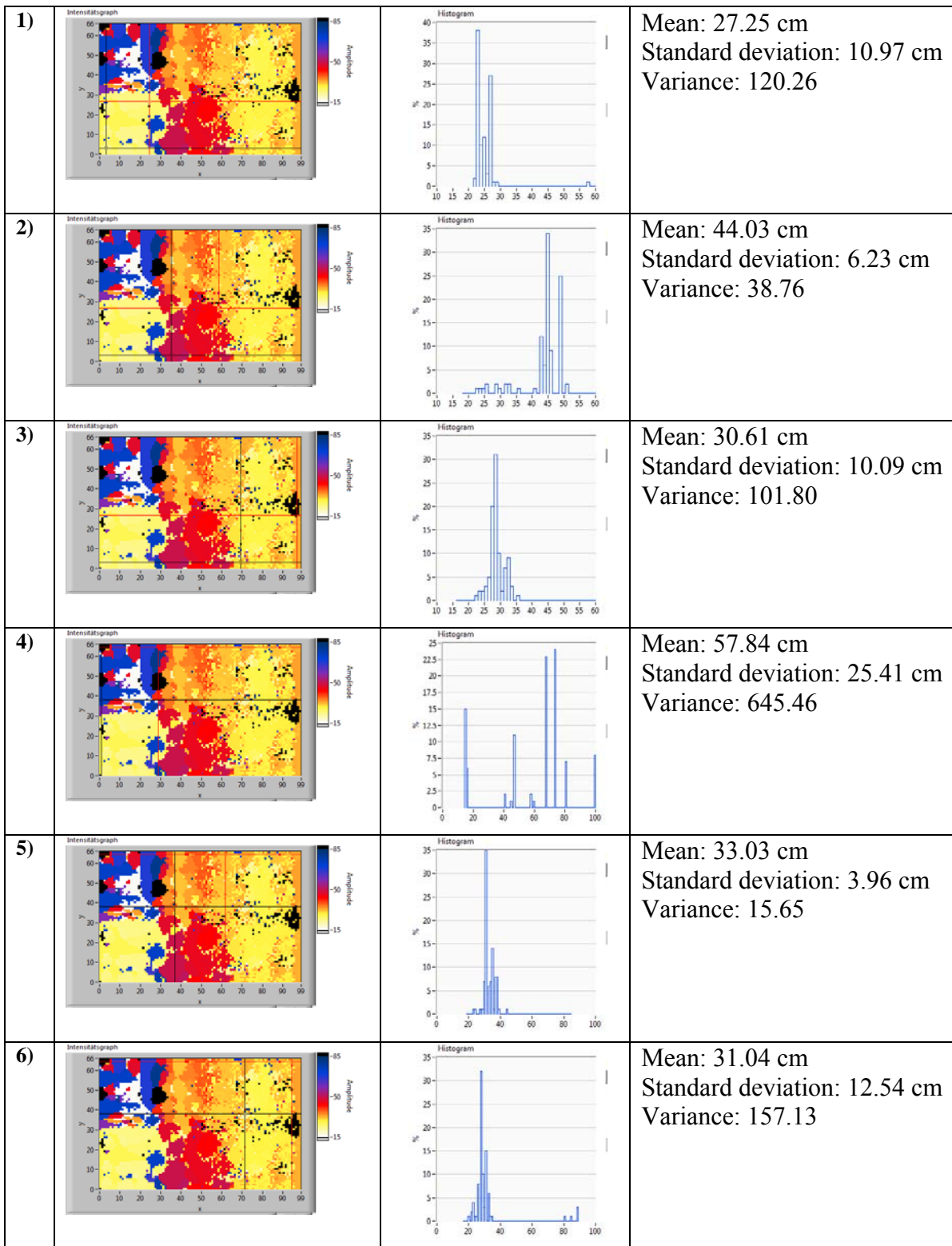


Figure 68: Histograms obtained for the different areas 1 – 6 of the block, frequencies 2 kHz -25 kHz.

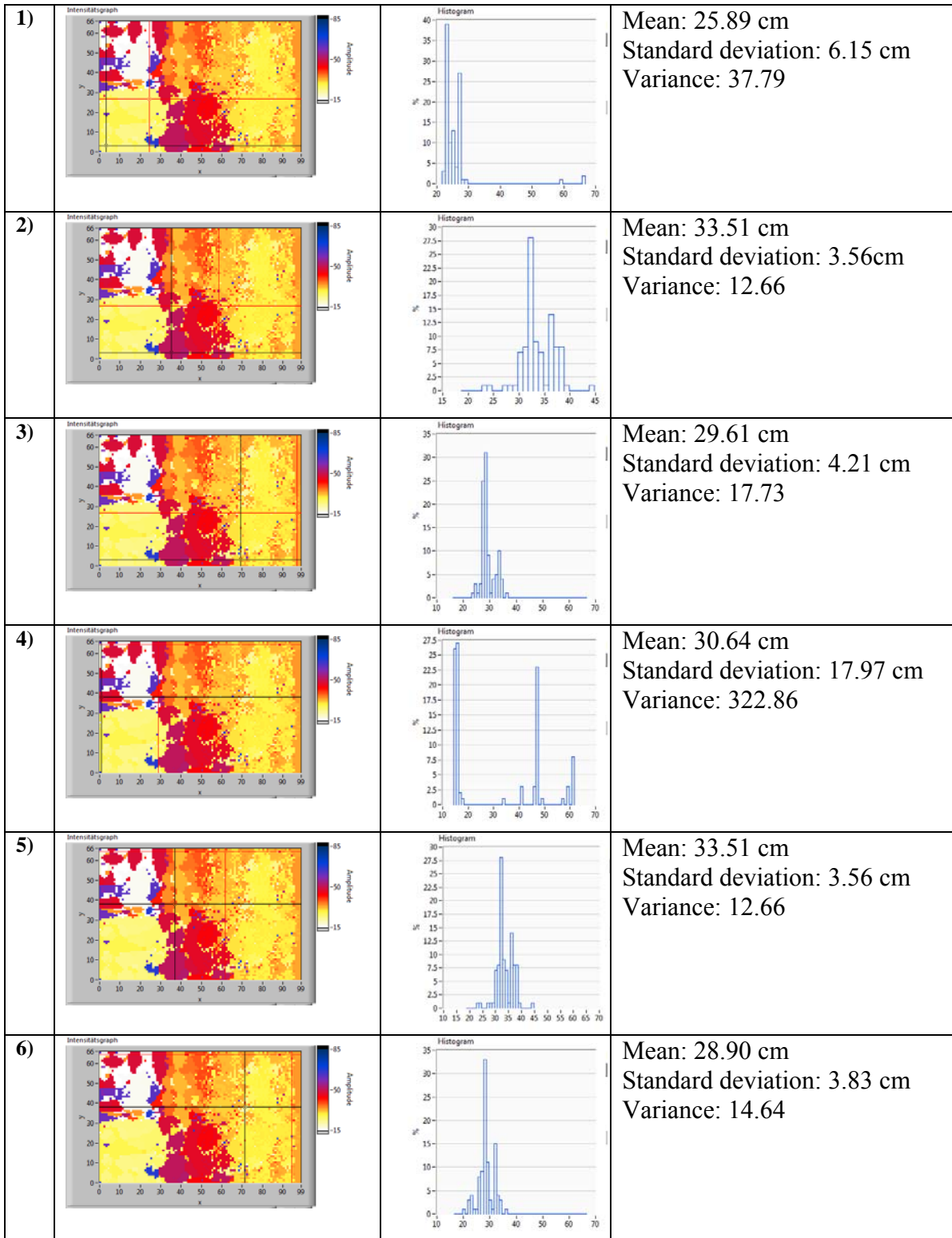


Figure 69: Histograms obtained for the different areas 1 – 6 of the block, frequencies 3 kHz -25 kHz.

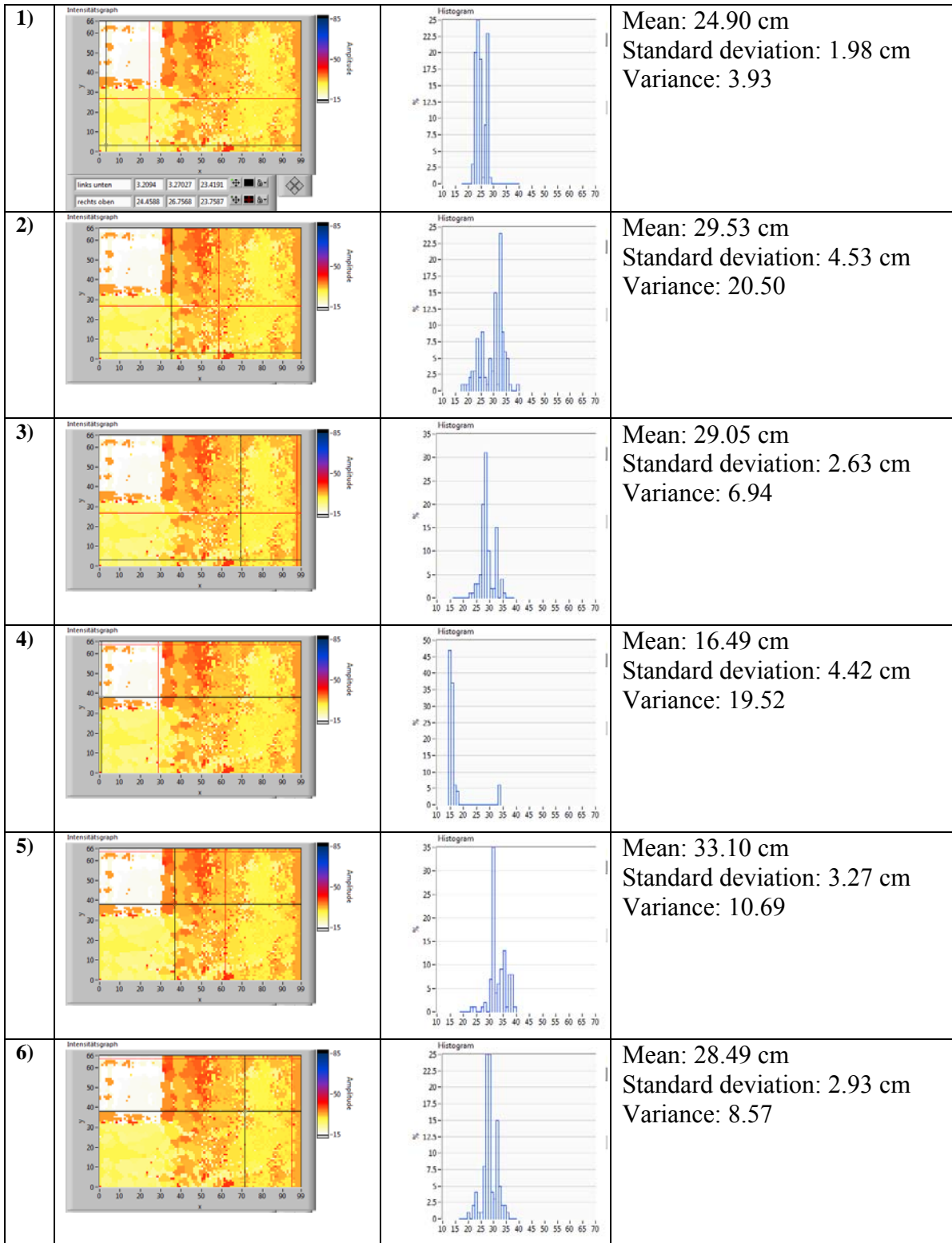


Figure 70: Histograms obtained for the different areas 1 – 6 of the block, frequencies 5 kHz -25 kHz.

5.5 Tendon Duct Block

The focus of the measurements carried out on the tendon duct block was to see how accurately the tendon ducts can be located in the block and if the different areas with different grouting states (empty, fully or half grouted) can be identified. Therefore, acoustic methods, ultrasonic-echo and impact-echo were used. In addition, scans with the covermeter were taken to see if this device can detect the tendon ducts. Although a covermeter would probably not be used for that in practice, it should be included in this study, especially as it is important to see how far the presence of tendon ducts in a component can affect covermeter measurements for determining the location of rebars.

5.5.1 Impact-Echo Measurements

Measurements taken from the front of the block

The impact-echo measurements were carried out along a 20 mm × 20 mm (0.8" × 0.8") grid. The D-scans crossing the tendon ducts are given in Figure 71a and b. In all D-scans, the indication of the backwall appears to be shifted towards lower frequencies at the location of the duct. The amount of this shift is different for the different ducts. Nevertheless, it seems that for all ducts the amount of this shift stays mostly constant over the whole length of the duct.

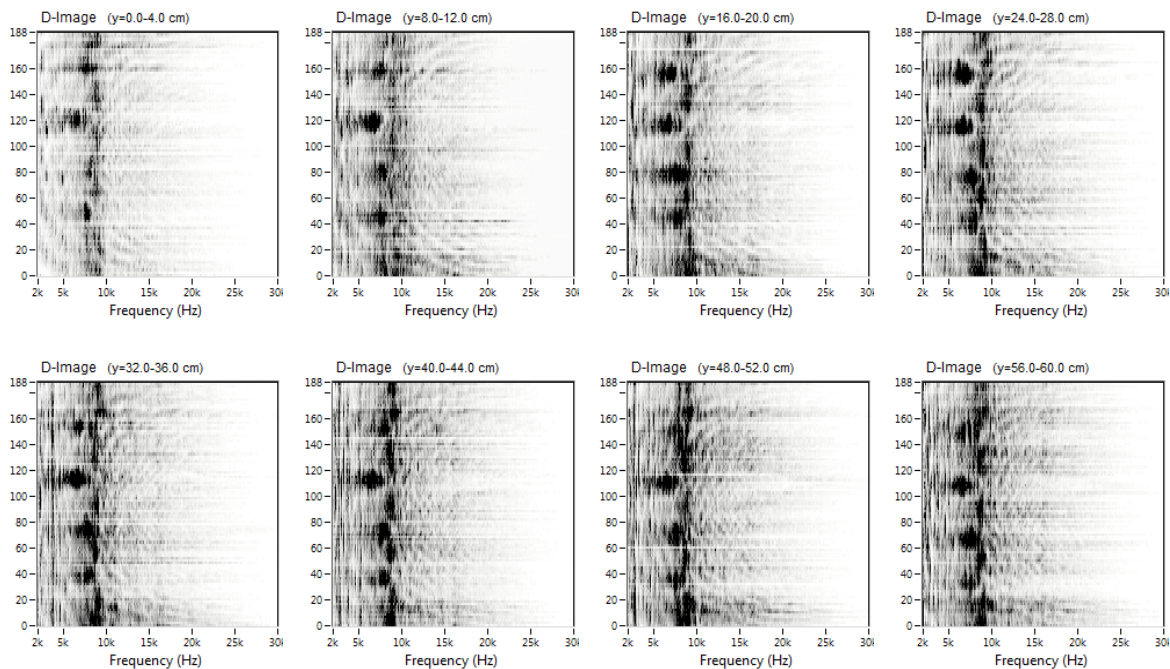


Figure 71a: D-Scans crossing the tendon ducts, ranging from y = 0 cm to y =60 cm.. Measurements were taken from the front of the block. At the positions of the ducts a backwall shift is clearly visible.

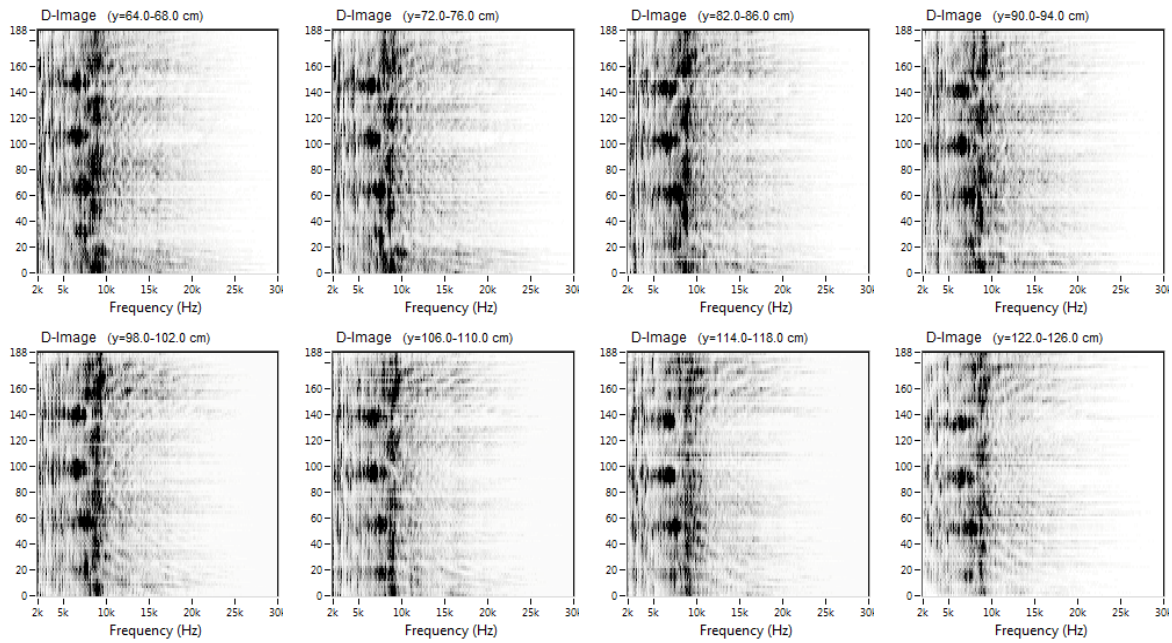


Figure 71b: D-Scans crossing the tendon ducts, ranging from $y = 64$ cm to $y = 126$ cm. Measurements were taken from the front of the block. At the positions of the ducts a backwall shift is clearly visible.

This can as well be seen in the C-scans in Figure 72a-c, where the ducts appear with maximum intensity in different C-scans corresponding to different frequencies, but every duct appears in full and not in different pieces, as would be the case if the grouted and empty areas appeared at different frequencies. In consequence, it cannot be distinguished between the grouted and empty areas based on the quantity of the backwall shift, as it was hoped.

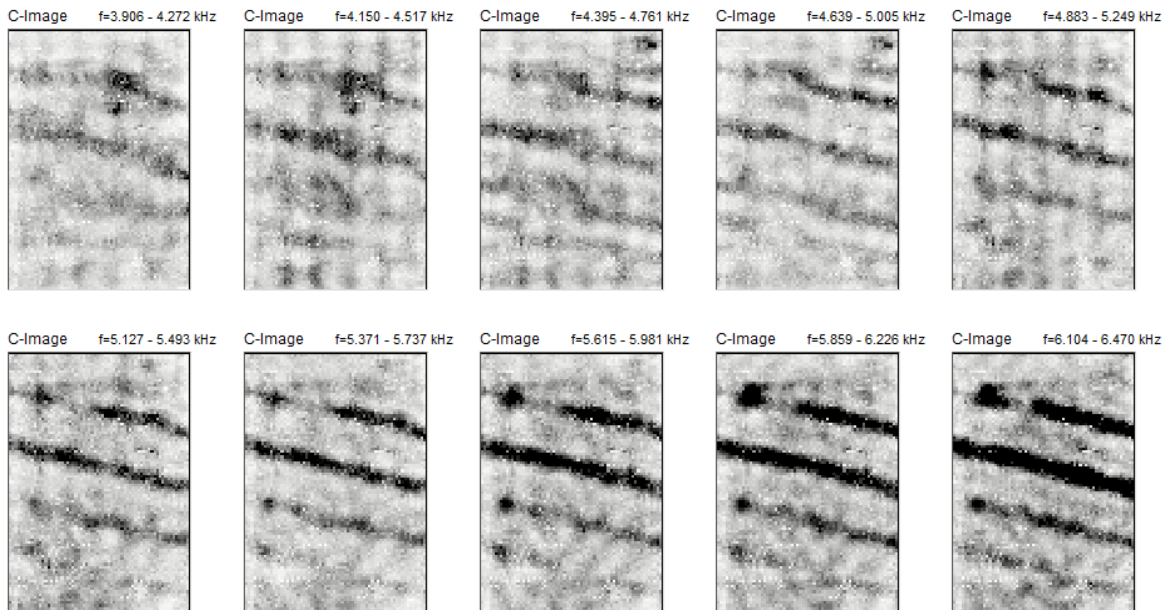


Figure 72a: C-Scans in the frequency range 4 kHz – 6 kHz. Measurements were taken from the front of the block. The given scans are projections obtained by averaging three consecutive scans, so that every image is an average over a frequency range of 0.366 kHz.

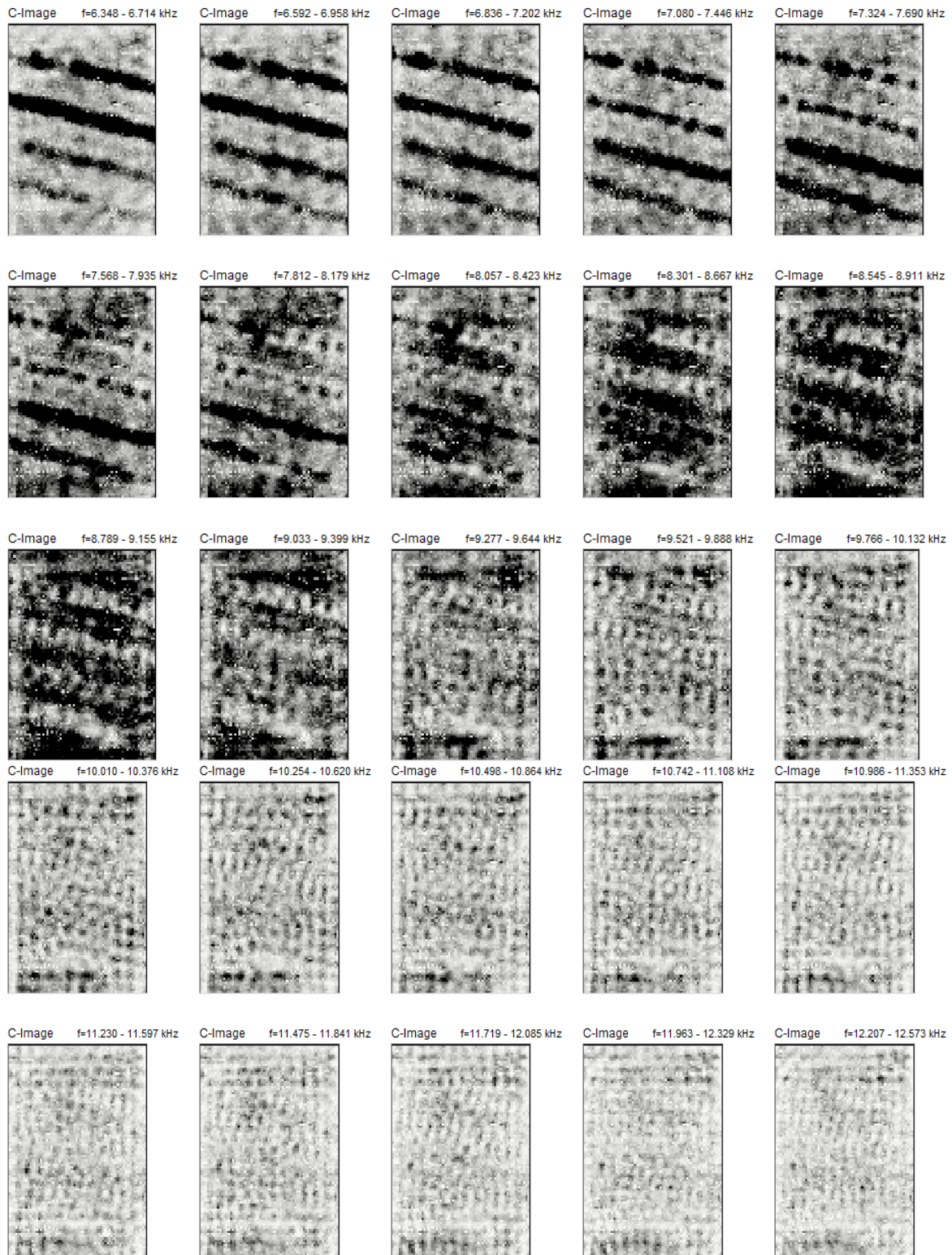


Figure 72b: C-Scans in the frequency range 6 kHz – 12 kHz. Measurements were taken from the front of the block. The given scans are projections obtained by averaging three consecutive scans, so that every image is an average over a frequency range of 0.366 kHz.

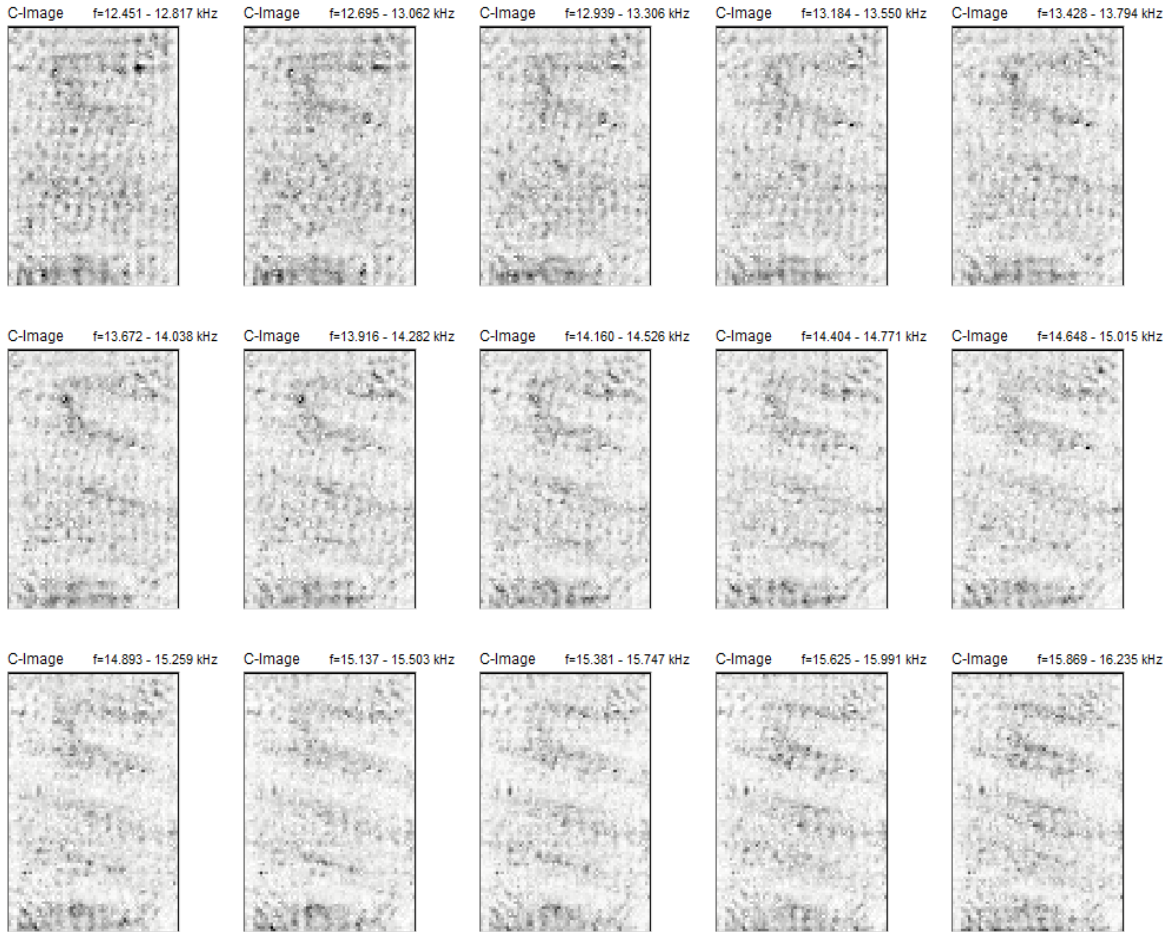


Figure 72c: C-Scans in the frequency range 12 kHz – 16 kHz. Measurements were taken from the front of the block. The given scans are projections obtained by averaging three consecutive scans, so that every image is an average over a frequency range of 0.366 kHz.

Figure 73 shows a 3D thickness plot obtained by picking the frequency with maximum amplitude at every measurement position. The apparent backwall shift at the position of the ducts is clearly visible here as well. It can also be seen that the shift is higher for the first two ducts (blue color) than for the other two ducts (red color). For every duct the color stays mostly constant over the length of the duct, which means again that the backwall shift is constant over the whole length. However, at the first duct, it can be seen that there is a discontinuity at about the middle of the duct, which might be related to grouting state. This gap can as well be seen in the C-scans (Figure 72a). However, it is not clear why this effect occurs only locally at this exact position along the duct, since the grouting state remains the same over half the duct length.

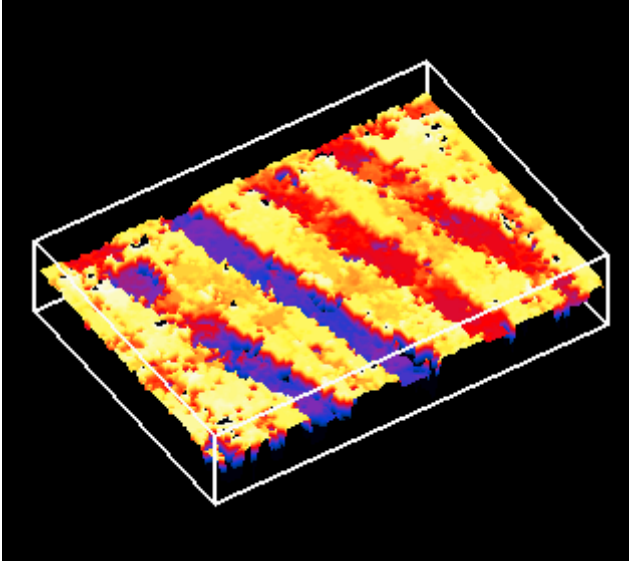


Figure 73: 3D Thickness plot obtained from impact-echo measurements taken from the front of the block.

Measurements taken from the back of the block

The impact-echo measurements from the back of the block were carried out along the same grid that was used on the front so that the results can be compared. The D-scans crossing the tendon ducts are given in Figure 74. The indication of the backwall appears to be shifted towards lower frequencies at the location of the duct, just as it was the case for the measurements taken from the front of the block. Again, the amount of this shift is different for the different ducts.

In the C-scans in Figure 75, and especially in the 3D thickness plot given in Figure 76, the distinctive feature at duct no. 1 that was already observed in the data taken from the front can be clearly identified. Furthermore, a similar feature occurs at duct no. 4, at about the same position along the duct. This can be seen as another indication that these discontinuities are related to the grouting state of the duct.

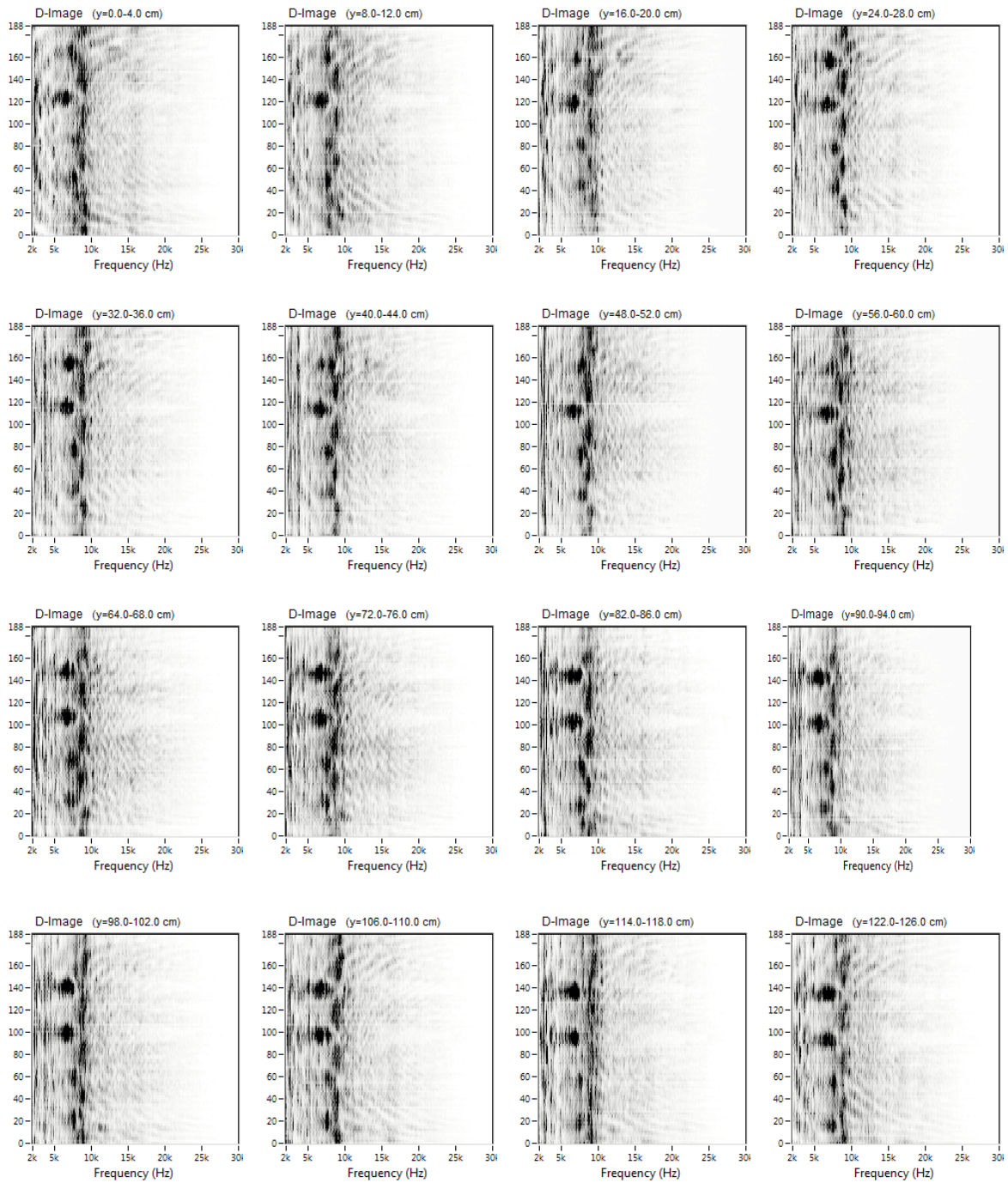


Figure 74: D-Scans crossing the tendon ducts. Measurements were taken from the back of the block. At the positions of the ducts a backwall shift is clearly visible.

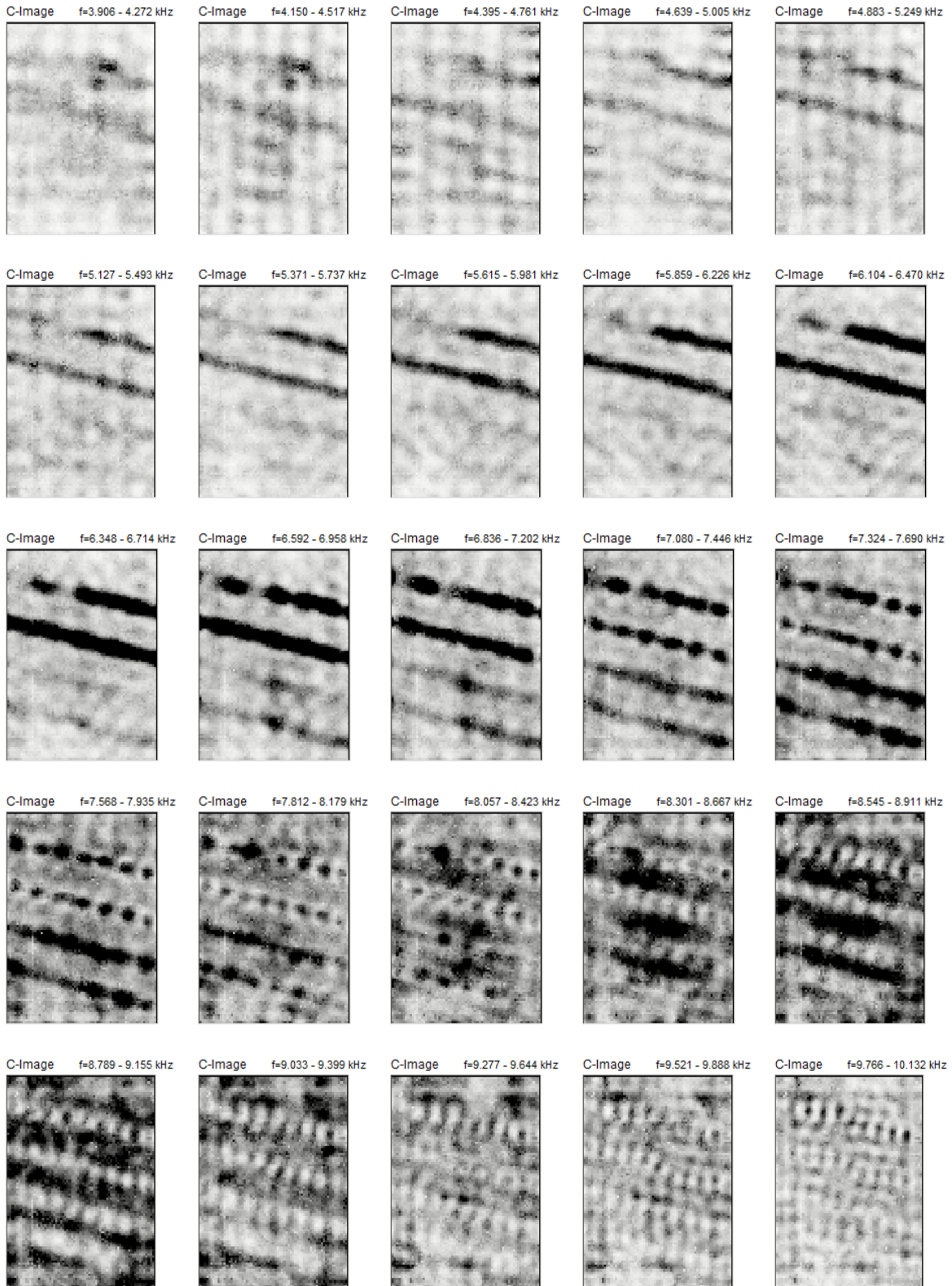


Figure 75a: C-Scans in the frequency range 4 kHz – 10 kHz. Measurements were taken from the back of the block. The given scans are projections obtained by averaging three consecutive scans, so that every image is an average over a frequency range of 0.366 kHz.



Figure 75b: C-Scans in the frequency range 10 kHz – 16 kHz. Measurements were taken from the back of the block. The given scans are projections obtained by averaging three consecutive scans, so that every image is an average over a frequency range of 0.366 kHz.

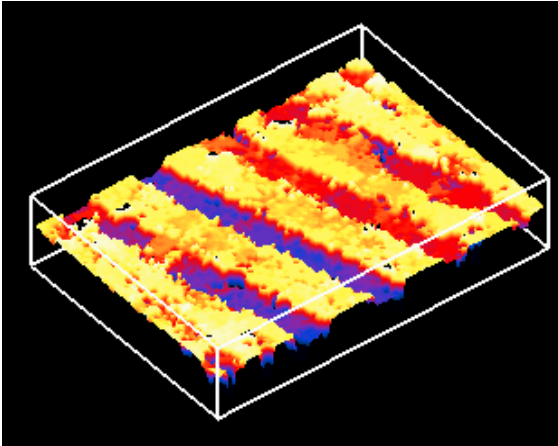


Figure 76: 3D Thickness plot obtained from impact-echo measurements taken from the back of the block.

5.5.2 Ultrasonic Echo Measurements

The ultrasonic echo measurements were carried out along the same grid (20 mm × 20 mm, 0.8” × 0.8”) as was used for the impact-echo measurements. The D-scans of the SAFT-HF signal are given in Figure 77a-b. In the D-scans, the indication of the duct can be identified so that the duct can be located in depth, which was not the case for the impact-echo measurements. In addition, the x- and y- location of the duct can also be seen as gaps in the backwall.

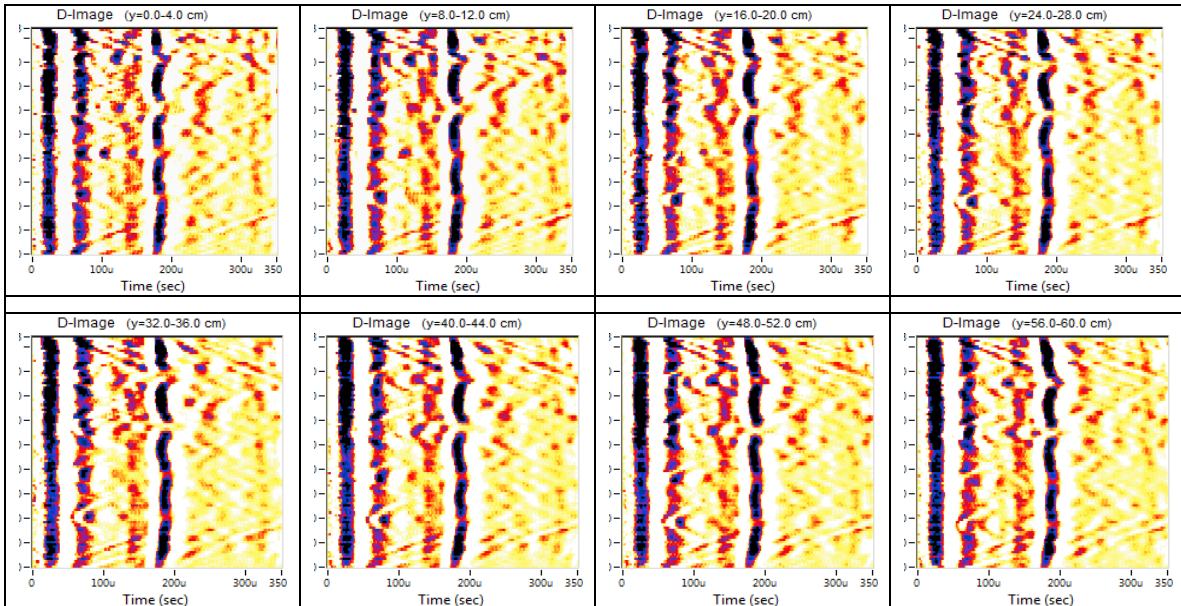


Figure 77a: Ultrasonic Echo D-Scans ranging from y = 0 cm to y = 60 cm, crossing the tendon ducts. Measurements were taken from the front of the block.

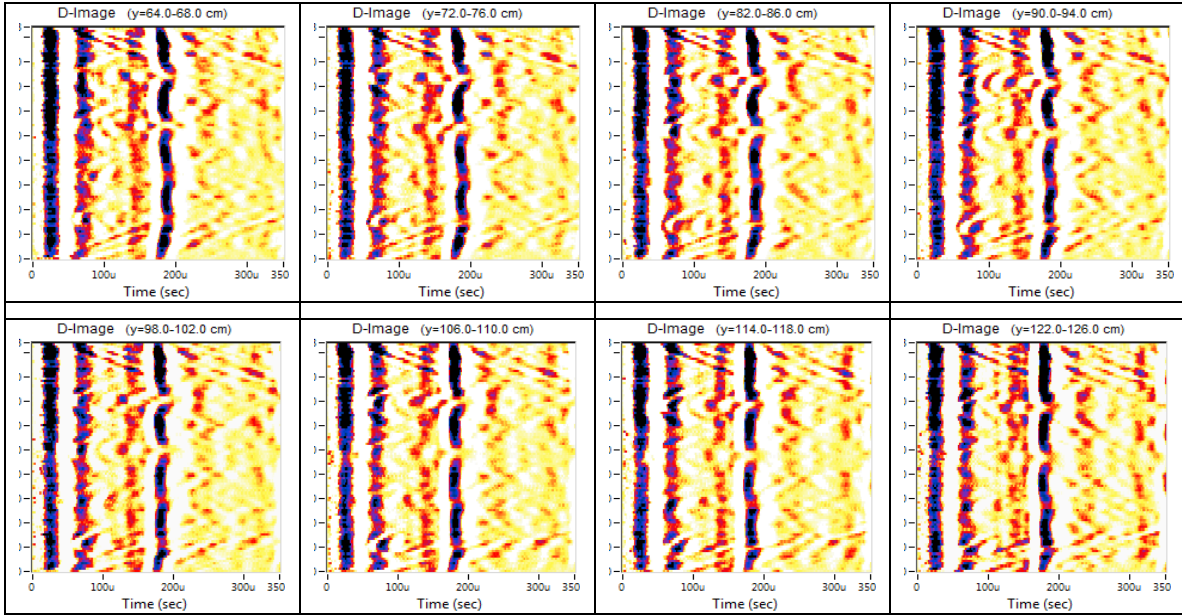


Figure 77b: Ultrasonic Echo D-Scans ranging from $y = 64$ cm to $y = 126$ cm, crossing the tendon ducts. Measurements were taken from the front of the block.

In the C-scans given in Figure 78a-e, the outlines of the ducts are clearly visible. Furthermore, the different sizes of the ducts can be identified as well, which again was not the case for the impact-echo measurements. Looking at duct no. 1, an irregularity can be observed at the position where the irregularities were seen in the impact-echo data as well, which might be an indication for the void inside the duct. This becomes even clearer in the 3D thickness plot given in Figure 79.

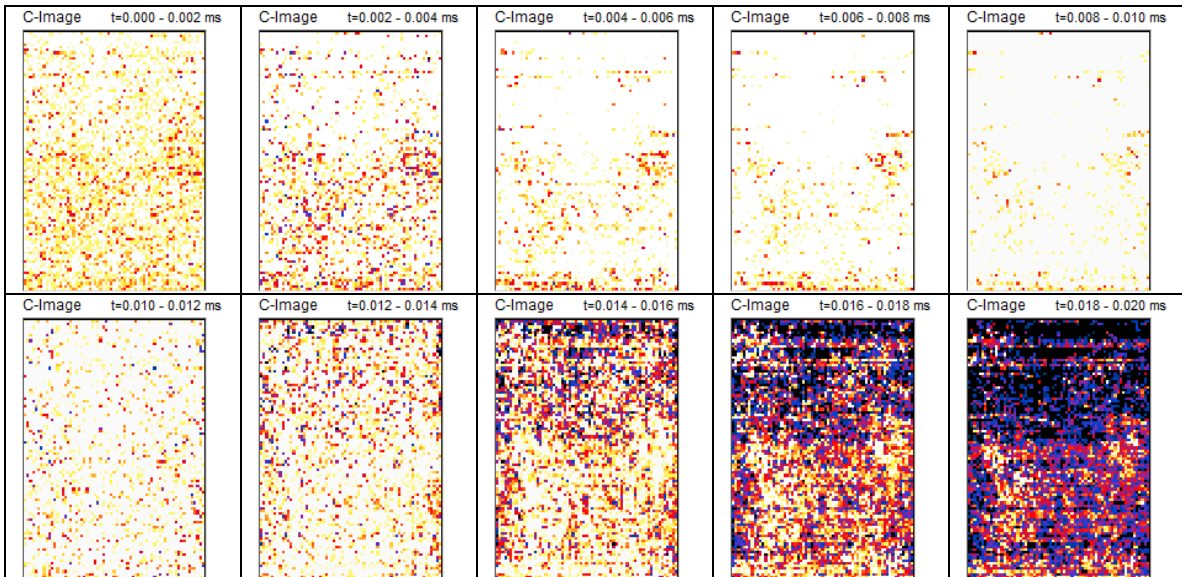


Figure 78a: C-Scans in the time range 0.000 ms – 0.020 ms. Measurements were taken from the front of block. The given scans are projections obtained by averaging three consecutive scans, so that every image is an average over a time range of 0.002 ms.

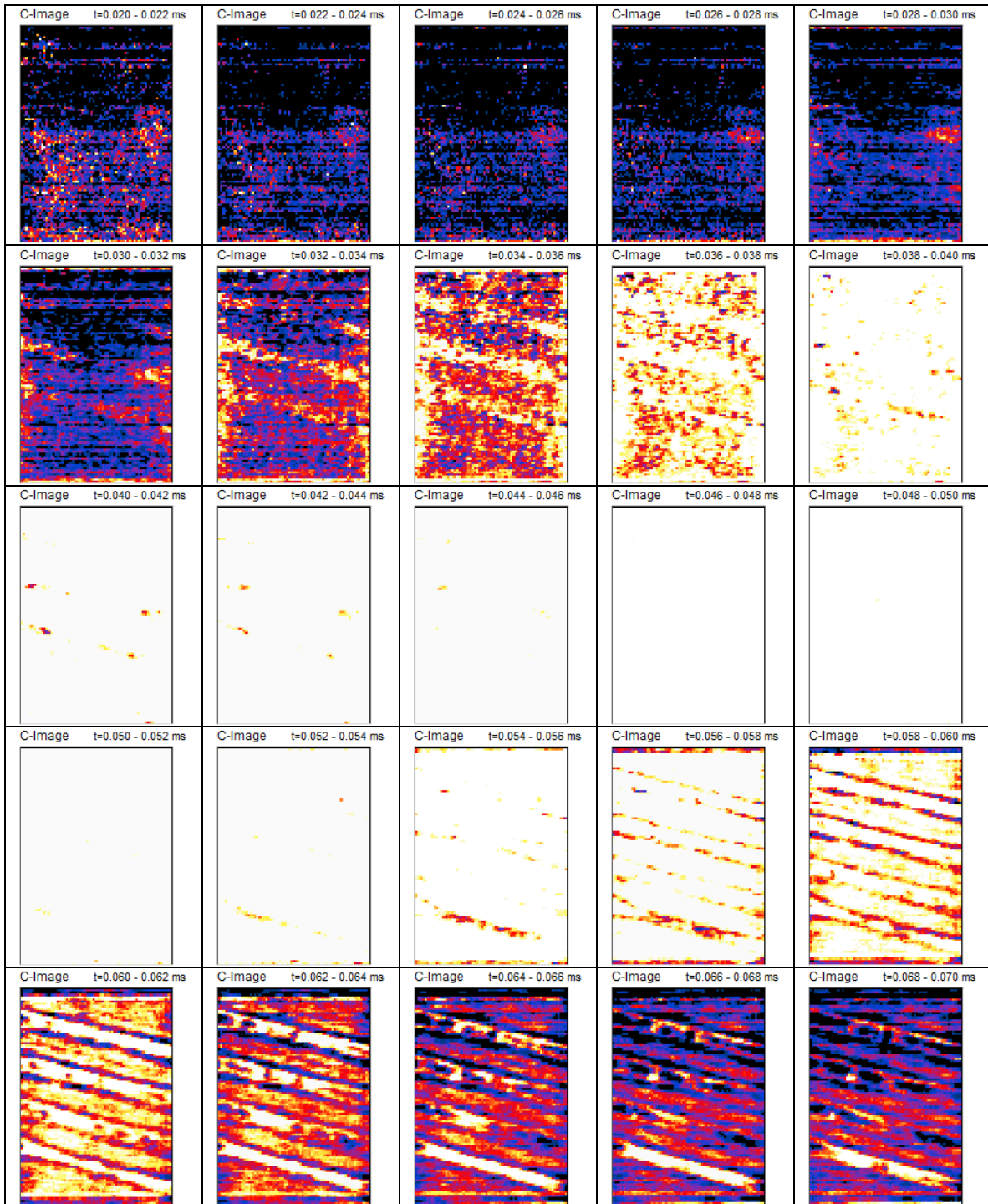


Figure 78b: C-Scans in the time range 0.020 ms – 0.070 ms. Measurements were taken from the front of block. The given scans are projections obtained by averaging three consecutive scans, so that every image is an average over a time range of 0.002 ms.

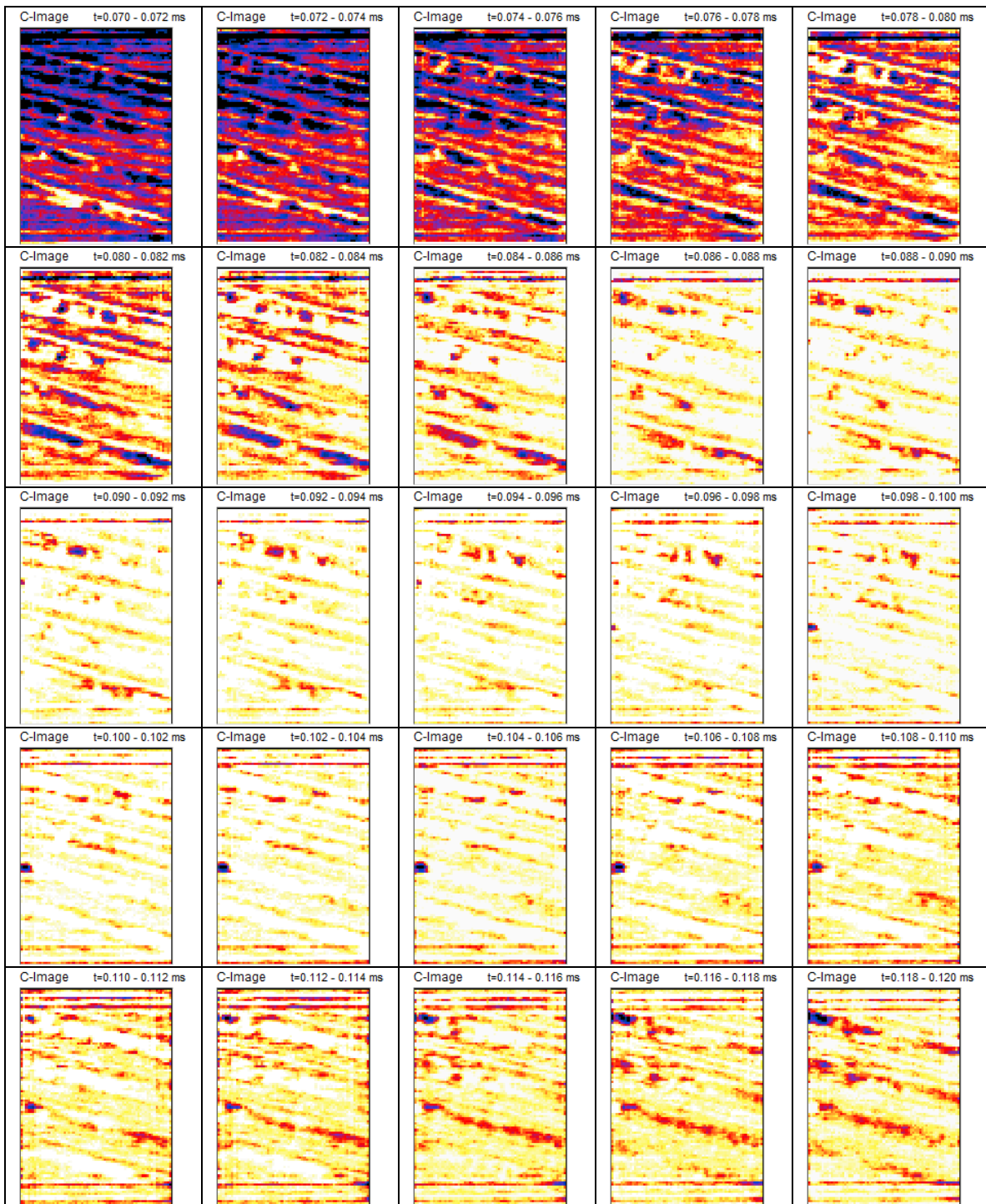


Figure 78c: C-Scans in the time range 0.070 ms – 0.120 ms. Measurements were taken from the front of block. The given scans are projections obtained by averaging three consecutive scans, so that every image is an average over a time range of 0.002 ms.

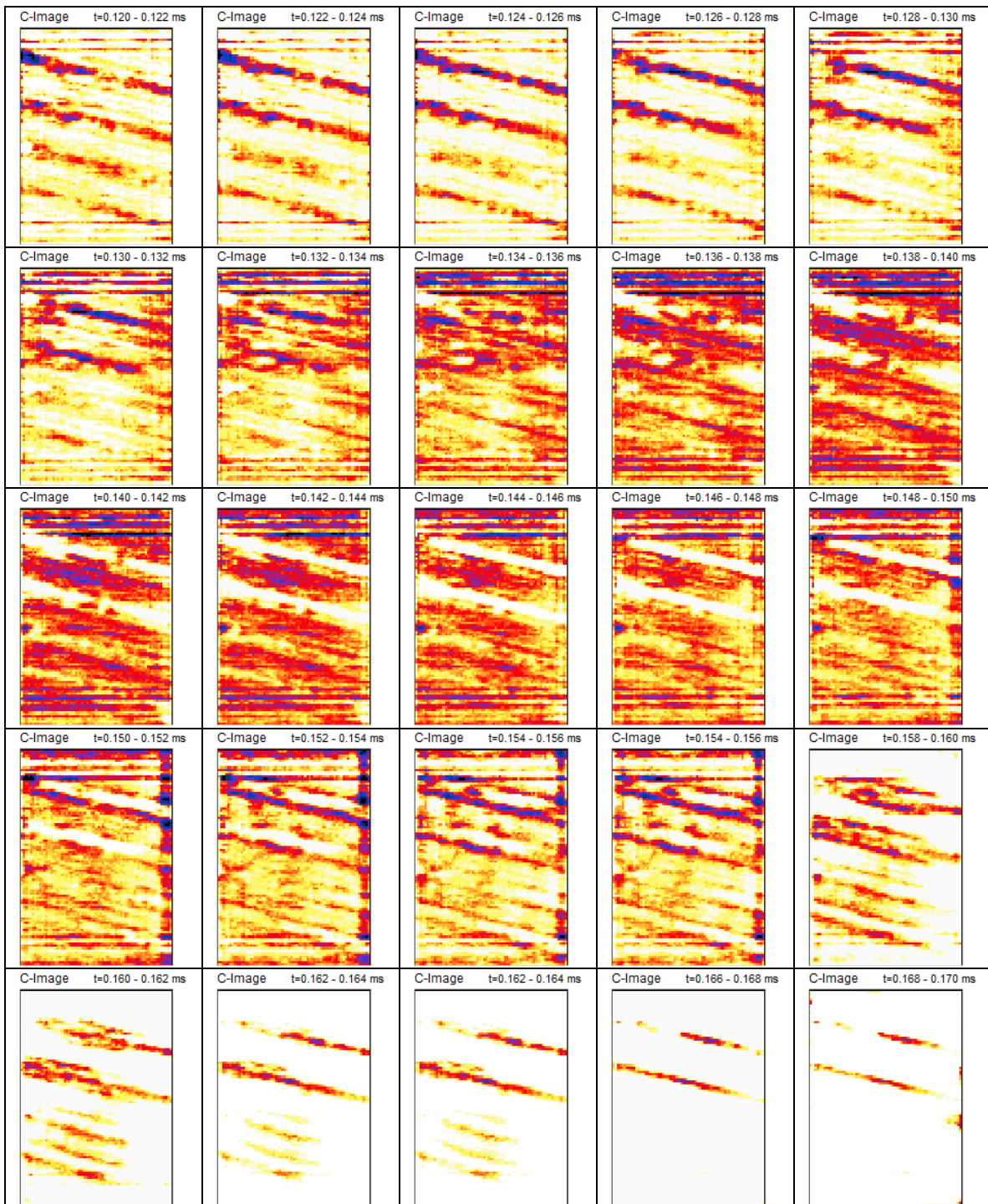


Figure 78d: C-Scans in the time range 0.120 ms – 0.170 ms. Measurements were taken from the front of block. The given scans are projections obtained by averaging three consecutive scans, so that every image is an average over a time range of 0.002 ms.

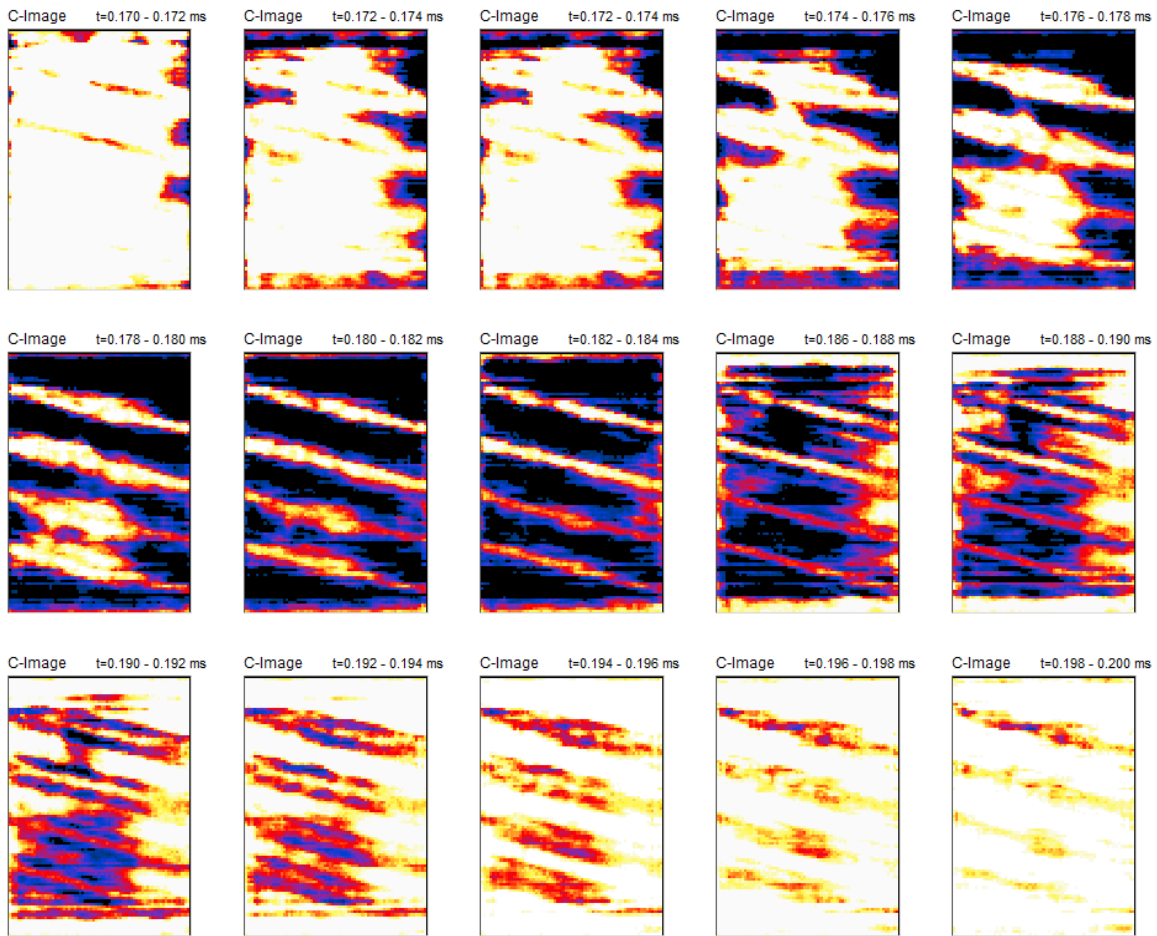


Figure 78e: C-Scans in the time range 0.170 ms – 0.200 ms. Measurements were taken from the front of block. The given scans are projections obtained by averaging three consecutive scans, so that every image is an average over a time range of 0.002 ms.

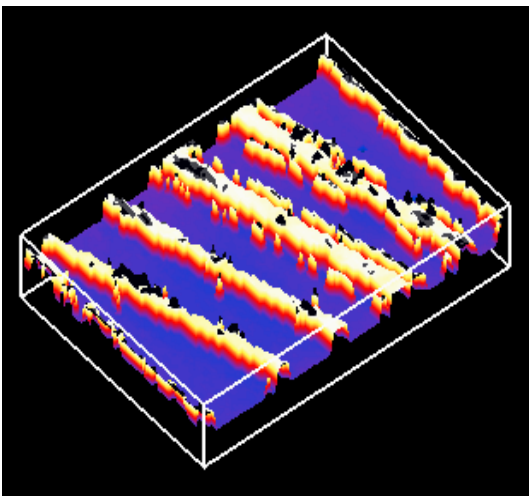


Figure 79: 3D Thickness plot obtained from ultrasonic echo measurements taken from the front of the block.

It is possible that the reason for the fully and partially grouted tendon ducts to provide images similar to the ones obtained from the ungrouted tendon ducts is a debonding issue. At the time of concrete placement, it was necessary to place the block formwork in a horizontal orientation (Figure 10) for casting. However, the block was moved to a vertical orientation subsequent to casting and curing for placement into the gantry frame for NDT testing. The movement of the block between placement and testing may have resulted in the debonding of the PT grout to the steel duct, resulting in a small layer of air which could have changed the acoustic impedance between the tendon duct and the grout, resulting in a reflection similar to those seen in a fully ungrouted duct. Preliminary tests during the construction of the block showed that the grout debonded from the steel duct with relative ease.

5.5.3 Covermeter Measurements

Covermeter measurements were carried out along scan lines in x-direction, crossing the tendon ducts. The distance between the scan lines was 4 cm (1.6”), and the distance between the consecutive points was 2 mm (0.08”). The results are shown in the depth plot in Figure 80.

The location of the ducts in the measurement area can be clearly determined. Since for localizing the ducts in depth, the diameter and wall thickness of the ducts as well as the amount of prestressing steel would have to be used as an input parameter, and the covermeter originally was not designed for this application, the depth values obtained can only be seen as a qualitative measure for the depth of the duct as well as the amount of prestressing steel in it, but cannot be quantitatively interpreted as the exact values. It can be seen that the ducts appear slightly wider than actual. This is because the probe registers the duct even when it is not exactly above the duct but slightly off, which is the same effect that causes the rebars to appear as hyperbolas.

For a practical case, this would mean that a covermeter could detect the position of tendon ducts, as long as the concrete cover is not too large and there is only very few reinforcement in front of it. Furthermore, in a case comparable to the one on this block, the tendon ducts would affect the measurement of the concrete cover of reinforcement steel, and would have to be taken into account. However, failing to take into account the effect of the tendon ducts would lead to an apparently smaller concrete cover of the reinforcement steel and would therefore be on the safe side.

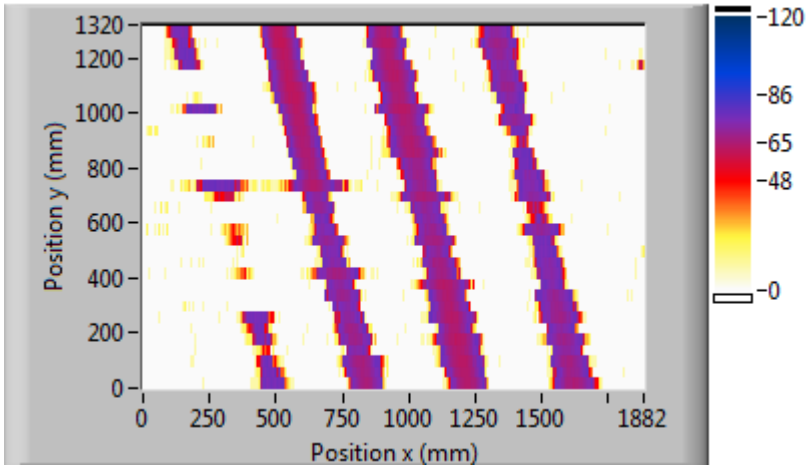


Figure 80: Covermeter measurements taken on Specimen 3 with the ducts. The covermeter is capable to detect the ducts.

5.6 Measurements on Specimen 3-1, Tendon Ducts

Because of its large dimensions, this specimen could not be brought in the test frame. It is planned to take the scanning system off the steel frame and bring it to this specimen to conduct automated measurements. In a first step, exemplary manual measurements were conducted with impact-echo (Figure 81).



Figure 81: Manual measurements taken on Specimen 3-1.

5.6.1 Impact-Echo Measurements

Manual impact-echo measurements were conducted along transversal scan lines as shown in Figure 82. The measurement grid was drawn on the surface of the specimen. The sensor was placed on the actual points of the grid while the steel ball, which was welded on a steel rod, was tapped on the concrete surface approximately 5 cm (2") away from the sensor.

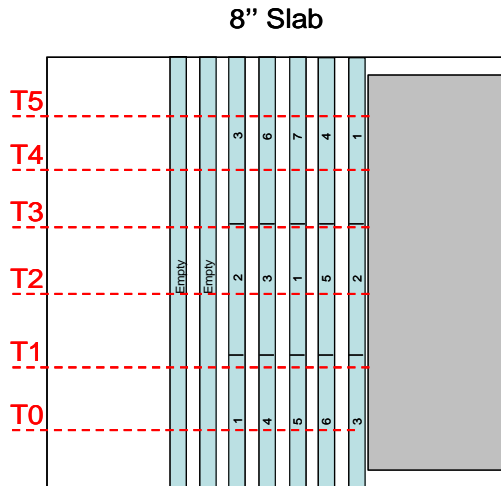


Figure 82: Overview of scan lines taken on Specimen 3-1.

The results are given in B-Scans in Figure 83. Since an eventual backwall shift can be seen best in a B-scan of a line crossing the duct, it was decided to use a relatively small point distance of 1.25 cm (0.5") in that direction and a spacing of approximately 30 cm (1') between the consecutive lines, which is just dense enough to cover the different sections along the ducts. In consequence, only the B-scans along the scan lines are shown in the following; C-scans or 3D thickness plots as they were shown above for the automated measurements would not reveal any additional information because of the relatively wide spacing between the lines compared to the dense spacing between the points along the scan lines.

Figure 83 gives the B-scans with (right) and without (left) an overlay of the locations of the amplitude maxima, which can be referred to as the indication of the backwall. In the solid area of the block without any ducts, the backwall reflection appears at a frequency of about 10 kHz, which matches the block thickness of 20 cm (8") and a longitudinal wave velocity of about 4000 m/s. In the area where the ducts are located, a significant drop in frequency can be seen, which is a typical effect and is used to locate tendon ducts as it was explained in chapter 1.3. Since the spacing between the ducts in the block is very small (less than the duct diameter), the individual ducts cannot be resolved, but appear as a band of reduced frequency in the B-scan. However, there are certain variations in the quantity of this backwall shift within the band. Although an exact allocation of the backwall shift to a specific void type might be an over-interpretation of the results, some general trends can be observed. The first two ducts are completely ungrouted. It can be seen that the backwall shift at the positions of these ducts stays mostly constant over all scan lines. Furthermore, these are also the locations where the maximum backwall shifts appear. In scan line T5 a significant area around duct no. 4 can be seen where the back wall shift is very low and almost the frequency of the solid part of the slab is reached. According to the information provided by the drawings, this is an area where the duct no. 4 is filled with grout. These observations are consistent with the theory that the apparent backwall shift is higher for an empty duct than for a duct that is filled with grout (and where the grout and the wall of the duct are bonded).

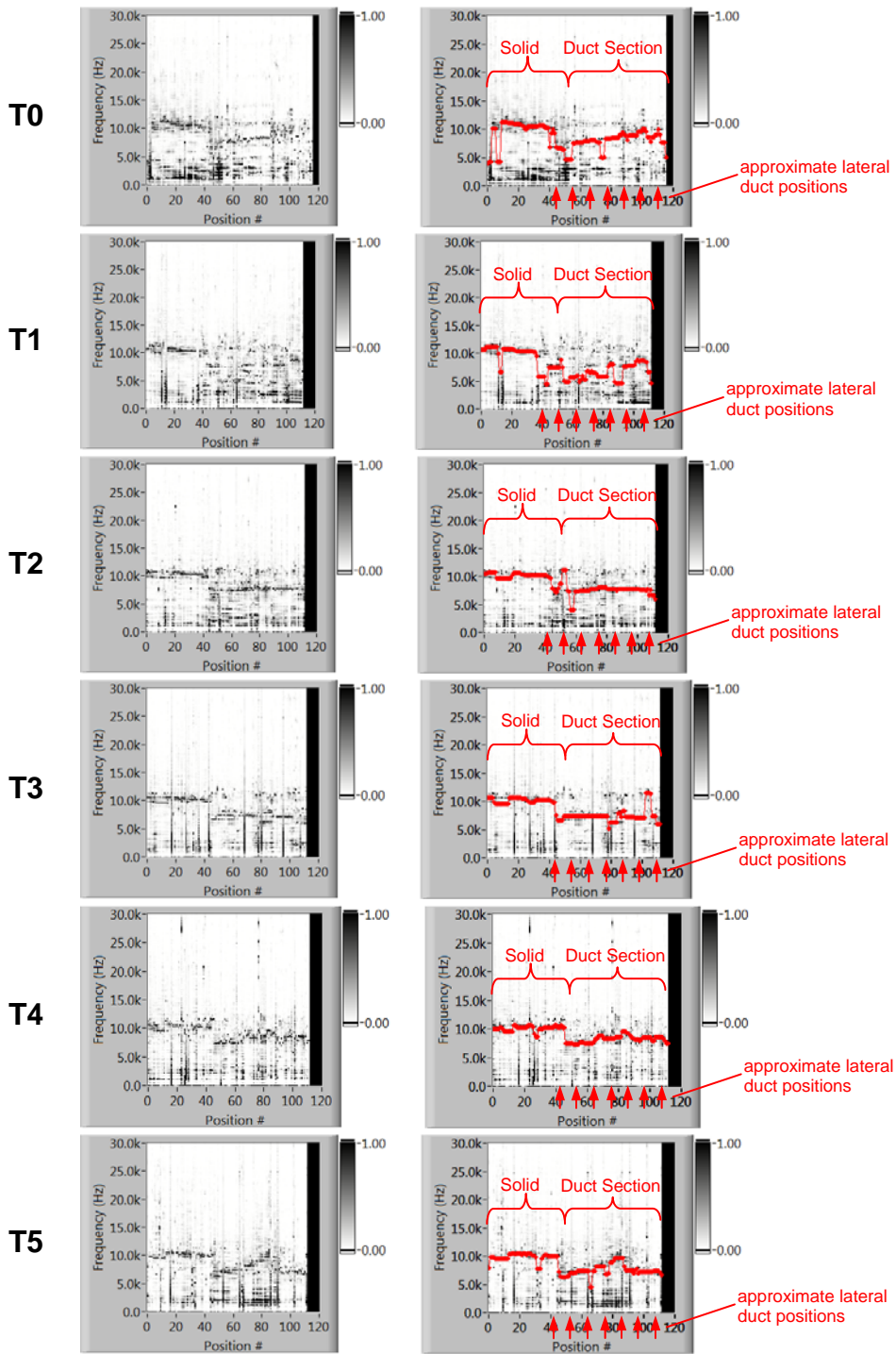


Figure 83: B-Scans collected from impact-echo measurements on Specimen 3-1 in transversal direction

5.7 Discussion

The following summarizes the experimental results reported in this chapter. The results make it clear that the different NDT methods are best suited for particular applications.

5.7.1 Localizing Reinforcement Steel in Concrete Components

Covermeter measurements are suitable for locating the top layer of reinforcement steel. The reinforcement block that was used for the performance demonstration served to study the capabilities as well as the limitations of this method and therefore has rebar arrangements that are more challenging than would be found in most practical cases. The covermeter provides good accuracy of about +/- 1 mm as long as the rebar spacing is wide (more than 7.5 cm, 3"), and there is only one layer of reinforcement. An additional layer of reinforcement crossing the layer that is being measured, however, will affect the accuracy. Naturally, the bigger the diameter and closer the spacing of the bars in the crossing layer, the more it will affect the measurement. A quantitative measure of this effect can only be given as a function of the rebar depths of the different layers as well as the rebar sizes and spacing. Based on the results obtained from the measurements on the reinforcement specimen used in this study, it can be said that the effect is rather small if the rebar spacing in the crossing layer is about 7.5 cm (3") or more. For a dense spacing of 2.5 cm (1"), the interfering effect will add to the amplitude of the signal obtained, which causes the cover measured to be about 1 cm (0.4") less than it actually is. In any case, the effect of additional rebar layers or adjacent rebars will only result in an underestimation of the cover and therefore always be on the safe side. Estimating the rebar diameter too large, however, can result in measured covers that are higher than the actual cover.

The results obtained from ultrasonic-echo in its application to locate reinforcement bars are promising. Especially in cases where reinforcement in larger depths or underneath the top layer is supposed to be located, this method will be the right choice. The application of the SAFT algorithm makes the rebars identifiable as point-like reflectors in the B-scan. The results obtained from this method provide more detailed information than is obtained from covermeter measurements. On the other hand, the image processing and interpretation requires a good amount of expertise from the personnel. The dense spacing, which is the key for the functionality of the SAFT algorithm, makes the measurements relatively time consuming. The combination of this method with covermeter measurements seems to be the way to go. Covermeter measurements can be conducted over a wider area, and ultrasonic measurements can then be conducted along selected scan lines where more detailed information is needed.

Because of their relatively large wavelength, the waves used in impact-echo measurements show hardly any interaction with the reinforcement steel, so that impact-echo should not be used for the detection of rebars. Instead, GPR should be considered to be used for this application also. The steel bars are perfect reflectors for the electromagnetic waves used in this method, and it can be expected that it will be able to detect reinforcement in several layers as long as the bar spacing is rather wide. However,

for spacing as dense as it can be found on the respective parts of the reinforcement block, it can be expected that the waves will be reflected completely and will not penetrate any further. Therefore, the decision of which method will be the best to use will always depend on the specific measurement problem and situation.

5.7.2 Thickness Measurements

The comparison of the results obtained from impact-echo and ultrasonic echo makes the advantages of the ultrasonic-echo quite obvious. While impact-echo suffers from various geometrical effects occurring at the edges of components with rather compact dimensions, this kind of effect hardly affects the ultrasonic-echo measurements. Although an experienced operator could identify geometry effects in the impact-echo results and pick the adequate indications manually, it becomes clear that the analysis is definitely easier, more reliable and straight forward for the ultrasonic-echo measurements. This obviously applies to measurement situations that are comparable with the one given here in the case of the thickness block, i.e., thicknesses ranging from about 17.5 cm to 50 cm (7'' to 20''), and the different areas being rather compact in their lateral dimensions. Impact-echo can definitely provide much better results when measurements are conducted on components with wide lateral extensions. Due to the long wavelength and the high energy created by the impact, impact-echo can also be applied to measure relatively large thicknesses as long as a transducer is used that is designed for the low frequencies. However, for the thickness range covered by the thickness block, ultrasonic-echo appears to be the method to go with.

As this block is not reinforced, GPR would as well be able to provide good results. In practical cases though, the accuracy of thickness measurements conducted with GPR is known to be affected by the reinforcement. A big advantage of the GPR method compared with ultrasonic as well as impact-echo is that it is a non-contact measurement, which results in very high scan speeds.

Although the surface of the thickness block is relatively smooth, there are some slight changes in the actual thickness within an estimated range of about 1 cm (0.4''). For a quantitative evaluation of the accuracy of the measured thicknesses, it would therefore be good to know the exact actual thickness at every measurement position along the scan area. It is expected that the application of the laser profilometer in the future will make it possible to obtain the necessary information for the exact quantitative evaluation of the results.

5.7.3 Tendon Duct Inspections

With ultrasonic-echo it was possible to locate the ducts in depth and obtain a good relative estimate of their diameters. With impact-echo the lateral position of the ducts can be determined based on an appearing backwall shift towards lower frequencies at the location of a duct.

Knowing that the detection of voids in the grout of the ducts is a highly challenging testing problem, it was still the hope to be able to identify the grouted, ungrouted and partially grouted parts of the ducts in the tendon duct block based on the measurement results. Unfortunately, this was not possible. It can be assumed that the grout is just not bonded to the wall of the duct (anymore), so that there is a thin air gap between the grout and the duct wall. Since this air gap is an acoustical interface that causes a total reflection of the acoustic waves (both, ultrasonic-echo and impact-echo), just as it is the case at the air voids at the ungrouted parts of the duct, it is not possible to distinguish between the grouted and ungrouted parts anymore, and in consequence not possible to detect the actual voids.

Although the dense spacing of the ducts in the additional tendon duct block 3-1 makes them appear as a frequency shifted band and not as individual ducts, the effects occurring within this band are mostly consistent with the theory that an empty duct causes a larger frequency shift than a fully grouted duct.

For future studies it should be considered to build another block and focus especially on the bond between the grout and the duct. For example, to avoid moving the block in the laboratory and cause the grout to debond, the block could be built with empty ducts at first, then brought in the test frame where the grout is filled in. After the grout is hardened, the block can be tested by the different methods.

6 Determining Elastic Parameters Using Acoustic NDT Methods

To gain information on the elastic behavior and structural integrity of a bridge structure, a commonly used method is to load the bridge by a truck load and measure the strain responses of the bridge. The effort for such a test is relatively high. For the interpretation of the data obtained from load tests, some elastic parameters still have to be estimated.

To support these tests or even reduce the number of tests that is necessary to obtain the particular information on the behavior of the bridge, it would help if a more exact estimate of the elastic parameters could be provided by complimentary methods. In this project it was investigated how far this information could be obtained from NDT techniques. There have been previous studies ([36][37][38][40]) in which various material parameters were determined based on the wave speed of ultrasound waves.

6.1 Theory

Since the elastic wave velocity of an ultrasonic wave depends on the elastic parameters, it can as well be used to determine a certain parameter if the other parameters are known. The velocity of an ultrasonic longitudinal wave can be determined as [24]:

$$c_L = \sqrt{\frac{E}{\rho} * \frac{1-\nu}{(1+\nu)(1-2\nu)}} \quad (2)$$

and the shear wave velocity as:

$$c_S = \sqrt{\frac{E}{\rho} * \frac{1}{2(1+\nu)}} \quad (3)$$

With:

c_L : longitudinal wave velocity
E: Young's modulus of elasticity
 ρ : material density
 ν : Poisson's ratio.

The two equations can as well be written as [24]:

$$c_S = c_L * \sqrt{\frac{1-2\nu}{2(1-\nu)}} \quad (4)$$

or solved for ν as a function of c_S and c_L :

$$\nu = \frac{\frac{1}{2} - \left(\frac{c_s}{c_L}\right)^2}{1 - \left(\frac{c_s}{c_L}\right)^2}, \quad (5)$$

which means that Poisson's ration ν can be obtained if c_s and c_L are known. Since impact-echo is based on longitudinal waves, c_L can be obtained from it based on the *impact-echo equation* [9]:

$$d = \frac{c_L}{2f}, \quad (6)$$

With:

d: reflector depth

f: the measured frequency

which solved for c_L gives:

$$c_L = \frac{d}{2f}. \quad (7)$$

The shear wave velocity c_s is obtained in ultrasonic echo measurements using shear wave transducers as was the case for the ultrasonic transducer (Eyecon) used in this project:

$$c_s = \frac{2d}{t}, \quad (8)$$

With:

d: reflector depth

t: time of flight.

Furthermore, in cases where the exact thickness of the test object is not known, ν can still be determined as:

$$\nu = \frac{t_s^2 - 2\left(\frac{1}{f}\right)^2}{2\left(t_s^2 - \left(\frac{1}{f}\right)^2\right)}, \quad (9)$$

With:

t_s : time of flight measured with shear wave ultrasound

f : frequency in the spectrum obtained from impact-echo measurement.

The combination of impact-echo and ultrasonic echo will therefore be able to provide Poisson's ratio.

To determine the modulus of elasticity as well as the shear modulus G , Equation 2 can be written as:

$$E = 4\rho \frac{3/4c_L^2 - c_s^2}{\left(\frac{c_L}{c_s}\right) - 1} \quad (10)$$

as well as

$$G = \rho \cdot c_s^2 \quad (11)$$

This means that with c_s and c_L measured, E as well as G can be determined if ρ is known, e.g., from coring, documents on the mix or even just estimations.

6.2 Demonstration

This theory will be applied to the data collected on Specimen 0, as this is a solid block with no reinforcement, voids or other objects that might affect the velocity measured.

As described in chapter 5.1, a longitudinal wave velocity of $c_L = 4519$ m/s was determined from impact-echo, and a shear wave velocity of $c_s = 2712$ m/s was determined from the ultrasonic-echo measurements using shear wave transducers. From this the Poisson's ratio is calculated as:

$$\nu = \frac{\frac{1}{2} - \left(\frac{c_s}{c_L}\right)^2}{1 - \left(\frac{c_s}{c_L}\right)^2} = \frac{\frac{1}{2} - \left(\frac{2712\text{m/s}}{4519\text{m/s}}\right)^2}{1 - \left(\frac{2712\text{m/s}}{4519\text{m/s}}\right)^2} = 0.23.$$

From conventional Poisson's ratio measurements conducted on samples of the same batch, a Poisson's ratio of $\nu = 0.26$ was obtained. The difference might be caused by certain inaccuracies in the process of determining c_L and c_s , and geometry effects

affecting the measurements. A slight difference in the wave velocity can cause a significant change in the value obtained for Poisson's ratio.

Assuming that the density of the concrete is known (determined to $143.2 \text{ lb/ft}^3 = 2294 \text{ kg/m}^3$), the modulus of elasticity can be determined:

$$E = 4\rho \frac{3/4c_L^2 - c_s^2}{\left(\frac{c_L}{c_s}\right)^2 - 1} = 4 * 2294 * \frac{\text{kg}}{\text{m}^3} * \frac{\frac{3}{4}\left(4519\frac{\text{m}}{\text{s}}\right)^2 - \left(2712\frac{\text{m}}{\text{s}}\right)^2}{\left(\frac{4519\frac{\text{m}}{\text{s}}}{2712\frac{\text{m}}{\text{s}}}\right)^2 - 1} * \frac{\text{m}^2}{1000000\text{mm}^2}$$

$$\Rightarrow E = \underline{\underline{41119.5 \frac{\text{N}}{\text{mm}^2}}}$$

The modulus of elasticity obtained from a test in the laboratory measured 43299 N/mm^2 .

Furthermore, the shear modulus G can be calculated as:

$$G = \rho \cdot c_s^2 = 2294 \frac{\text{kg}}{\text{m}^3} * \left(2712\frac{\text{m}}{\text{s}}\right)^2 = \underline{\underline{16872 \frac{\text{N}}{\text{mm}^2}}}.$$

6.3 Discussion

It has been explained and demonstrated how the Poisson's ratio, elastic modulus and shear modulus can be determined by using a combination of ultrasonic-echo and impact-echo measurements. In the example given, the results provided an estimate of the values that were determined in laboratory tests, however, still showed tolerances that have to be taken into account. To get a better idea of the performance of the NDT methods in this particular application, further experiments will be necessary. One of the reasons why it will be challenging to obtain exact values from this procedure is that it strongly depends on the accuracy with which the wave velocities have been determined. This requires the thickness of the test object at the measurement position to be known as exactly as possible, because the wave velocities are determined based on the thickness. In most practical cases, this will require coring at the measurement position. Another way to determine the wave velocities would be to measure them at the surface with two sensors of the same kind, one transmitting and the other one receiving. However, it is known that the wave velocities at the surface of a concrete object can vary from those inside the object, thus resulting in certain deviations as well. It also has to be taken into account that the presence of reinforcement, tendon ducts or voids might reduce the wave velocities

being measured. More experiments will provide better statistics on the performance of the different techniques. Since the conventional laboratory tests to determine the elastic parameters serve as a reference for results obtained from the NDT measurements, it might be necessary to check the accuracy of these tests in more detail as well. When used thoroughly, NDT has potential to support or verify the findings from load testing experiments or to even replace them.

7 Closure

7.1 *Summary of Findings*

The Florida Department of Transportation (FDOT) would like to implement nondestructive test and evaluation (NDT/NDE) technologies to assess quality of concrete constructed in the field for new construction, and to assess the structural details of older and often unknown existing structures. Toward this aim, the primary objective of the project was to design, construct, and implement a facility for calibrating and validating methodologies for the NDT/NDE of structural concrete materials and members.

Four concrete test blocks have been designed and built in which specific testing problems were implemented to investigate them under defined conditions in the laboratory. Four major testing problems/aspects of NDT were included, namely: 1) locating reinforcing steel in concrete components, 2) measuring thicknesses and locating irregularities, 3) tendon duct inspection, and 4) application of NDT to determine elastic parameters. The specimens were designed to challenge NDT techniques, and serve to demonstrate their capabilities as well as their limitations.

An automated test frame has been designed, built, and implemented, and a user-friendly software platform for scanner control, data acquisition with different sensors, real-time imaging and data analysis has been developed and successfully applied in the project.

Automated measurements were taken in scanning mode with impact-echo, ultrasonic echo, and covermeter on the four concrete test specimens. GPR equipment has been procured but will require extra effort to be operated on the scanner. Based upon the experimental results presented herein, the key findings are summarized as follows:

- Covermeter measurements on the specimen with reinforcement steel clearly demonstrated the potential of this method, but also showed some limitations.
- Complementary ultrasonic-echo measurements in combination with the synthetic aperture focusing technique (SAFT) analysis showed the potential of this method to resolve reinforcement in cases where it cannot be resolved by the covermeter.
- Measurements conducted on the specimen with varying thicknesses demonstrated the capabilities of especially ultrasonic-echo.
- The tendon ducts in the tendon duct specimen were located in 2D by impact-echo and in 3D by ultrasonic echo. Even the covermeter measurements carried out on that block showed a clear image of the ducts. A differentiation between the empty, grouted and half-grouted areas was questionable at best, but mostly impossible. A reason for that is assumed to be the lack of bond between the grout and the duct, maybe caused in the process of having to move the block in the laboratory.

- Two additional tendon duct specimens were provided by the FDOT Structures Office in Tallahassee. Manual impact-echo measurements were taken on block 3-1, which has tendon ducts with various kinds of voids in the grout. The results were consistent with the theory that an empty duct causes a higher apparent shift in the backwall than a filled duct, although the ducts could not be individually identified.
- The theory for determining elastic parameters of concrete has been presented and demonstrated in an example. Based on the example, it is understood that this method can provide a good estimate of these important mechanical properties.
- Modification or adaption of the GPR device will be necessary to operate it in combination with the scanner system.

7.2 Conclusions

Based upon the findings of this study, the primary conclusions are as follows:

- Overall, a first-stage NDT validation facility has been established, and the system has been demonstrated to work precisely and reliably.
- The system implements automated scanning measurements and data analysis techniques with NDT hardware to produce an advanced sensing system for assessment of structural concrete materials and members.
- The concept for the system design follows the scanning systems pioneered at BAM, Berlin, Germany, but it provides a unique, one-of-a-kind capability in the United States.

7.3 Recommendations

Based upon the findings and conclusions documented herein, the following recommendations for further investigation are presented:

- **Quality Assurance/Quality Control (QA/QC):** It is hoped that the positive results documented herein on the application of automated NDT to assess structural concrete will inspire continued and increased application in real infrastructure projects and problems. For example, automated NDT should one day be able to serve as the primary source for inspection and acceptance of infrastructure facilities. However, to realize this vision, the work documented herein will not be sufficient, but can serve as a first step in this direction. Certainly more extensive experimental testing must be conducted to establish the detailed capabilities of the techniques, and to establish a sufficient statistical database from which appropriate acceptance criteria can be developed.

- **Field Testing:** Since the scanners can be easily taken off the frame to move them on a truck, the system is well suited to be applied in the field. As long as the surfaces of the components to be tested provide at least a minimum smoothness that is needed for the coupling of the sensors, to mount the scanner and to position the sensors, impact-echo, ultrasonic-echo and covermeter measurements can be conducted just as it was demonstrated in the laboratory. It is recommended that pilot field studies be conducted to shake-down use of the system for field applications.
- **Tendon Ducts:** The tendon duct experiments documented herein were only partially successful. However, there are enough clear indications from the tests on the two blocks to suggest that more complete success can be expected from proper application of NDT, and further trials should be conducted to investigate and develop techniques for this important area of structural concrete assessment, including the suggestions discussed in Chapter 5.7.3.
- **Ground Penetrating Radar (GPR):** The application of GPR will add another capable method to the assortment of NDT techniques, and should prove useful in locating reinforcement steel and tendon ducts, and in determining concrete thickness. Since GPR measurements can be conducted with a high scan speed, it can also be used to define the measurement areas on which other NDT methods can be applied for a more in-depth investigation. For example, tendon ducts can be first located by GPR, so that measurements with ultrasonic-echo to examine the grout inside the duct will only have to be conducted along the duct and not along the whole measurement area, thus reducing the time for the inspection.
- **Profilometer:** The laser profilometer will provide valuable information especially for field applications since it will be able to register surface cracks and will be able to measure the surface texture and profile along the measurement area, which can be used in the interpretation of the NDT results. The surface profile can as well be used during the measurement to prevent the sensor from getting damaged at potential obstacles on the surface. It is recommended that this system be implemented in the scanner for future measurement applications.
- **Data Fusion:** As provided via example in the GPR section above, the more general subject of data fusion and integration should be more fully investigated and developed. As with the GPR example, testing efficiencies are expected with the coupling of multiple methods, each working on an aspect of the overall problem for which the particular method is best suited. Also, combinations of differing techniques may reveal details of the problem not available from the results of a single technique applied alone.

8 References

- [1] Streicher, D., Algernon, D., Wöstmann, J., Behrens, M. and H. Wiggenhauser: Automated NDE of post-tensioned concrete bridges using imaging echo methods. Proceedings of the European Conference on NDT 2006, CD, (2006).
- [2] Helmerich, R., Niederleithinger, E. and H. Wiggenhauser: Toolbox with nondestructive testing methods for condition assessment of railway bridges. Transportation Research Record, Volume 1943, pp. 65-73, (2006).
- [3] Wiggenhauser, H.: Advanced NDT methods for quality assurance of concrete structures. Proceedings of the NDTCE'09 conference, Nantes, CD, (2009).
- [4] ACSYS A1220: www.acsys.ru, (2006).
- [5] Schickert, M., Krause, M. and W. Mueller: Ultrasonic imaging of concrete elements using reconstruction by synthetic aperture focussing technique. Journal of Materials in Civil Engineering, Vol. 15, No. 3, June 1, (2003).
- [6] Mayer, K., Marklein, R., Langenberg, K. J. and T. Kreutter: Three-dimensional imaging system based on Fourier transform synthetic aperture focusing technique. Ultrasonics, 28, pp. 241-255, (1990).
- [7] Krause, M., Milman, B., Schickert, M. and K. Mayer: Investigation of tendon ducts by means of ultrasonic echo methods: A comparative study. Proceedings of the European Conference on Nondestructive Testing 2006, Berlin, (2006).
- [8] Krause, M., Wiggenhauser, H., Mueller, W. and V. Schmitz: NDE of tendon ducts in concrete using 3D-SAFT. Proceedings of the MRS Fall Meeting 1997, Vol. 503, (1997).
- [9] Sansalone, M. und B. Streett: Impact-Echo. Jersey Shore, Bullbrier Press, (1997).
- [10] Schubert, F. and B. Koehler: Ten lectures on impact-echo. Journal for Nondestructive Evaluation, Vol. 27, pp. 5-21, (2008).
- [11] Tinkey, Y., Olson, L.D., Bedon, R. and C. Lieberle: Impact-echo scanning technology for internal grout condition evaluation in post-tensioned bridge ducts. International Symposium for Non-Destructive-Testing in Civil Engineering, Berlin, September 16-19, (2003).
- [12] Tinkey, Y., Olson, L.D. and H. Wiggenhauser: Impact echo scanning for discontinuity detection and imaging in post-tensioned concrete bridges and other structures. Materials Evaluation, American Society Nondestructive Testing, Vol. 63, No. 1, January, pp.64-69, (2005).
- [13] Beutel, R., Reinhardt, H.W., Grosse, C.U., Glaubitt, A., Krause, M., Maeierhofer, C., Algernon, D., Wiggenhauser, H. and M. Schickert: Performance demonstration of non-destructive testing methods. Proceedings of the European Conference on Nondestructive Testing 2006, Berlin, (2006).

- [14] Abraham, O. and P. Cote: Impact-echo thickness frequency profiles for detection of voids in tendon ducts. *Structural Journal*, Vol. 99, Issue 3, pp. 239-247, (2002).
- [15] Proverbio, E., Epasto, G. and V. Venturi: Il metodo dell'impact-echo per la valutazione dello stato di degrado di strutture in c.a.p. *Cemento & calcestruzzo*, April, pp. 167-174, (2007).
- [16] Colla, C.: Scanning impact-echo NDE of post-tensioning ducts in concrete bridge beam. *SMT Structural Materials Technology: NDE/NDT for Highways and Bridge Topical*, S. Alampalli and G. Washer (Ed.), Cincinnati, OH, September 10-13, ASNT, Columbus, pp. 307-312, (2002).
- [17] Algernon, D.: Impact-echo data analysis based on duration and bandwidth of signal components. *Transportation Research Records (TRR): Journal of the Transportation Research Board*, No. 2050, Transportation Research Board of the National Academies, Washington, D. C., pp. 127-133, (2008).
- [18] Abraham, O., Leonard, Ch., Cote, Ph. and B. Piwakowski: Time frequency analysis of impact-echo signals: numerical modeling and experimental validation. *ACI Materials Journal*, Vol. 97, No. 6, pp. 645-657, (2000).
- [19] Flohrer, C.: Messung der betondeckung und ortung der bewehrung. *Fachtagung Bauwerksdiagnose 1999, DGZFP Berichtsband*, Vol. 66-CD, (1999).
- [20] Proceq Manual for the Profometer 5+. Proceq SA, Switzerland.
- [21] Annan, A. P., Cosway, S. W. and T. DeSouza: Application of GPR to map concrete to delineate embedded structural elements and defects. *International Society for Optical Engineering (SPIE) Proceedings*, 4758, 359–364 (2002).
- [22] Derobert, X., Aubagnac, C. and O. Abraham: Comparison of NDT techniques on a posttensioned beam before its autopsy. *NDT&E International*, Vol. 35, pp 541–548, (2002).
- [23] Leuze Electronic: www.leuze.de, (2009).
- [24] Krautkraemer, J. and Krautkraemer, H.: *Ultrasonic testing of materials*. 4th Ed., Springer, Berlin, (1990).
- [25] Fatemi, M. and A.C. Kak: Ultrasonic B-scan imaging theory of image formation and a technique for restoration. *Ultrasonic Imaging*, Vol. 2, No. 1, pp. 1-47, (1980).
- [26] Wiggenhauser, H.: Homemade-Datenanalyse und –visualisierung mit freier Software. *iX Magazin für professionelle Informationstechnik*, Vol. 12, pp. 96-99, (2003).
- [27] Colla, C., Schneider G. and H. Wiggenhauser: Automated impact-echo: method improvements via 2- and 3-D imaging of concrete elements, *SFR'99*, London, pp. 1-11, (1999).
- [28] Tinkey, Y, Olson, L. and H. Wiggenhauser: Impact-echo scanning for discontinuity detection and imaging in post-tensioned concrete bridges and other structures. *Materials Evaluation*, Vol. 63, No. 1, pp. 64-69, (2005).

- [29] Lausch, R., Wiggenhauser, H. und F. Schubert: Geometrieeffekte und Hüllrohrortung bei der Impact-Echo-Prüfung von Betonbauteilen – Experimentelle und modelltheoretische Ergebnisse. DGZfP Jahrestagung 06-08, Mai 2002 in Weimar, DGZfP-Berichtsband BB-80-CD, Plakat 34, (2002).
- [30] Köhler, B., Schubert, F., Algernon, D., Gardei, A., Mielentz, F. and M. Krause.: Experimental study of elastic waves in concrete for NDE in civil engineering. 31st Annual Review of Progress in Quantitative Nondestructive Evaluation (QNDE), Canada, (2004).
- [31] Algernon, D., Wiggenhauser, H. and F. Schubert: A new approach for the investigation of geometry effects in impact-echo measurements – experimental results and numerical simulations. Proceedings of the 9th ECNDT, June 25-29, Berlin, CD-ROM, (2006).
- [32] Algernon, D., Schubert, F. and H. Wiggenhauser: Impact-echo: experimental and theoretical study of the acoustic wave propagation. Proceedings of the 2006 Conference of NDE in Civil Engineering, St. Louis, (2006).
- [33] Biot, M.A.: Theory of propagation of elastic waves in a fluid saturated porous solid. J. Acoust. Soc. Am., Vol. 28, pp. 168-191, (1956).
- [34] Ruck, H-J., Grosse, C.U. and H.W. Reinhardt: Automatisierung bei der Qualitätssicherung von Frischbeton mit Ultraschall. Virtuelle instrumente in der Praxis, R. Jamal and H. Jaschinski, Ed., Proceedings of VIP 2001, Munich, pp. 26-31, (2001).
- [35] Ozturk, T., Rapoport, J., Popovics, J.S. and S.P. Shah: Monitoring the setting and hardening of cement based materials with ultrasound. Concrete Science and Engineering, Vol. 1, No. 2, pp. 83-91, (1999).
- [36] Gulzow, A., Gsell, D. and R. Steiger: Non-destructive evaluation of elastic parameters of square-shaped cross-laminated solid wood panels, built up symmetrically with 3 layers. European Journal of Wood and Wood Products, Vol. 66, No. 1, pp. 19-37, (2008).
- [37] Ulrich, T.J. and K. R. Mc Call: Determination of elastic moduli of rock samples using resonant ultrasound spectroscopy. J. Acoust. Soc. Am., Vol. 111, No. 4, pp. 1667-1674, (2002).
- [38] Choudhari, N.K., Kumar, A., Kumar, Y. and R. Gupta: Evaluation of elastic moduli of concrete by ultrasonic velocity. NDE 2002, National Seminar of ISNT, Chennai, (2002).
- [39] Forschergruppe 384: Zerstörungsfreie Strukturbestimmung von Betonbauteilen mit akustischen und elektromagnetischen Echo-Verfahren, Internetpräsenz: <http://www.for384.uni-stuttgart.de/>, (2004).
- [40] Große, C., Wiggenhauser, H., Algernon, D., Schubert, F. und R. Beutel: Impact-Echo – Stand der Technik und Anwendungen des Verfahrens. Tagungsunterlagen zur Fachtagung 2005 des DafStb, Zerstörungsfreie Prüfverfahren und Bauwerksdiagnose im Betonbau 10./11. März 2005, Berlin, BAM, S. A11-A18.

- [41] Köhler, B., Schubert, F., Algernon, D., Gardei, A., Mielentz, F. and M. Krause: Experimental study of elastic waves in concrete for NDE in civil engineering. 31st Annual Review of Progress in Quantitative Nondestructive Evaluation (QNDE), Canada, (2004).
- [42] Krautkrämer, J. und H. Krautkrämer: Werkstoffprüfung mit Ultraschall. 5. Aufl., Berlin, Springer, (1986).
- [43] Lausch, R., Wiggenhauser, H. und F. Schubert: Geometrieeffekte und Hüllrohrortung bei der Impact-Echo-Prüfung von Betonbauteilen – Experimentelle und modelltheoretische Ergebnisse. DGZfP Jahrestagung 06.-08. Mai 2002 in Weimar, DGZfP-Berichtsband BB-80-CD, Plakat 34, (2002).
- [44] Mielentz, F., Ernst, H., Wüstenberg, H., Mayer, K. und R. Marklein: Überprüfung der Funktionsweise von laufzeitgesteuerten Gruppenstrahlern für Ultraschallprüfungen von Betonbauteilen durch Visualisierung der Wellenausbreitung, München, Carl Hanser Verlag, MP Materialprüfung, Vol. 46, pp. 11-12, (2004).
- [45] Schickert, G., Henschen, J., Krause, M., Maierhofer, C., Weise, F., Wiggenhauser, H. und K. Borchardt: ZfPBau-Kompodium. Bundesanstalt für Materialforschung und -prüfung BAM, Berlin, 1999. www.bam.de/service/publikationen/zfp_kompodium/welcome.htm
- [46] Maierhofer, C., Krause, M., Niederleithinger, E. and H. Wiggenhauser: Non-destructive testing methods at BAM for damage assessment and quality assurance in civil engineering. Proceedings of the International Symposium on Non-Destructive Testing in Civil Engineering, (2003).